TU WIEN

DISSERTATION

Construction of a high temperature sessile drop device for wettability studies in the Carbon/Copper system

ausgeführt zum Zwecke der Erlangung des akademischen Grades eines Doktors der technischen Wissenschaften unter der Leitung von

a.o. Univ. Prof. Dipl.-Ing. Dr.techn. Christoph Eisenmenger-Sittner
E138
Institut für Festkörperphysik

eingereicht an der Technischen Universität Wien
Fakultät für Physik

von

Dipl.-Ing. Bernhard Schwarz
e9626156
Arndtstraße 42-44/R22
A-1120 Wien

Wien, am 26. 03. 2008

Contents

Kurzfassung

Das Ziel dieser Dissertation war das Benetzungsverhalten in Kupfer - Kohlenstoff Systemen zu untersuchen. Hauptziel dabei war die Konstruktion einer Hochtemperaturkontaktwinkelanlage um geschmolzene Metalltropfen auf festen Substraten zu studieren. Die verwendete Methode war die des liegenden Tropfens (engl. sessile drop method). Dabei wird das Metall aufgeschmolzen und der so entstandene Tropfen im flüssigen Zustand abfotographiert. Die daraus ableitbaren Informationen sind der Kontaktwinkel der Flüssigkeit mit dem Festkörper, die Oberflächenenergie im flüssigen Zustand und die Identifizierung des Benetzungsregimes. Der Kontaktwinkel eines flüssig/fest Systems ist das Hauptkriterium für die Beschreibung des Benetzungsverhaltens eines solchen Systems.

Nach einer breit angelegten vergleichenden Literatursuche über Hochtemperaturkontaktwinkelanlagen, wurde eine solche selbst konstruiert und gebaut; der Einsatzbereich ist bis zu einer Temperatur von ca. 1100°C unter Hochvakuum. Die Einzigartigkeit unserer Anlage ist der speziell konstruierte widerstandsbeheizte Substrathalter, der auch als Substrathalter in einer Physical Vapour Deposition (PVD) Anlage genutzt werden kann. Die in-situ Aufnahme des Tropfens erfolgt mittels Webcam, der eine Optik vorgesetzt wurde. Für die Auswertung des Kontaktwinkels zwischen Flüssigkeit und Substrat ist eine eigene Software verfügbar.

Mit der fertiggestellten Hochtemperaturkontaktwinkelanlage wurden Benetzungsexperimente mit Kupfer und kupferbasierten Loten (engl. active brazing alloys) auf Zwischenschichten aus TiN und Mo durchgeführt. Im Fall von TiN wurden ebenfalls substöchiometrische Schichten untersucht und im Fall von Mo wurde die Karbidbildung in der Mo Schicht bei Temperaturbehandlung charakterisiert sowie mit einem Modell verglichen. Die Identifizierung des Benetzungsregimes geschieht mit Hilfe der zeitlichen Entwicklung des Tropfens während des Benetzungsexperiments.

Diese Dissertation gliedert sich folgendermaßen:

Im Kapitel *"Introduction"* werden die Gründe für die Materialwahl Kupfer - Kohlenstoff beschrieben, sowie die Anwendung von benetzungssteigernden Zwischenschichten in der Herstellung von Wandauskleidungen in zukünftigen Fusionsreaktoren.

Das Kapitel *"High Temperature Sessile Drop Device"* beschäftigt sich mit der Planung und der Konstruktion der Bestandteile der Hochtemperaturbenetzungsanlage. Die einzelnen Teile (Substrathalter, Metallzuliefersystem, Thermoelement) werden

hier beschrieben.

Das nächste Kapitel *"Information from the liquid drop"* zeigt, welche Informationen aus der Tropfengeometrie abgeleitet werden können (wie zum Beispiel der Kontaktwinkel und die Berechnung der Oberflächenenergie im flüssigen Zustand). Der Massenverlust durch das Abdampfen während der Experimente wurde bestimmt und mit theoretischen Vorhersagen (Knudsen Formel) verglichen.

Im Kapitel *"Physical vapor deposition"* werden die Grundprinzipien des Sputterprozesses beschrieben, sowie die Herstellung von substöchiometrischen TiN mittels reaktivem Sputtern. Diese wurden mit theoretischen Modellen für reaktives Sputtern verglichen.

Das Kapitel *"Carbon with interlayers"* beschreibt die Oberflächenenergiemessung an glasartigem Kohlenstoff und stellt die ersten Benetzungexperimente mit unterschiedlichen Zwischenschichten auf Kohlenstoff vor.

Das folgende Kapitel *"Substoichiometric TiN as wetting promoter"* beschäftigt sich mit den Ergebnissen der Benetzungexperimente an stöchiometrischen und substöchiomtrischen TiN Schichten. Das Konzept des reaktiven Benetzens wird vorgestellt, sowie auf die beiden Unterarten, die diffusionskontrollierte reaktive Benetzung und die reaktionskontrollierte reaktive Benetzung, eingegangen. Außerdem werden die Ergebnisse der Lötexperimente mit TiN und substöchiometrischem TiN auf Graphit und CFC (**C**arbon **F**iber reinforced **C**arbon - Kohlenstofffaser verstärkter Kohlenstoff) dargestellt.

Im Kapitel *"Molybdenum as wetting promoter"* werden Benetzungsexperimente auf Mo und auf Mo-Schichten gezeigt. Außerdem beschäftigt es sich mit dem Karbidisierungsprozeß einer dünnen Mo Schicht während der Temperaturbehandlung. Hier werden die experimentellen Ergebnisse der Bildung der Karbidschicht mit einem theoretischen Modell (Zellularautomat - Cellular Automaton) verglichen.

Im letzten Kapitel *"Conclusion"* werden die Ergebnisse dieser Dissertation nochmals kurz zusammengefasst und ein Ausblick auf zukünftige Arbeiten gegeben.

Abstract

The objectives of this thesis were wettability studies in the Carbon - Copper system. Therefore the overall aim was the construction of a High Temperature Sessile Drop Device (HTSDD) to study the wettability of a liquid metal on a solid substrate. Sessile drop means to melt a metal on a plane substrate and to image the curvature of the droplet, gaining informations on the contact angle, liquid surface energy and identifying the wetting regime. The contact angle in a liquid/solid system is the main property to describe the wetting behavior in the system.

After a comparative literature survey about high temperature wetting we planned and constructed a sessile drop device with the ability of melting metals up to approx. 1100°C under high vacuum and the capability of in-situ imaging of the liquid drop. A novelty of this custom-built device is the resistance heated substrate holder, which is also suitable for sputter deposition in a physical vapor deposition (PVD) plant. The imaging of the liquid drop is done by a webcam with an additional optic and for the determination of the contact angle a self-written software is available.

With the HTSDD wetting experiments of Cu and a Cu-based active brazing alloy (CuABA) were performed on TiN and Mo coatings. In the case of TiN also substoichiometric films were investigated and in the case of Mo the carbide formation in the Mo-film during heat treatment was investigated and compared with a model. The identification of the reactive wetting regime in the C/CuABA system can be deduced from the time evolution of the droplet.

The structure of this thesis is as follows:

In the chapter *"Introduction"* the reasons for the choice of C/Cu are described, also the application of wetting promoting thin films in the joining of plasma facing components in future fusion reactors is presented.

The chapter *"High Temperature Sessile Drop Device"* deals with the planning and construction of the sessile drop device. The individual parts of the device (substrate holder, manipulator, thermocouple) are described here.

The next chapter *"Information from the liquid drop"* deals with some information gained from the curvature of the droplet: the contact angle and the liquid surface energy can be calculated. The mass loss of the molten metal during the experiments was compared with theoretical predictions (Knudsen model).

In the chapter *"Physical vapor deposition"* the basics of sputtering are explained

and the deposition of substoichiometric TiN films is described. A comparison with a theoretical model for reactive sputtering from literature is given.

The chapter *"Carbon with interlayers"* describes surface energy measurements of the glassy carbon and gives the first wetting experiments with different interlayers deposited onto the carbon substrate.

The following chapter *"Substoichiometric TiN as wetting promoters"* deals with the results of the wetting experiments of stoichiometric and substoichiometric TiN films. The concept of reactive wetting is presented with the distinction between diffusion limited and reaction limited reactive wetting. The brazing results of the sputter deposited films on graphite and CFC (Carbon Fiber reinforced Carbon) are shown as well.

In the chapter *"Molybdenum as wetting promoter"* wetting experiments on pure Mo and on Mo coatings are presented. Also the carbidization process during the heat treatment of thin Mo films was studied. Experimental results of the carbide layer formation are compared with a mathematical model using a Cellular Automaton.

In the last chapter *"Conclusion"* the results of this thesis are shortly summarized and an outlook on further work is given.

Chapter 1

Introduction

The material combination of Copper and Carbon, which both have remarkable physical properties, offers a wide range of possible applications. Some material parameters of pure copper and two allotropes of Carbon (graphite and diamond) are shown in Table 1.1.

	Density$[g/cm^3]$	Crystal structure	T_M $[°C]$	Therm.Cond. $[W/mK]$
Copper	8,92	fcc Fm-3m	1084	400
Graphite	2,267	hcp P63/mmc	3527 [1]	140
Diamond	3,513	fcc Fd3m	800 [2]	1000 [3] / 2000-2500 [4]

[1] no actual melting point at atmosphere, sublimates over 3500°C

[2] flashpoint at 800°C

[3] diamond impure

[4] purified synthetic diamond

Table 1.1: Material parameters for Carbon and Copper [1, 2].

One application of the above mentioned Cu/C system is in heat sinks. Heat sinks of C-fibers embedded in a copper matrix (MMCs - metal matrix composites) are also of great technological interest in the semiconductor industry because of the tunable properties of these composites. Copper has a very high thermal conductivity, and by mixing a suitable amount of C-fibers the Coefficient of Thermal Expansion (CTE) can be varied in the range of $4-8 \times 10^{-6} K^{-1}$, which is the required range for matching the CTE of electronic components ($\alpha_{Si} = 4, 1 \times 10^{-6} K^{-1}$, $\alpha_{GaAs} = 5, 8 \times 10^{-6} K^{-1}$,

$\alpha_{\mathrm{Cu}} = 16 \times 10^{-6} \mathrm{K}^{-1}$ [3, 4]). The poor adhesion of these two elements is due to their low wettability which is characterized by a contact angle of approx 140° of liquid Cu on solid C which is far above 90°. Generally wetting is defined by a contact angle less then 90°.

The characterization of the wetting behavior of two different elements can be done by measuring the contact angle of a liquid drop on a solid substrate by means of the sessile drop method. The sessile drop technique is the configuration where one material will be molten (by various methods) and the molten droplet is optically imaged. The recorded contact angle and the shape of the droplet gives evidence of the wetting behavior of the melt with the solid substrate. Also the liquid surface energy can be estimated. This knowledge is of great technological interest because metallic spreading is intrinsic to many industrial processes such as brazing, soldering and thin film processing.

Additionally, wetting properties are needed to describe the liquid-state processing of composites, for example the infiltration of ceramic fiber preforms by liquid metals. In case of MMCs consisting of Carbon fibers with metals the most satisfactory route is the infiltration of the reinforcing network by the metal in the liquid state. As liquid metals usually do not wet the fibers, it is necessary to force infiltration by applying an external pressure. Many methods are available: vacuum infiltration, squeeze casting, liquid metal infiltration and pressure assisted network infiltration [5, 6, 7, 8, 9, 10]. But due to poor wettability and small diameters of modern fibers, applying pressure often does not assure an optimum contact between fiber and matrix. Therefore research has been directed towards wettability enhancing procedures. These consist either in depositing a suitable overlayer/interlayer on the surface of the reinforcing network or in adding surface active alloying elements to the metal.

Another application of the C/Cu system is as plasma facing component (PFC) in future nuclear fusion reactors of the Tokamak type ("ТОРОИДАЛЬНАЯ КАМ-ЕРА С МАГНИТНЫМИ КАТУШКАМИ" - "toroidal chamber in magnetic coils" and the first syllable of the abbreviation "ТОК" - "current"), like the planned ITER (International Thermonuclear Experimental Reactor) in Cadarache, France.

The construction of ITER has one overall objective: "to demonstrate the scientific and technological feasibility of fusion energy for peaceful purposes" [11]. The design of ITER is a Tokamak plasma confinement, with superconducting toroidal and poloidal field coils around the toroidal vacuum vessel. A cross section through one side of this toroidal vacuum vessel is given in Figure 1.1.
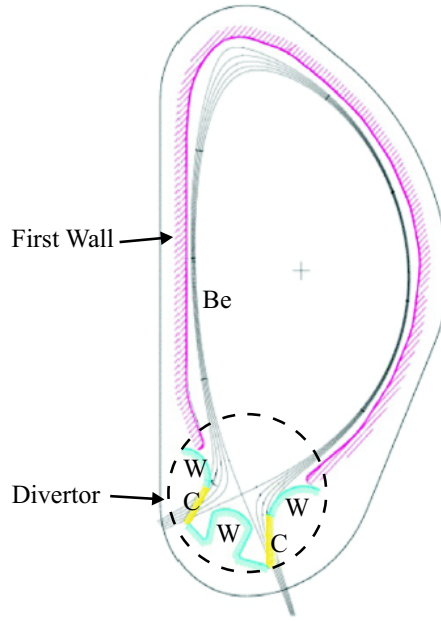

Figure 1.1: Cross section of the toroidal ITER plasma vessel.

The vacuum vessel is roughly divided into two parts: the first wall and the divertor[1]. The first wall consists of l cm thick beryllium armor protection, l cm thick copper to diffuse the heat load as much as possible, and approx. 10 cm of steel structure. The advantages of beryllium are: low Z material, oxygen gettering capability, absence of chemical sputtering and high thermal conductivity.

The divertor materials are tungsten (lowest sputtering, highest melting point, high thermal conductivity and no concern about tritium inventory) and CFC (longest lifetime, absence of melting, thermal shock resistance, high thermal conductivity

---

[1]The divertor is part of a fusion reactor. Its purpose is the removal of the He-4 and the impurities from the wall materials. With additional magnetic fields these ions are deflected to the divertor plates, where they can recombine with electrons and then be pumped off the vacuum chamber.

and low atomic number). They are used depending on the heat flux from the plasma. In Figure 1.2 an image of the divertor is shown, where the different heat fluxes are indicated.
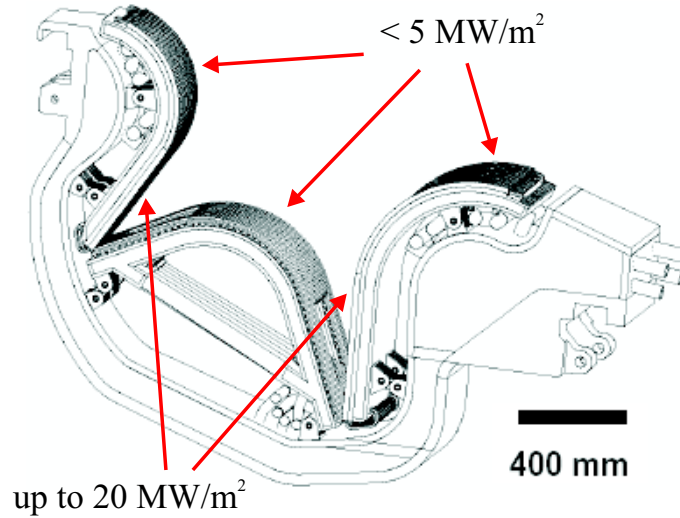

Figure 1.2: Image of the ITER divertor, with the maximal heat fluxes expected.

The divertor itself consists of 54 separate divertor cassettes for the better maintenance of the device, a prototype of such a divertor cassette is shown in Figure 1.3. These PFC have to withstand the intense neutron irradiation and a suddenly changing high heat flux. The thermal shock creates critical localized stresses in the material and in the joints between different materials.

The PFCs are composed of a thick stainless steel back. This carries an array of heat sinks, cooled by water flowing in cooling channels. The heat sink is covered by a protective material, carbon based or tungsten based, depending on the position in the divertor. The state of the art material for the application with carbon is a 3D Carbon Fiber reinforced Carbon (CFC) as protective material and a CuCrZr precipitation hardened copper alloy (0,3 - 1,2 wt% Cr, 0,03 - 0,3 wt% Zr, Cu balance) as heat sink material. For the joining of CFC to CuCrZr a pure copper interlayer is used. This interlayer is produced by casting pure Cu onto the CFC, whereas the CFC is previously activated with Ti (Active Metal Casting). Then the Cu interlayer is joined to CuCrZr by Hot Isostatic Pressing (HIPing). Brazing with commercial CuTi brazing alloys instead of the Active Metal Casting is taken into consideration.
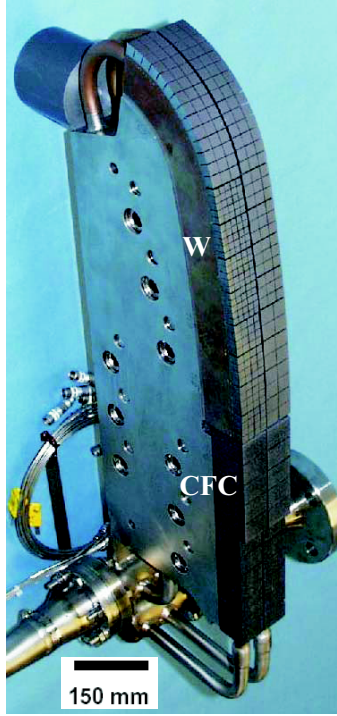
Figure 1.3: Image of the ITER divertor cassette. The two plasma facing materials tungsten and carbon are visible in the image.

The CTE of the protective material is usually low (1 - 4 $\times 10^{-6} \mathrm{K}^{-1}$), whereas the CTE of the CuCrZr heat sink is about $15,7 \times 10^{-6} \mathrm{K}^{-1}$. The thermal conductivity should be as high as possible, $\geq 320\,\mathrm{Wm}^{-1}\mathrm{K}^{-1}$ for the heat sink and $\geq 330\,\mathrm{Wm}^{-1}\mathrm{K}^{-1}$ at 20°C and $\geq 150\,\mathrm{Wm}^{-1}\mathrm{K}^{-1}$ at 800°C for the C-based protective material. Because of the high heat flux the PFCs have to be actively cooled. As a consequence the protective material needs a thermal conductivity as high as possible, which reduces the thermally induced mechanical stress.

Some additional requirements for the materials are:

- Both protective materials and materials used in joints and interlayers have to be free of low melting point and high vapor pressure elements (pollution of the plasma with atoms).

- All the material used for PFCs have to be as free as possible of high activation elements (environmental safety - all PFCs have to be removed every four years, in the case of ITER).

- All the material used for PFCs have to be free of Ag, Au and any other element prone to nuclear transmutation to high vapor pressure elements under neutron irradiation (Au, e.g., transmutes to Cd)

The advantages of CFC as the protective material are: longer lifetime (in comparison to tungsten), absence of melting, excellent thermal shock resistance, very high thermal conductivity (e.g. NB31[1] CFC x-direction: 323 $Wm^{-1}K^{-1}$, y-direction: 117 $Wm^{-1}K^{-1}$, z-direction: 115 $Wm^{-1}K^{-1}$) and low atomic number. Low-Z elements are one preferred material class because they are less prone to "pollute" the plasma. W-based protective materials, on the other hand, have high erosion resistance and very low sputtering yield. The heat flux in normal operation mode is about 10 MWm^{-2} on PFCs with C-based materials and 0,1 - 5 MWm^{-2} on PFCs with W-based protective materials for a time < 450 s. The neutron irradiation dose is 0,7 dpa (displacements per atom) for the protective material and 2 dpa in the heat sink. The aim within this work is to find a wetting promoting layer between CFC and the Cu layer to enhance the wettability of these two elements for an improved joint.

For the PFC (tungsten as well as carbon) there are two possible configurations: the flat tile geometry and the monoblock geometry. Both of them are used in the divertor design. Images of already produced mock-ups of these geometries are shown in Figure 1.4 (flat tile geometry) and Figure 1.5 (monoblock geometry).

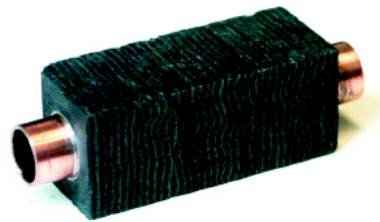*Figure 1.4: Image of the flat tile mock-up design.*

Figure 1.5: Image of the monoblock mock-up design.

This mock-up design is used for simulating the thermal load in high heat flux tests. The manufacturing of the flat tile geometry is much easier than of monoblocks, but

---

[1]Material parameters see Appendix F

the thermal fatigue performance of monoblock components is much better than of flat tiles. Nevertheless, both of them are foreseen in the ITER design.

A detailed state of the art manufacturing scheme of the flat tile geometry is given in Figure 1.6, and of the monoblock design in Figure 1.7.
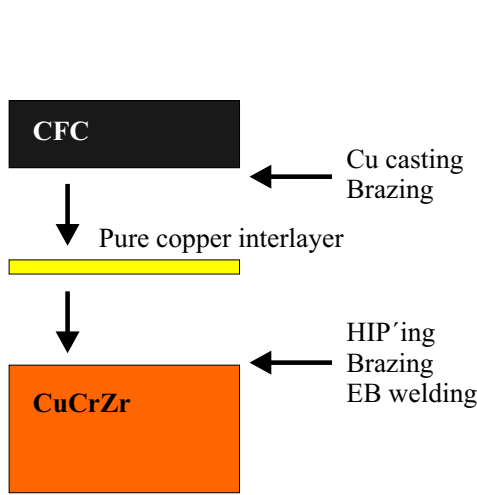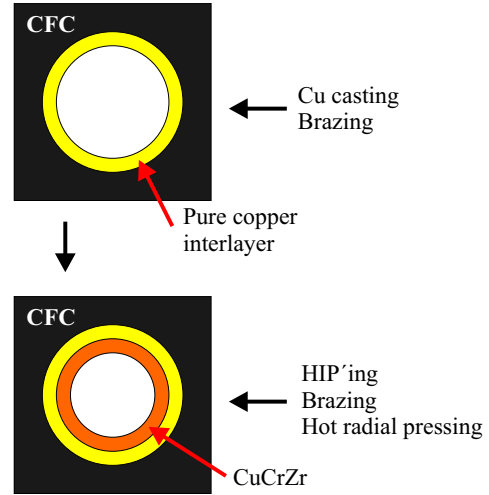

Figure 1.6: Scheme of the flat tile geometry.

Figure 1.7: Scheme of the monoblock geometry.

The joining of the CFC to the CuCrZr heatsink in the monoblock design is realized by a pure copper interlayer, which is joint to the CFC by brazing or Cu casting. The joining to the CuCrZr heat sink is done by HIPing, brazing or electron beam (EB) welding.

The manufacturing of the monoblock design is also realized by a pure copper interlayer, but in this design all components have to be adapted to a cylindrical shape. Instead of EB-welding, hot radial pressing of the CuCrZr heat sink tube is possible [12].

Improvements to the flat tile geometry are mainly concerning the interface CFC-pure copper interlayer. Wetting promoting thin films deposited on the CFC are a promising method for a better joining of the compound as it will be shown in this work.

Chapter 2

Fundamentals of Contact Angle and Wettability

2.1 Contact Angle

On a flat, perfectly smooth and homogeneous solid surface a liquid drop intersects with the solid surface under a "contact angle", θ. This angle is used to define the wettability of liquids on solids and is related with the surface and interface energies by Young's equation [13]:

$$\cos\theta = \frac{\sigma_{SV} - \sigma_{SL}}{\sigma_{LV}} \tag{2.1}$$

where σ_{SV}, σ_{SL} and σ_{LV} are the solid-vapor, solid-liquid and liquid-vapor interface energies, respectively. Figure 2.1 shows a schematic of the sessile drop profile, where the interfacial energies are drawn. The line where the different phases meet is called triple line.
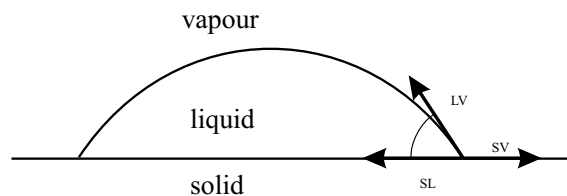

Figure 2.1: Interfacial energies of a sessile drop.

A contact angle smaller than 90° defines wetting behavior, an angle greater than 90° defines non wetting and an angle of 0° identifies perfect wetting of the liquid. The different wetting regimes depending on the contact angle are sketched in Figure 2.2.
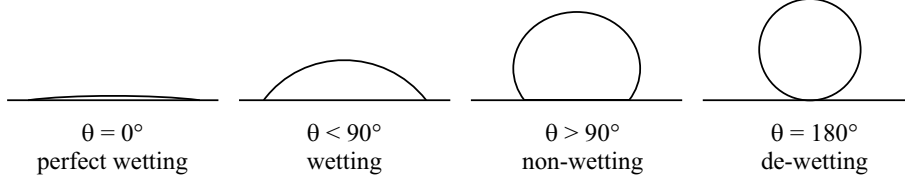

Figure 2.2: Different wetting regimes depending on the contact angle.

Equation 2.1 can be derived from the variation of the surface free energy F_S of the system caused by a small displacement δz of the triple line on the solid surface (Figure 2.3).
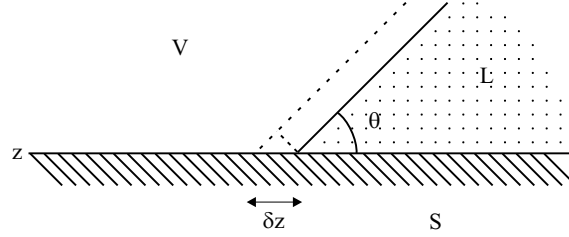

Figure 2.3: Triple line displacement for the derivation of the Young equation.

$$\delta F_S = F_S \left(z + \delta z \right) - F_S \left(z \right) = \left(\sigma_{SL} - \sigma_{SV} \right) \delta z + \cos \theta \sigma_{LV} \delta z \tag{2.2}$$

The equilibrium condition

$$\frac{d \left(\delta F_S \right)}{d \left(\delta z \right)} = 0 \tag{2.3}$$

leads to Equation 2.1. For this derivation only a small region around the triple line is taken into account to neglect the curvature of the real droplet. A second derivation of Young's equation is given in Appendix D, where the whole spherical cap of the droplet was used for the derivation.

The interfacial adhesion is usually measured by the thermodynamic work of adhesion W_A, which is related to the surface and interface energies of the system by:

$$W_A = \sigma_{LV} + \sigma_{SV} - \sigma_{SL} \qquad (2.4)$$

Combining Equation 2.1 and Equation 2.4 leads to the Young-Dupré equation [14, 15],

$$W_A = \sigma_{LV} \left(1 + \cos\theta\right) \qquad (2.5)$$

which relates W_A to θ. By measuring the contact angle and the surface energy of the liquid/vapor interface the work of adhesion can by calculated.

2.2 Influences on the contact angle

2.2.1 Drop size

When the sessile drop size reaches the order of the range of atomic interactions, the contact angle geometry changes. In this case the interfacial free energy by increasing the length of the triple line of the droplet has to be taken into account. The variation of the energy is

$$\delta F_S = 2\pi R \left(\sigma_{SL} - \sigma_{SV}\right) \delta R + 2\pi R \cos\theta \sigma_{LV} \delta R + 2\pi\tau\delta R \qquad (2.6)$$

with τ as excess free energy of the triple line, R as droplet radius and δR as the variation of the drop radius.

Again the equilibrium condition $d\left(\delta F_S\right)/d\left(\delta R\right)$ leads to:

$$\cos\theta_{eq} = \cos\theta - \frac{\tau}{R\,\sigma_{LV}} \qquad (2.7)$$

The importance of this second term $\tau\left(R\,\sigma_{LV}\right)^{-1}$ decreases with increasing drop size and can be neglected for R > 100 nm. No significant differences in contact angles of millimeter and micrometer size droplets have been found in [16]. This correction is only important for very small droplets in the nm-range, e.g. those which nucleate by condensation on solid surfaces.

2.2.2 Surface Roughness

The wetting of rough surfaces is affected by the increase of the actual surface area compared to the ideally smooth surface. According to Equation 2.2 again the variation of the interfacial free energy F_S resulting from a small displacement δz is calculated.

$$\delta F_S = (\sigma_{SL} - \sigma_{SV}) \, s_r \delta z + \sigma_{LV} \cos \theta \delta z \tag{2.8}$$

Here s_r is the ratio between the actual surface to the planar surface and $s_r > 1$. The equilibrium condition $d(\delta F_S)/d(\delta z) = 0$ leads to the Wenzel equation [17]:

$$\cos \theta_W = s_r \cos \theta \tag{2.9}$$

This equation indicates that with increasing surface roughness, the actual contact angle decreases for hydrophilic materials ($\theta < 90°$) and increases for hydrophobic materials ($\theta > 90°$). So the surface roughness, which is always bigger than one, enhances both the hydrophilicity of hydrophilic surfaces and the hydrophobility of hydrophobic surfaces. In this equation, the solid surface is assumed to contact completely with the liquid between their interfaces.

2.2.3 Heterogeneous Materials

When we assume that the solid surface is composed of two materials (1 and 2), mixed microscopically, then the contact angle θ_R of a liquid on this surface can be expressed as

$$\cos \theta_R = f_1 \cos \theta_1 + f_2 \cos \theta_2 \tag{2.10}$$

with f_1 and f_2 as the surface fractions of the materials 1 and 2, and θ_1 and θ_2 as the contact angles of the pure materials 1 and 2, respectively [18, 19, 20]. Assuming one of the two materials to be air leads to the concept of superhydrophobicity. In general superhydrophobicity means a contact angle of the liquid bigger than 150°. This is of great interest for repelling water from surfaces (Lotus - effect). Equation 2.10 then assumes the form

$$\cos \theta_R = f_1 \cos \theta_1 - f_2 \tag{2.11}$$

with f_2 as the surface fraction of air and $f_1 + f_2 = 1$. The contact angle θ_2 on air is 180°. Increasing the surface fraction of air on the solid (structured surfaces, porous surfaces) leads to increasing contact angles of the liquid (above the value of 150° for superhydrophobicity). Equation 2.11 can also be written as

$$\cos \theta_R = f (\cos \theta + 1) - 1 \tag{2.12}$$

with f as surface fraction of the material and θ as contact angle on the flat material. In this equation the strong influence of small f is visible, reducing the right hand side of the equation to values near -1, which means contact angles in the region near 180°.

2.2.4 Gravitational field

In the case of millimeter size droplets the gravitational field is responsible for the modification of the liquid shape of the drop through its own weight. It has been discussed if the classical Young equation is also valid in this case. A clean proof of the validity of the Young´s equation is given in [21], achieved by minimization of the free energy of the system including a gravitational term.

2.3 Laplace equation

The sessile drop method is based on the measurement of the drop shape built by the equilibrium between the action of the gravitational field, which tends to flatten the drop, and the surface tension which requires the smallest surface area. This curvature is described by Laplace's equation [14, 22]:

$$\Delta P = \sigma_{LV} \left(\frac{1}{R_1} + \frac{1}{R_2} \right) \tag{2.13}$$

with ΔP as excess pressure at a given point of the drop surface and R_1, R_2 the principal radii in this point (see Fig. 2.4). This equation can be rewritten in the form of Bashforth and Adams [23]

$$\frac{b}{R_1} + \frac{b\sin\phi}{x} = 2 + \beta\frac{z}{b} \tag{2.14}$$

with

$$\beta = \frac{b^2\rho g}{\sigma_{LV}} \tag{2.15}$$

where b is the radius of curvature at the drop apex, g is the acceleration of gravity, ρ is the density of the liquid, which is used instead of the more rigorously correct difference between it and the density of the vapor (or vacuum) and ϕ the angle from the apex to a point of the surface of the droplet. The radius of curvature R_1 and $\sin\phi$ can be expressed in terms of the first and second derivatives of z with respect to x. Substituting them into Equation 2.13 leads to a differential equation with no analytical solutions. Two ways of handling this equation are possible, numerical solution by curve fitting into the experimental drop shape or by empirical relationships. For droplets larger than the capillary length $(2\sigma_{LV}/(\rho g))^{1/2}$ the relationship suggested by Dorsey [24] is the most accurate one:

$$\sigma_{LV} = \rho g x_{90}^2 \left(\frac{0,052}{f_1} - 0,1227 + 0,04881 f_1\right) \tag{2.16}$$

with the factor

$$f_1 = \frac{H_{45}}{x_{90}} - 0,04142 \tag{2.17}$$

and the distances H_{45} and x_{90}, which are given in Figure 2.4. By measuring the two distances from the drop profile it is possible to calculate the liquid surface energy of the drop.

The radius R_1 is in the plane of paper and $R_2 = x/\sin\phi$ is in a plane perpendicular to the paper. Also the contact angle θ and the angle ϕ are drawn in Figure 2.4.

For drops smaller than 1 cm another relationship is proposed, due to the lower influence of gravitation [25],

$$\sigma_{LV} = D d_m^2 \rho g \tag{2.18}$$

with d_m as the maximal drop diameter and D as a geometrical factor which is related to $d_m/2H$, where H is the height from the maximal diameter to the drop apex. A schematic is shown in Figure 2.5.
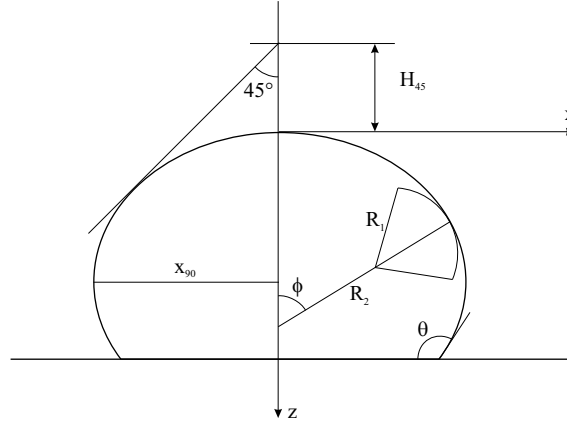
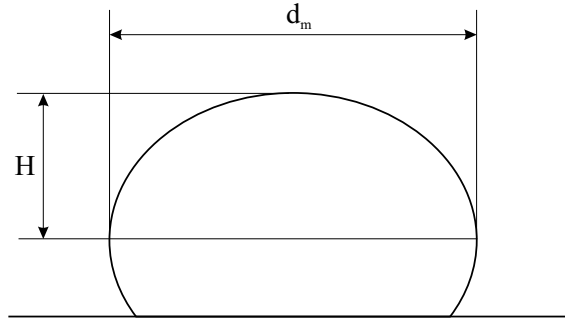*Figure 2.4: Profile of the sessile drop with the parameters.*

Figure 2.5: Schematic view showing the geometry for small drops.

A plot of values of D versus $d_m/2H$ can be found in [26, 27], so after measuring the two distances the surface energy of the liquid drop can be determined by Equation 2.18.

Chapter 3

High Temperature Sessile Drop Device

3.1   Common sessile drop instruments

A big variety of different types of sessile drop devices can be found in literature [28, 29, 30, 31, 32, 33], but they all have the same goal: to image the molten drop from the side to see the curvature of the liquid.

For the measurement of liquid metals a vacuum chamber with a high vacuum or an inert gas (Ar) is necessary to prevent the liquid from oxidation. The heating is realized by different furnaces (graphite heating, radiation heating, tantalum heater, cartridge heater) and temperatures up to 2000 K can be achieved. Digital or optical cameras are used to image the drop and a bright background illumination for a better contrast of the images is necessary.

The usual way of melting is as follows: cleaning the sample, then putting the sample into the furnace, evacuating the chamber and heating up to the melting point and above. The other way reported is first to melt the metal and then drop the liquid down to the surface. Each group has its own equipment, so much attention has to be paid when comparing the different results.

3.2   Construction of the device

For the construction of the high temperature sessile drop device (HTSDD) one demand was crucial: a common application with several PVD sputter plants. The solution was a resistance heated substrate holder, which is suitable for the sputter plant as well as for the HTSDD. This led to a geometric limitation of the substrate holder, because the connection port of the PVD plant is realized by an ISO 40 KF flange. So the heating of the metal sample had to be done by a resistance heated 0,5 mm thick Ta-foil onto which the substrates for the wettability measurements are clamped. Figure 3.1 gives a schematic overview of the HTSDD.
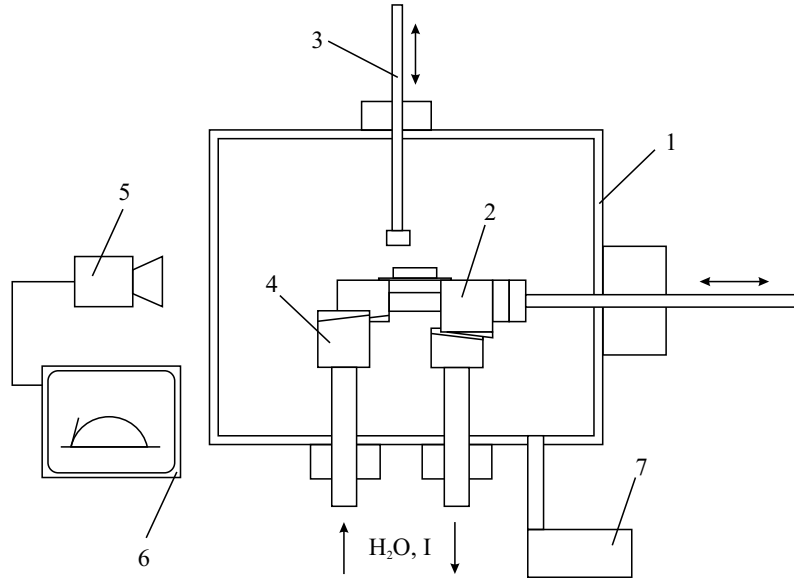
Figure 3.1: Schematic of the high temperature sessile drop device:
  1) Vacuum chamber
  2) Heatable substrate holder
  3) Manipulator or thermocouple
  4) Water cooled current counterparts
  5) Webcam with optic
  6) PC with measurement software
  7) Vacuum pumps (turbomolecular- and forepump)

An image of the high temperature sessile drop device with all necessary parts is given in Figure 3.2.

The whole device is operated under vacuum, which is generated by a turbomolecular pump and a rotary forepump. The base pressure of approx. 10^{-5} Pa is reached in
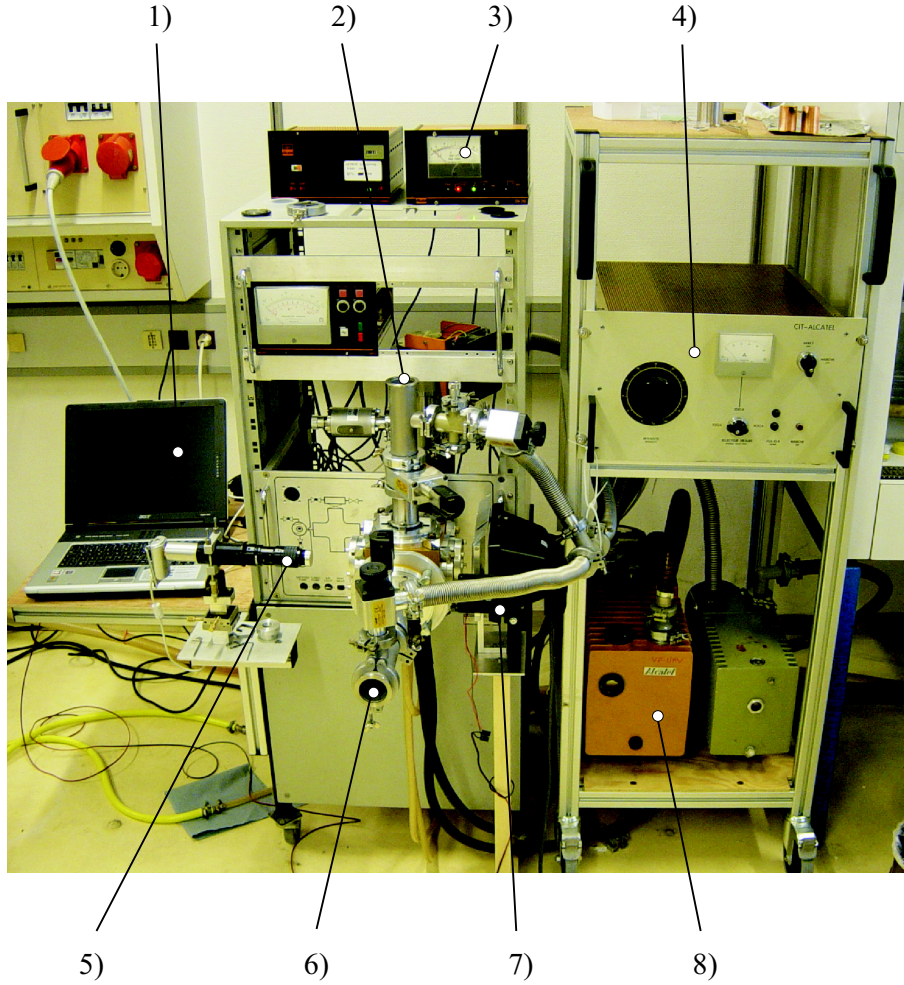
Figure 3.2: Image of the high temperature sessile drop device:
    1) PC with measurement software
    2) load lock for manipulator or thermocouple
    3) vacuum gauges
    4) high current supply
    5) optic with an additional protection foil[1]
    6) load lock for the heatable substrate holder
    7) background illumination
    8) rotary fore pumps

less than one hour after inserting the substrate holder. For measuring the drop profile a commercial webcam with an additional optic[1] is used, in connection with a PC and a custom-written software [34].

The heating of the substrate is done by a Ta resistance heater: A high current

---

[1]Technical details see Appendix C

supply (up to 400 A) is connected to water cooled Cu blocks, which have contrary wedges to the substrate holder for catching it. The sample delivery for the droplet formation is done by a manipulator from above; the same feedthrough can also be used for inserting a thermocouple into the device for temperature measurement.

All removable components of the HTSDD (the substrate holder, the manipulator and the thermocouple) can be inserted into the device via load-locks without breaking the vacuum of the chamber. This is a significant advantage to all other devices consisting of a vacuum furnace, where the whole furnace has to be opened for sample delivery and change.

3.2.1 Substrate holder

An image of the heatable substrate holder in given in Figure 3.3. The two copper parts with the catching wedges are electrically insulated by a ceramic (Macor$^{®}$) spacer and the system is mounted together by a thread rod.

1 cm
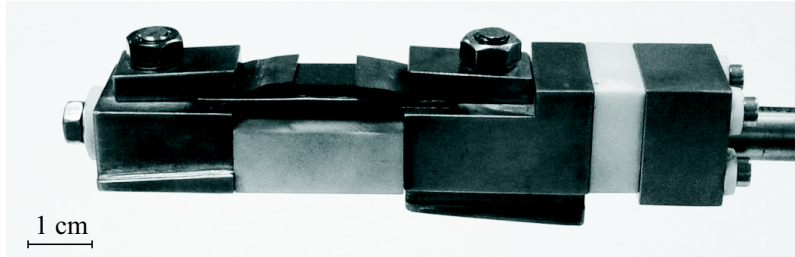
Figure 3.3: Heatable substrate holder.

The sample is clamped with stainless steel screws onto the Ta foil. With this construction measurements up to the melting point of Cu (1083°C) were successfully performed. The current for the measurements was supplied by a high current device, which can generate an output current up to 400 A (Input: 220 V, Output: 400 A/5 V or 200 A/10 V or 100 A/20 V). For a good electrical contact between the copper parts and the Ta foil, the foil has to be very flat to ensure a big enough contact area for the current.

For using this substrate holder in the PVD chamber the ceramic spacer has to be removed and replaced by another spacer including a shielding against the sputter deposition. This newly designed spacer is shown in Figure 3.4. Here the electrical

insulation is realized by two Macor spacers near the Cu blocks, with a steel tube
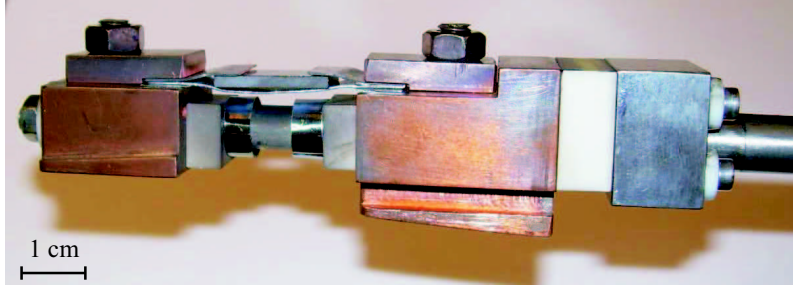between them.

Figure 3.4: Heatable substrate holder with Ta shielding.

It has to be guaranteed that no alternative current path is produced in the system.
This is achieved by two round Ta foils, which are assembled to form an undercut to
prevent sputtered atoms to reach this part during the deposition process.
In Figure 3.5 the whole situation during the sputter process is visible. The sputtered
atoms have a mean free path which is longer than the undercut of the substrate
holder and can therefore not build a continuous coating on the substrate holder.
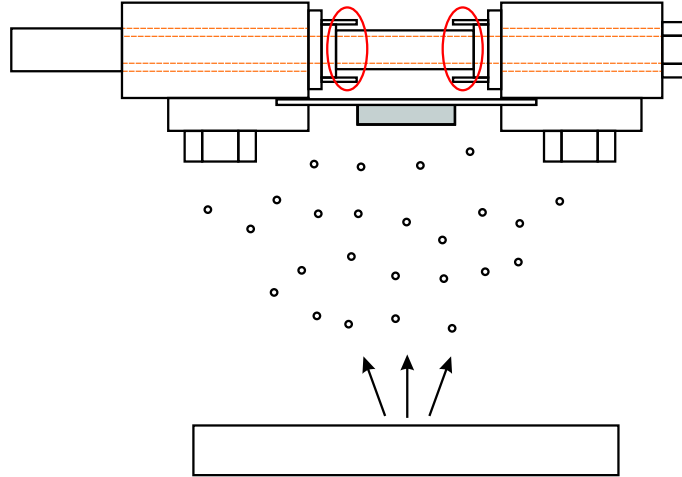
*Figure 3.5: Schematic of the heatable substrate holder with Ta shielding during the sputter
deposition.*

3.2.2 Manipulator

For the delivery of the metal pieces to the sample where the droplet is formed, a special designed supply system called "manipulator" was planned and constructed (see Figure 3.6 and Figure 3.7).
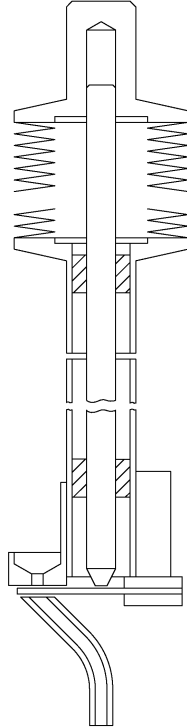
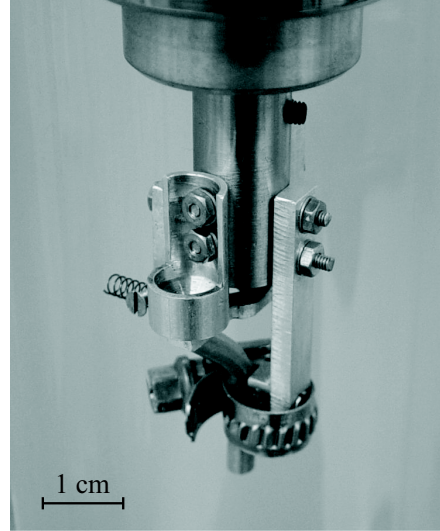*Figure 3.6: Schematic of the whole manipulator.*

Figure 3.7: Image of the lower supply system.

The aim of this device is the positioning of the metal onto the sample surface after the substrate holder is inserted into the HTSDD. Therefore the manipulator is moved via a linear/rotary feedthrough above the sample surface, then a small shutter opens a funnel and the metal for the wetting experiment slips to the surface through a bent tube. The big advantage of this procedure is the delivery of the drop forming metal under vacuum after the substrate holder was inserted into the chamber. So in case of PVD experiments, the surface of the coating will never come in contact with the ambient air. This leads to the possibility of studying wettability effects of surface contamination through the air compared to vacuum-transported samples.

3.2.3 Thermocouple

For the temperature measurement during the sessile drop experiments a Ni-CrNi thermocouple is placed onto the sample surface near the molten droplet. This configuration guarantees an accurate temperature measurement during the experiment. The same flange is used for the manipulator as well as for the thermocouple, so they have to be used one after another.

An image of the custom built Ni-CrNi thermocouple is given in Figure 3.8. The two metal wires are welded together in one point which is put as a measuring point onto the surface.
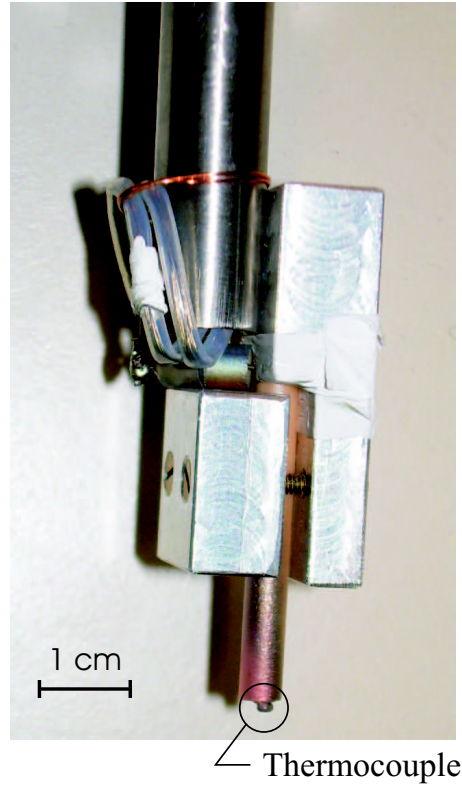
Figure 3.8: Thermocouple for temperature measurements.

The thermocouple is inserted into an Al_2O_3 tube. The tube is clamped into two aluminum blocks, which provide the mechanical stability and which are also responsible for the correct positioning of the thermocouple on the sample surface. A small but constant force of the thermocouple to the sample is realized by the difference

of two contrarily directed forces. The pressure difference between the outside and the inside of the plant tries to pull the thermocouple (mounted in a linear/rotary feedthrough) into the chamber. A spring mounted outside the feedthrough is holding against this force. By adjusting this spring a small definite force presses the thermocouple to the surface.

The calibration of the thermocouple was done by measuring the thermovoltage at the melting point of different elements and then fitting a curve into these values. In the lower temperature range of the calibration (up to 200°C) a hot stage was used, and in the upper range the melting points of the following elements (Table 3.1) were used for the calibration of the thermocouple:

Element	Melting point [°C]
tin	232
lead	327
silver	962
copper	1085

Table 3.1: Melting points of the four elements used for the temperature calibration of the thermocouple.

In Figure 3.9 the measured thermovoltage is drawn at the ordinate and the temperature is at the abscissa. A linear fit was put through these values and is also drawn in Figure 3.9. The equation of this linear fit is:

$$U_{\text{Therm}}[mV] = 0,0319\,T[°C] - 0,9683 \tag{3.1}$$

A table generated from Equation 3.1 was then used for the following wetting experiments (see Appendix, Table B.1).

For the temperature dependent evaluation of samples in the HTSDD a temperature regulation at different given thermovoltages was done. The temperature was increased very fast to the given value and then the temperature was held at this point for a certain time. The results of this investigation are shown in Figure 3.10. The experimental curve can be divided into two regions: the first one is a very fast increase in temperature, which is nearly linear and the set temperatures can
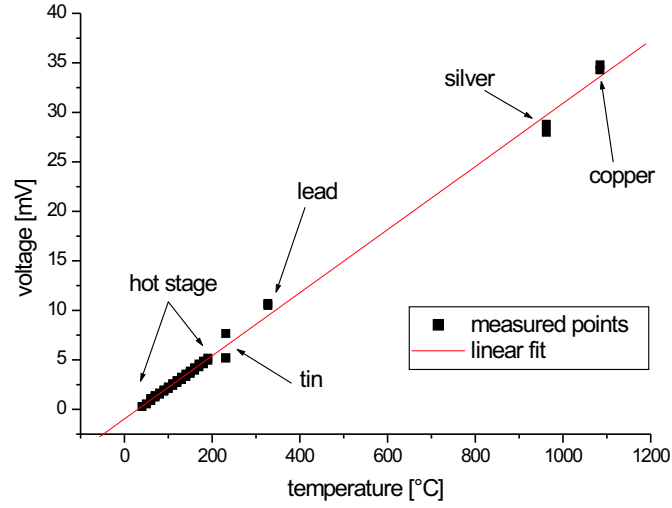
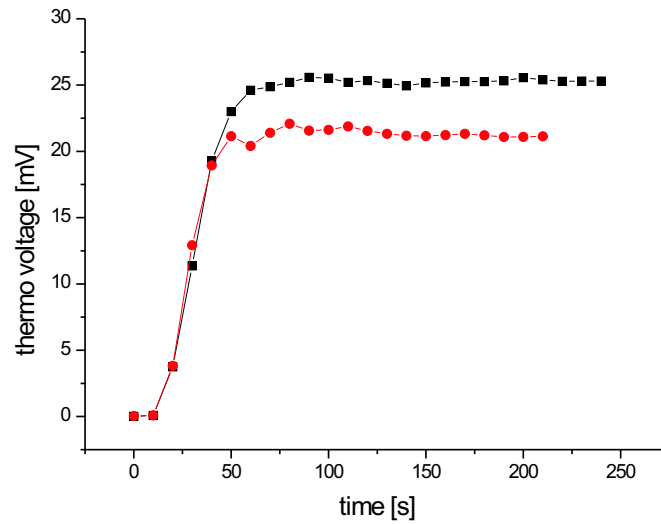*Figure 3.9: Calibration of the thermocouple using the melting point of four metals and a hot stage.*

Figure 3.10: Temperature regulation for two different thermovoltages (dots - 700° C, squares - 800° C).

be reached in about 50 sec. The second region is a constant temperature plateau at the set temperature and this can be held for several minutes (the estimated time/temperature maximum is about 3 minutes/1100°C, already performed, higher values were not necessary). This division into two parts was very satisfying, because for later calculations (reaction rate of molybdenum carbide, see Chapter 8) it was easy to simulate the temperature profile in these two regions by two straight lines.

3.3   Contact angle measurements

In the previous sections the parts of the HTSDD were described. Now the most general application is shown: in situ imaging of the contact angle of molten droplets during the wetting experiments. The output of the webcam are images with a resolution of 640×480 pixel, recorded in a time step of one second.

In Figure 3.11 the image of a molten Cu droplet on a glassy carbon substrate is shown.
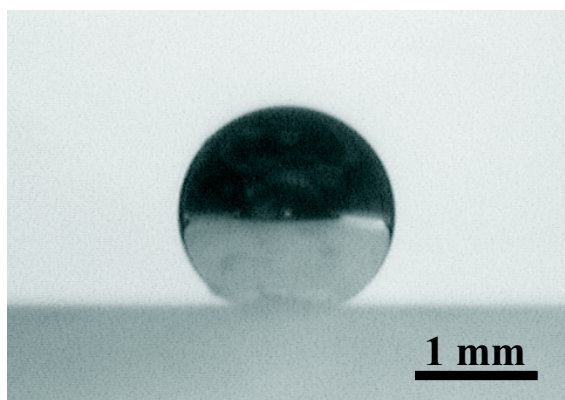
Figure 3.11: Image of a molten Cu droplet on a glassy carbon substrate. The final contact angle ($\theta = 144°$) in this non-reactive and immiscible system is reached in the first second after the melting.

This non-reactive and immiscible system has a contact angle $\theta = 144°$, which is reached during the first second of the wetting experiment. This angle is already the final contact angle and does not change with time. With the HTSDD experiments up to 180 seconds at a temperature of approx. 1100°C can be performed, before the parts of the device become too hot (temperatures up to 80 - 90 °C are reached at

the current feedthroughs). This big contact angle is clearly a non-wetting behavior, responsible for the bad mechanical adhesion of the Cu/C system in e.g. MMCs (metal matrix composites: copper matrix, carbon fibers).

A different situation is created by the usage of alloying elements in the copper. In the Figures 3.12 to 3.17 the commercially available brazing alloy CuABA[1] is used as drop material on the glassy carbon substrates. This is a typical example of reactive wetting (see Chapter 7.3 for a detailed description).
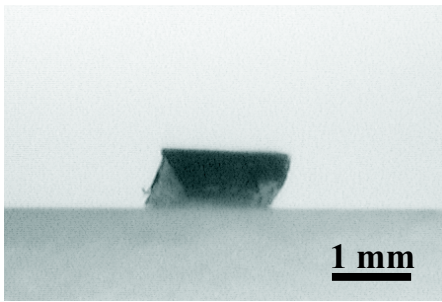
Figure 3.12: Image of the CuABA piece shortly before melting.
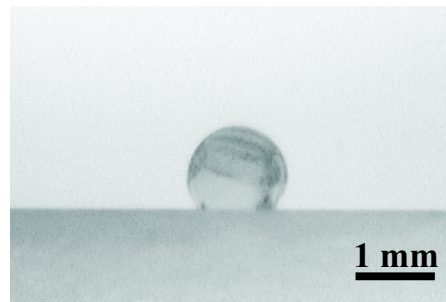
Figure 3.13: Image of the CuABA drop after melting, $\theta = 123°$.
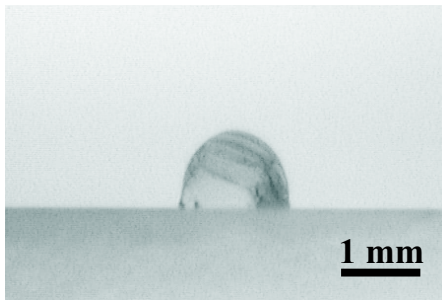
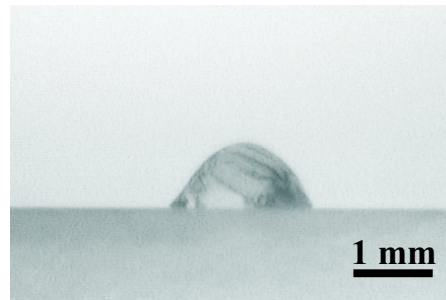Figure 3.14: Droplet evolution in time due to reactive wetting, $\theta = 82°$.

Figure 3.15: Droplet evolution in time due to reactive wetting, $\theta = 59°$.

These figures show the time dependence of the contact angle during a wetting experiment. In Figure 3.12 the unmolten CuABA piece is resting on the substrate. The begin of melting can be observed when the surface of the cylinder begins to deform. Then complete melting happens very fast (a few seconds) and a droplet like in Figure 3.13 is formed. With the automatic image acquisition the whole wetting experiment is documented and the contact angle can be measured at any time step.
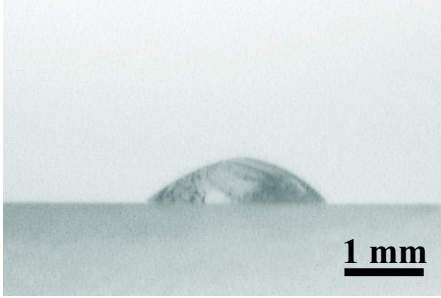
---

[1]Composition see Appendix F

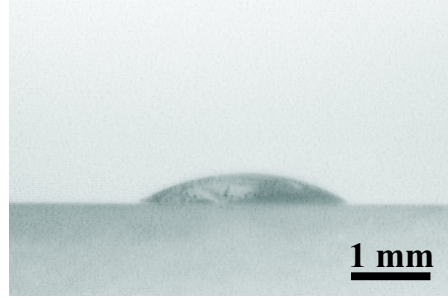*Figure 3.16: Droplet evolution in time due to reactive wetting, $\theta = 43°$.*

Figure 3.17: Droplet evolution in time due to reactive wetting, $\theta = 31°$.

The images in Figure 3.12 to Figure 3.17 are arbitrarily chosen for the description of the contact angle time evolution. The final contact angle in the CuABA/C system was found to be approx. 10°.

Chapter 4

Information from the liquid drop

Sessile drop experiments are a commonly used technique to derive characteristics of spreading and penetration phenomena. By making one single sessile drop experiment the following informations can be gained: contact angle, liquid surface energy and density of the liquid. These points will be discussed in detail in the next sections:

4.1 Contact Angle θ

The contact angle of the sessile drop is measured either by a software which recognizes the shape of the droplet, or by "hand". Additionally in the case of a spherical drop the contact angle can be calculated by the following expression:

$$\tan\left(\frac{\theta_{calc}}{2}\right) = \frac{H}{R} \tag{4.1}$$

where H is the height of the drop and R is the radius of the substrate contact area. The contact angle of Cu on vitreous (glassy) carbon can be found in literature with 139° to 145° [14]. The measurement in our HTSDD gave a value of 144° and calculating the contact angle from the height and the radius according Equation 4.1 leads to 147°, which is close to the values measured by other authors.

4.2 Liquid surface energy σ_{LV}

The liquid surface energy of four different metals in a wide temperature range (Melting points: In = 159°C, Pb = 327°C, Al = 660°C, Cu = 1083°C) was measured in

the HTSDD. The melting point of copper is the upper temperature limit of the HTSDD due to the stability of the ceramic distance spacer by now. The Macor® glass ceramic which was used has a continuous usage temperature of 800°C and a peak usage temperature of 1000°C [35].

An example of all relevant distances for determining the liquid surface energy of the sessile drop is shown in Figure 4.1.
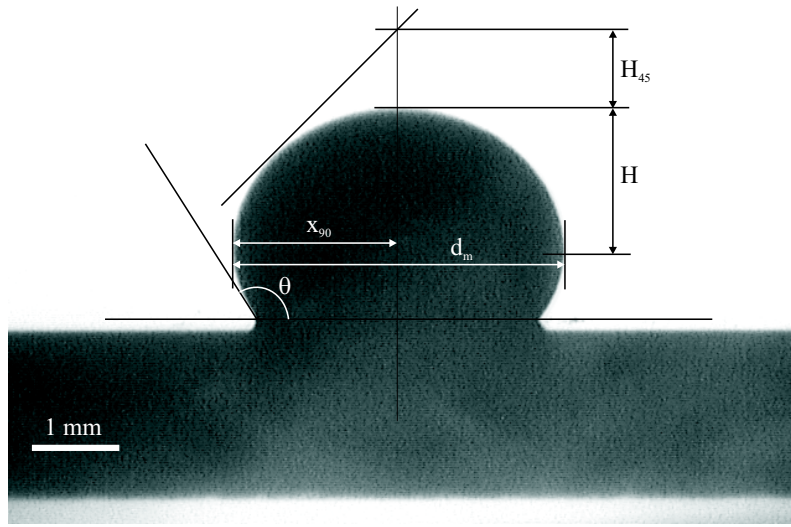

Figure 4.1: Image of the sessile drop, with all relevant parameters.

The exact horizontal line can easily be found by the reflection of the drop on the substrate surface. For the calibration of the scale the unmolten diameter of the metal disc was measured. By correlation of the measured diameters with the size of the image (640×480 pixel) it is possible to derive a mm/px relation for the following distance measurement in the droplet image.

A calibration of the different magnifications of the optic was done and the derived curve is shown in Figure 4.2.

Here the conversion factor in mm/px (y-axis) is given for the different magnifications (x-axis). The distance between the sample and the optic is 175 mm. The measurement of the geometric distances in pixel can be done by any software. The multiplication with the conversion factor leads to the real distances in mm. For the error estimation a uncertainty in the measurement of two pixels was assumed and
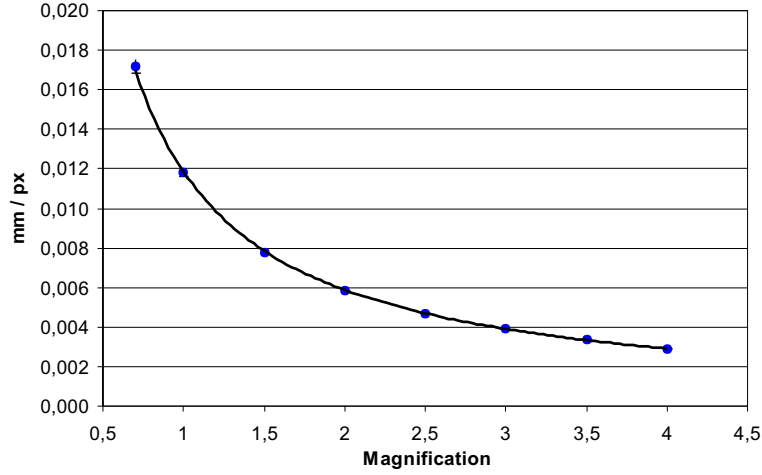
Figure 4.2: Magnification curve of the optic. The x-axis shows the magnification and the y-axis gives the mm/px for the image.

error bars are drawn in Figure 4.2. They can just be seen for the first two dots, the other ones are too close to the dots to be visible in the image.

The fitting curve was found to be a power law of the form:

$$y = 0,0118 \; x^{-1,0112} \tag{4.2}$$

As it can be seen in Figure 4.2, this power law curve fits very well to the experimental values. The coefficient of determination[1], R^2, which is a factor for the correlation between measured points and fitted curve, has the numerical value of 0,9998.

The measurements were performed with big drops (several mm) to get flattened drops due to the gravitational force. Images of the drops were taken right after melting and the drop geometry was carefully measured. The surface energy was calculated with both models described in Chapter 2.3. The uncertainty $\Delta\sigma_{LV}$ was taken into consideration for an error of distance measurement of one pixel in the image (640×480 px). If y is a function depending on n uncorrelated variables, $y = y(x_1 \ldots x_n)$, then the uncertainty Δy of the function can be calculated from the uncertainties Δx_i of the variables, via Gauss law of error propagation

---

[1]Definition of the coefficient of determination see Appendix G

$$\Delta y = \sqrt{\sum_{i=1}^{n} \left(\frac{\partial y}{\partial x_i} \right)^2 \Delta x_i^2} \tag{4.3}$$

where $\partial y / \partial x_i$ is the partial derivative of y for the i-th variable.

In the present case the liquid surface energy depends on two variables, $\sigma_{LV} = \sigma_{LV}(x_{90}, H_{45})$ or $\sigma_{LV} = \sigma_{LV}(d_m, H)$, according to the two different models. The calculated values for the surface energy as well as the literature values are presented in Table 4.1. The uncertainty Δy of the different models is also given in this table.

	θ [°]	σ_{LV} [mJ/m^2] [1]	σ_{LV} [mJ/m^2] [2]	σ_{LV} [mJ/m^2] [3]
Cu	144	1355	1028 ± 211	1342 ± 106
Pb	128	462	541 ± 113	413 ± 23
In	154	555	646 ± 91	523 ± 39
Al	147	867	693 ± 94	654 ± 68

[1] Literature values [14]
[2] model according to [14, 24]
[3] model according to [26, 27]

Table 4.1: Measured contact angles and calculated liquid surface energies of different metals on glassy carbon. The uncertainty Δy of the models is given in the appropriate column.

One can see that the model of Koshevnik [26, 27] provides a better agreement with literature due to the assumption of small droplets (Chapter 2.3). For aluminum both liquid surface energy values are quite far away from literature, but this can be explained by oxidation effects of Al, since the surface energy σ_{LV} of liquid oxides is less than the surface energy of the pure metal. Many values of pure oxides and pure metals can be found in [14] and in all cases the σ_{LV} values for the oxides are significantly lower than the values for the pure metal. In Table 4.2 some values are summarized.

One can see that the literature value for Al_2O_3 is much closer to our measured value of the Al drop in our HTSDD. This leads to the conclusion that oxidation during the wetting experiments happens and therefore the measurement was done actually on an oxide layer on the pure Al. In addition it can be said that measuring the appropriate surface energy of a pure metal indicates that this metal oxidizes very

metal	$\sigma_{LV}\,[mJ/m^2]$	oxide	$\sigma_{LV}\,[mJ/m^2]$
Al	867	Al_2O_3	630
Pb	462	PbO	132
Fe	1855	FeO	545
Co	1884	CoO	550
Cr	1628	Cr_2O_3	812

Table 4.2: Surface energies of liquid metals and oxides at their melting point. The surface energy of the oxide is always lower than the surface energy of the pure metal [14].

slow, because of the same vacuum conditions during all different experiments in the HTSDD.

4.3 Density of the liquid drop

The density of the liquid is also a value which can be derived by profile measurement of a symmetrical sessile drop. The volume of the drop is calculated from the droplet profile and by knowing the original mass, the density is derived. There has to be no significant loss of mass due to evaporation for an accurate measurement.

Similar to the measurement of σ_{LV} there are two ways for the estimation of the volume: measuring the drop profile coordinates and numerical integration by using image analysis techniques or, alternatively, by an estimation according the following Equation 4.4:

$$V = r^2\pi \left(\frac{2b}{\beta} - \frac{2b^2\sin\theta}{x_{90}\beta} + H \right) \tag{4.4}$$

where H is drop height and b, x_{90}, β are the same variables as in Chapter 2.3 (see also Figure 2.4).

4.4   Mass loss of the liquid

The assumption of the previous section, no mass loss due to evaporation, is not fully satisfied in real experiments. During the wetting experiments the temperature reaches about 1100°C. Under the high vacuum condition of the system this temperature leads to evaporation already. For the most wetting experiments in this thesis the CuABA active brazing alloy was used, which is an alloy composed of 92,77wt% Cu, 3wt% Si, 2wt% Al and 2,25wt% Ti. In this case it is important to take care of the vapor pressure of the individual elements.

The theoretical mass loss was calculated with two different models: an evaporation table [36] and the formula after Knudsen [37]. The time for the wetting experiments is about 60 seconds and the droplet is assumed to be a sphere with a radius of 1 mm (leading to an evaporation surface of about 12,6 mm^2).

4.4.1   Evaporation rate

The evaporation rate for the mass loss calculation is given in Appendix E, and was taken from [36, 38]. In this graph the evaporation rate in $[g\ cm^{-2}s^{-1}]$ is plotted for several elements depending on the temperature. In our case the evaporation of pure copper was calculated due to the high copper content in the brazing alloy. The evaporation temperature was approximated to be 1100°C, which is a little bit higher than the melting point of copper ($T_M = 1084$°C).

With these parameters the evaporation table gives an evaporation rate of $5,48 \times 10^{-6}\ \frac{g}{cm^2 s}$ or $5,48 \times 10^{-5}\ \frac{mg}{mm^2 s}$. By multiplying this value with the surface of the droplet and the time for the experiment, one gets the total amount of mass loss, 0,04 mg.

4.4.2   Knudsen formula

For the evaporation of liquids into the gas phase the formula according to Hertz and Knudsen is valid [37, 38], which describes the amount of particles evaporating from the liquid or solid.

$$\frac{dN}{A\,dt} = j = \frac{p_D(T)}{\sqrt{2\pi m k_B T}} \tag{4.5}$$

With:

A = droplet surface

j = particle $m^{-2}s^{-1}$

p_D = vapor pressure [Pa] depending on temperature T

m = particle mass (for copper = $1{,}0552 \times 10^{-25}$ kg)

k_B = Boltzmann constant = $1{,}38 \times 10^{-23} \frac{J}{K}$

T = Temperature in [K]

With this calculated particle flow j, again the mass loss during the evaporation experiment is derived. The diagram for the vapor pressure of Cu (and other elements) is given in Appendix E. At 1100°C the vapor pressure for copper is $4{,}61 \times 10^{-2}$ Pa. By inserting the proper values into Equation 4.5 the particle flow j = $4{,}11 \times 10^{20} \frac{1}{m^2 s}$, which is equal to $4{,}34 \times 10^{-5} \frac{mg}{mm^2 s}$. This corresponds to a total mass loss of 0,03 mg of the droplet.

In the last two subsections the mass of the evaporated element was estimated on the one hand with an evaporation table and on the other hand with kinetic gas theory equations. Both approaches lead to an evaporation rate in the range of $10^{-5} \frac{mg}{mm^2 s}$, leading to a total amount of mass loss for the droplet of 0,03 - 0,04 mg in 60 seconds. The actual mass loss during the wetting experiments was calculated from the mass difference before the wetting test (mass of the brazing alloy and the substrate separately) and after the wetting test (mass of the substrate with the molten alloy together). This led to a weight loss of about 2 mg, which is about 50 times higher than the calculated one. Since the evaporation rate is strongly (exponentially) dependent on the temperature of the source, a small change in the temperature leads to a strong increase in the mass flow. In our calculation a temperature enhancement of 50°C leads to an increase of the evaporated mass to 0,08 mg, decreasing the difference to the real experiment to a factor of 20. A temperature difference of 240°C to the temperature of 1100°C would evaporate the complete mass of 2 mg in 60 seconds.

The composition of the CuABA wire was checked by EDX before and after the wetting experiment, and the result is presented in Table 4.3. Here the composition in at% of the CuABA wire before and the CuABA droplet after melting is shown.

	Al [at%]	Si [at%]	Ti [at%]	Cu [at%]
CuABA wire	10,0	7,9	2,5	79,6
CuABA droplet	5,1	10,7	10,4	73,8

Table 4.3: EDX measurement of the CuABA wire before and the CuABA droplet after the wetting experiment.

The pressure in the chamber during the wetting experiment was in the region of 2 - 5 × 10^{-3} Pa. At the temperature of about 1100°C the vapor pressure of the components of the CuABA brazing alloy is: 2×10^{-5} Pa for Ti, 6×10^{-4} Pa for Si and 5×10^{-1} Pa for Al. This means that at the temperature and the pressure in the experiment Al is far below its vapor pressure and evaporates already. Ti and Si are still above their vapor pressure and in the solid phase. This is in agreement with Table 4.3, where Al shows a mass loss of the half of the original mass but Si and Ti have higher concentrations (due to the loss of the other components).

For the calculation of the real masses of the CuABA elements in the alloy the at% values from Table 4.3 were converted into wt% and are shown in Table 4.4.

	Al [wt%/mg]	Si [wt%/mg]	Ti [wt%/mg]	Cu [wt%/mg]
CuABA wire	4,8 / 1,68	3,9 / 1,37	2,1 / 0,74	89,2 / 31,33
CuABA droplet	2,4 / 0,79	5,4 / 1,78	8,9 / 2,94	83,3 / 27,49

Table 4.4: The same EDX measurement of the CuABA as in Table 4.3, but this time converted to wt% and masses of the droplet.

For the CuABA wire the original mass of about 35 mg was used and for the CuABA droplet after the wetting experiment the mass of about 33 mg (evaporation of about 2 mg, see above) was used for the calculation of the individual masses of the CuABA components Al, Si, Ti and Cu (see again Table 4.4). This is also an indication for the evaporation of Al and Cu during the wetting experiments in the HTSDD chamber, although some uncertainties from the EDX measurements have to be taken into consideration (accuracy, uniformity of the sample).

The stability of the Sigradur substrate during the wetting experiments was tested by a heat treatment of the carbon substrate alone in the HTSDD (with the same parameters as the wetting experiments: about 1100°C and 60 seconds). The weight of the Sigradur substrate was measured before and after the annealing, with the result of no significant mass loss. The evaporated mass during the wetting experiments therefore results just from the molten CuABA droplet, and is hardly affected by the Sigradur substrate.

Chapter 5

Physical Vapour Deposition - Sputtering

The applications of thin films in industry and science are manifold. Thin films are used in optics for transmission and reflexion changes of glasses, semiconductor industry and materials science for tribology, hardness, corrosion and wear resistance. A big application is the usage of thin magnetic films for information storage, e.g. as harddisks in personal computers. In general, thin films are always used when different material properties between the surface and the bulk of a component are required. Also for the joining of different materials in a compound, thin films (then they are called interlayers) are of great technological interest.

In the present case, more precisely, the application of thin films as wetting promoters during brazing is of interest. Here the thin film should increase the wetting behavior of the liquid braze, resulting in a better joined compound.

5.1 Basics of the Sputtering process

Physical Vapour Deposition (PVD) means the deposition of a coating from the gas phase, including evaporation and sputtering. In the following we always refer to sputter deposition.

Atoms from a solid target (which is the coating material) are ejected into the gas phase by bombardment with energetic ions. Sputtering is driven by momentum transfer from these ions to the atoms in the target material. This non thermal

transfer to the gas phase is the big advantage of sputtering, because almost every material is suitable as target.

The ions for the sputtering process are supplied by a gas discharge in the vacuum chamber. The easiest way is to put a voltage between the target as cathode and the substrate as anode, with Ar as working gas, see Figure 5.1.
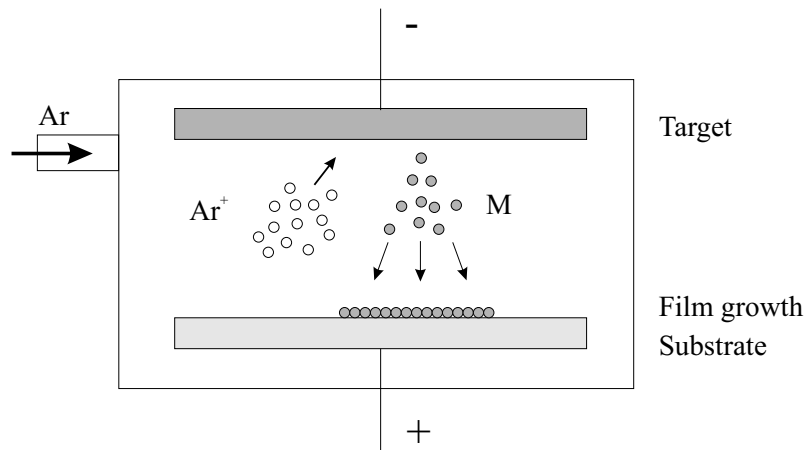
Figure 5.1: Schematic of the sputter process, M are the ejected target atoms.

Advantages of sputtering are:

- many substrate materials (metals, ceramics, glass)

- big variety of coating materials (metals, alloys, oxides, carbides, nitrides)

- good adhesion

- free choice of substrate temperature

Disadvantages of the sputtering process are:

- low deposition rate and film thicknesses

- high technical effort for achieving and maintaining the vacuum

- not suitable for complex geometries

The described advantages made sputtering a commonly used deposition technique. In the practical use a magnetron sputter system is favored, leading to a lower sputter

pressure (0,1 Pa instead of several Pa) by trapping the electrons from the plasma near the target with a B-field generated by permanent magnets. By using a RF (radio frequency) power supply, the sign of the anode-cathode voltage is changed at a high rate (13,56 MHz) which is necessary for semi-conductor and insulator targets to suppress charging. Sometimes for cleaning purposes an additional negative bias (up to - 200 V) on the substrate is used.

The PVD plant used in this work for the deposition of films was an ALCATEL SCM 451 with two magnetron sputter targets, DC and RF power supply and two gas inlets for reactive deposition of nitrides. A base pressure of approx. 10^{-5} Pa was achieved.

5.2 Reactive sputtering of stoichiometric and substoichiometric TiN films

TiN coatings are a candidate for wetting promoting thin films in the system C (in the modifications: graphite, CFC, . . .)/Cu(Cu-alloy). Literature gives evidence that the contact angle of Cu on TiN films depends on the nitrogen concentration in the coating, resulting in decreasing contact angles with decreasing nitrogen content. Almost complete wetting is reported for $TiN_{0,5}$ [14, 39]. Therefore stoichiometric and substoichiometric TiN films were deposited onto glassy carbon for wetting experiments. For reactive deposition of films two gas flow controllers are necessary: one for maintaining a constant Ar flow and one for a variable N flow. The Ar pressure was 0,23 Pa and the total pressure was recorded during the increase of the N flow. The pressure vs. nitrogen flow graph is shown in Figure 5.2.

One can recognize a significant increase in the total pressure at a certain nitrogen flow point. This point is the switch point of TiN sputtering. Below the switch point the growing TiN film absorbs all nitrogen atoms from the gas phase and the pressure stays constant. After the switch point there are too many nitrogen atoms to be absorbed by the film, hence the pressure is increased in the chamber. The nitrogen flow at this significant point is just enough to lead to a stoichiometric TiN coating. Nitrogen flows below the switch point are suitable for the deposition of substoichiometric $TiN_{x<1}$ films.
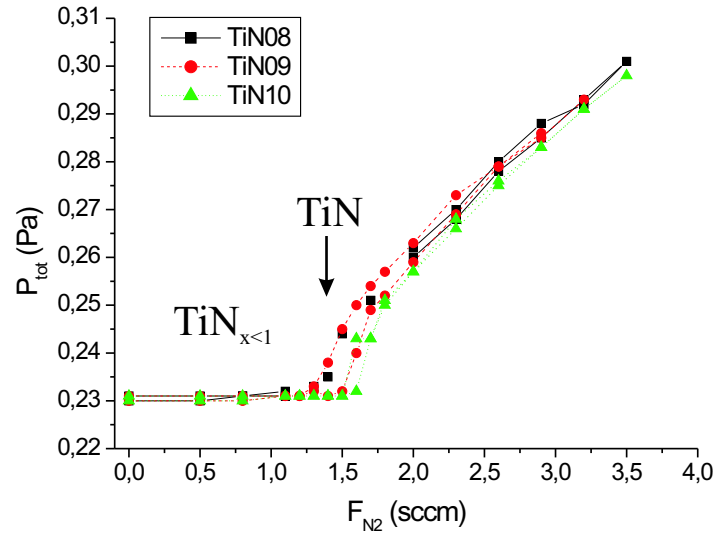
Figure 5.2: Total pressure vs. nitrogen gas flow.

In Figure 5.3 a golden TiN coating is shown, which gives indication that the coating is near the stoichiometric ratio. In contrast Figure 5.4 shows a gray substoichiometric TiN film.
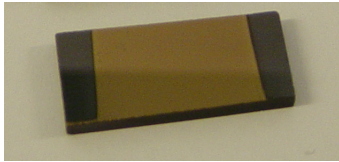
Figure 5.3: Stoichiometric TiN.
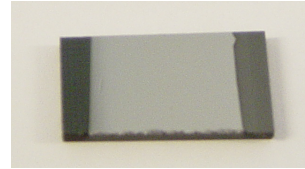
Figure 5.4: Substoichiometric $TiN_{0,3}$.

For the determination of the N and Ti content of the coatings Rutherford Backscattering (RBS) measurements were performed at the Max Planck Institute for Plasma Physics (IPP) in Garching. The results of these measurements are presented in Table 5.1 and Figure 5.5.

Five samples with the same Ar flow in standard cubic centimeters (sccm) but different N_2 flows were analyzed. The golden sample had a N/Ti ratio of 0,93 which proved the approximate stoichiometry of the TiN coating. By plotting the at% of Ti and N against the N_2 flow one can recognize the linear dependence of the atomic

	TiN22	TiN24	TiN25	TiN27	TiN30
Ar [sccm]	8,1	8,1	8,1	8,1	8,1
N [sccm]	1,3	1,1	0,9	0,7	0,5
N/Ti	0,93	0,54	0,30	0,15	0,08

Table 5.1: Flow parameters and N/Ti-ratio for different TiN_x coating.
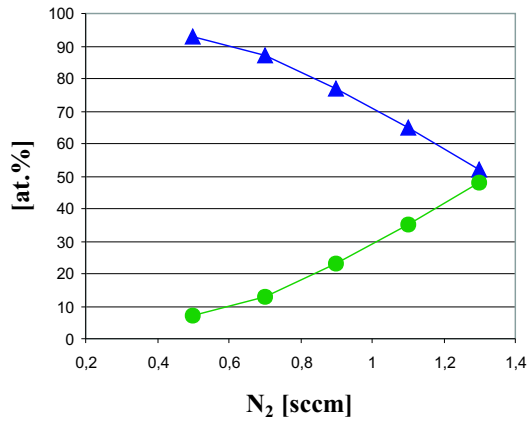
Figure 5.5: Ti and N at% against the N_2 flow.

percentage on the nitrogen flow. This proved the possibility of sputter deposition of each desired TiN_x stoichiometry in our PVD plant.

5.3 Comparison of reactively sputtered TiN with literature data

Reactive magnetron sputtering is a widely used technique to produce nitride- or oxide- coatings. A lot of literature can be found dealing with the different production routes for TiN coatings [40, 41, 42, 43, 44, 45, 46, 47, 48, 49]. Most of them report of sputtering in a mixed atmosphere of Argon and Nitrogen gas, with a fixed relation between the two amounts of gas. In many cases the measurement is done with a gas flow controller and the two gas flows are given in sccm.

Two papers found in literature are dealing with a model of reactive sputtering of TiN [50, 51], and give curves for the nitrogen partial pressure in the chamber in dependence of the nitrogen flow. This graph was extracted from the literature and inserted into Figure 5.6, where the comparison with the experimental results is shown.
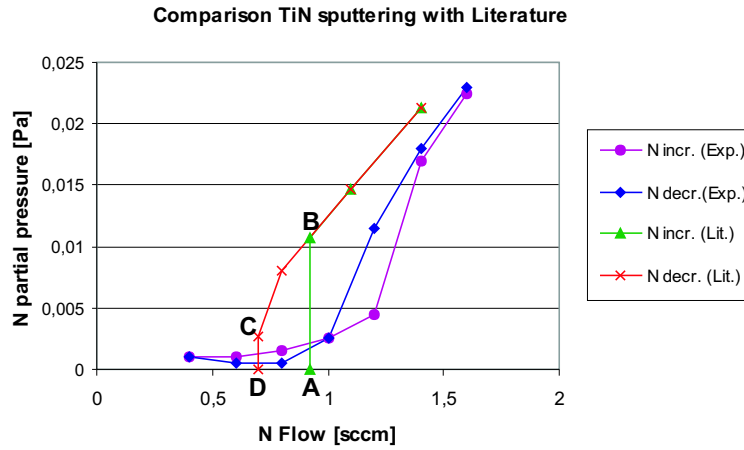
Figure 5.6: Nitrogen partial pressure over nitrogen flow. The reactive sputtering parameters in our PVD plant is compared with values found in [50, 51].

In Figure 5.6 the experimental and the literature partial nitrogen pressures are given for increasing (incr.) and decreasing (decr.) nitrogen flow. In each of the two data sets a hysteresis between increasing and decreasing the nitrogen flow is visible. According to [50, 51] the following processes are involved:

Increasing the nitrogen flow over point A results in a nonlinear increase of the formation of nitride at the target. When the target gets partially nitrided, the nitrogen consumption decreases. Thus, less nitrogen is gettered and the nitrogen partial pressure is increased. This increase in nitrogen partial pressure will cause a further increase of the nitride formation at the target. Then even less nitrogen is gettered and the nitrogen partial pressure increases further, and so on. A runaway situation emerges that shifts the operating point from A to B. An analogous situation appears if the nitrogen flow is decreased. Reaching point C (coming from higher flow values) will cause a similar runaway situation that shifts the operating point from C to D.

In [50, 51] the following equipment and parameters were used: a MRC rf-diode sputtering system SEM-8620, the Ti target had a diameter of 127 mm and the TiN was sputtered in a mixture of argon and nitrogen. The ratio between them was controlled by mass flow controllers and the total sputtering pressure was kept constant at 1,33 Pa. These parameters differ from those used in our experiments (see above). Nevertheless, the match between our results and the literature results is clearly visible in Figure 5.6, which shows the hysteresis in both data sets, although absolute values are slightly shifted against each other.

Chapter 6

Carbon with Interlayers

6.1 Surface energy of carbon modifications

The surface energy of carbon is strongly dependent on the modification which is used. There is a big difference between graphite, vitreous carbon, diamond and pyrolytic graphite. In the literature the following values for the surface energy σ_{SV} were found: The graphite basal plane has a σ_{SV} of about 150 mJ/m^2, whereas the planes perpendicular to the basal plane has values of about 500 mJ/m^2 [14, 52]. For vitreous carbon σ_{SV} was found to be 32 mJ/m^2 and for diamond values of about 4000 mJ/m^2 are reported [14]. Also for the basal plane of pyrolytic graphite a high value is reported, 1139 mJ/m^2 in [53].

The surface energy of the Sigradur®G glassy carbon substrates was measured by ourselves, values between 37 - 54 mJ/m^2 were obtained [54]. A sessile drop technique was used and the calculation method after *Owens et al.* [55] was applied. Here the contact angle of at least two different liquids with known surface energies σ_{LV} on the unknown solid substrate is measured.

According to [55] the work of adhesion can be written as:

$$W_a = 2\sqrt{\sigma_{SV}{}^d\,\sigma_{LV}{}^d} + 2\sqrt{\sigma_{SV}{}^p\,\sigma_{LV}{}^p} \tag{6.1}$$

where d and p means the dispersive and polar part of the surface energy, respectively. Inserting Equation 6.1 into Equation 2.5 leads to

$$\sigma_{LV}\left(1 + \cos\theta\right) = 2\sqrt{\sigma_{SV}{}^d\,\sigma_{LV}{}^d} + 2\sqrt{\sigma_{SV}{}^p\,\sigma_{LV}{}^p} \tag{6.2}$$

with some rearrangement this leads to the following expression:

$$\frac{1+\cos\theta}{2}\frac{\sigma_{LV}}{\sqrt{\sigma_{LV}{}^d}} = \sqrt{\sigma_{SV}{}^p}\sqrt{\frac{\sigma_{LV}{}^p}{\sigma_{LV}{}^d}} + \sqrt{\sigma_{SV}{}^d} \qquad (6.3)$$

which can be considered as a linear equation of the form

$$y = k \cdot x + d \qquad (6.4)$$

with

$$y = \frac{1+\cos\theta}{2}\frac{\sigma_{LV}}{\sqrt{\sigma_{LV}{}^d}}, \quad k = \sqrt{\sigma_{SV}{}^p}, \quad x = \sqrt{\frac{\sigma_{LV}{}^p}{\sigma_{LV}{}^d}} \quad \text{and} \quad d = \sqrt{\sigma_{SV}{}^d}. \qquad (6.5)$$

By knowing the polar and dispersive part of the liquid surface energy σ_{LV}, one can calculate $\sigma_{SV}{}^p$ from the slope of the straight line and $\sigma_{SV}{}^d$ from the intersection of the straight line with the y-axis. The measurement was done with three test liquids, the values of their surface energies are given in Table 6.1.

liquid	$\sigma_{LV}{}^p\,[mJ/m^2]$	$\sigma_{LV}{}^d\,[mJ/m^2]$	$\sigma_{LV}\,[mJ/m^2]$
distilled water	51,0	21,8	72,8
ethylene glycol (EG)	16,8	30,9	47,7
EG:water=50:50	41,1	20,51	61,6

Table 6.1: The three test liquids with known $\sigma_{LV}{}^p$ and $\sigma_{LV}{}^d$ values for the measurement of the surface energy σ_{SV} of a substrate [56].

The result of the measurement on Sigradur®G is shown in Figure 6.1.
The three test liquids give three points in the graph (squares in Figure 6.1) which are on one straight line, representing Equation 6.3. A good accuracy is given because the points are close to the straight line.

Our measurements are close to the measurements of vitreous carbon [14]. This is sound due to the fact that these two names (glassy, vitreous) are used for the same carbon modification. They have a highly disordered structure, consisting of curved carbon planes showing a fullerene-related structure [57]. An image of glassy carbon
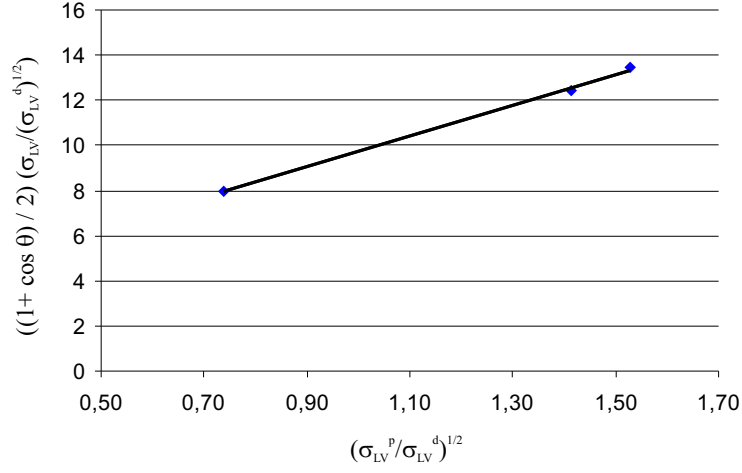
Figure 6.1: Owens-Wendt plot for the determination of the liquid surface energy.
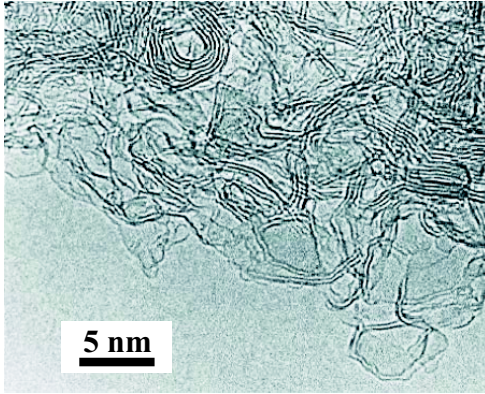
Figure 6.2: TEM image of the structure of the glassy carbon - Sigradur [57].
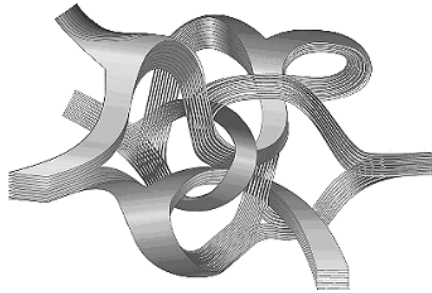
Figure 6.3: Proposed structure of glassy carbon [58, 59].

from the manufacturer is given in Figure 6.2 and the proposed microstructure is shown in Figure 6.3.

This microstructure from the manufacturer and from literature was confirmed in former work [60] and a TEM image is given in Figure 6.4.

The low surface energy of the glassy carbon is one reason for the bad wetting of Cu on this material.
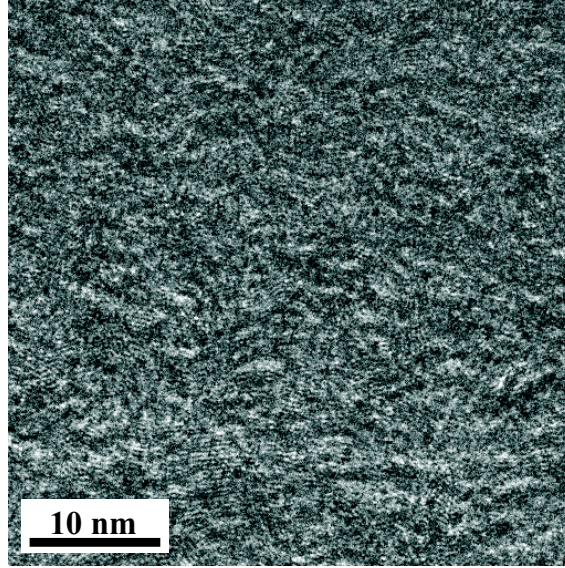
Figure 6.4: TEM image of the structure of glassy carbon - Sigradur® G. In contrast to Figure 6.2 this image was taken from a thicker part of the sample.

6.2 Wetting experiments

On a glassy carbon substrate wetting experiments with pure Cu and with the CuABA brazing alloy were performed. In the case of pure Cu a complete non-wetting behavior was obtained, with a contact angle of approx. 144°. The equilibrium contact angle in the case of CuABA was approx. 10°. The time evolution of the contact angle in the CuABA/C system and the mechanism of it (reactive wetting) will be explained in detail in Chapter 7.3.

In Figures 6.5 and 6.6 the images obtained by the HTSDD are given, showing the contact angle of Cu on C and the contact angle of CuABA on C, respectively.

The completely different wetting regimes (non-wetting and wetting - by reactive wetting) can be seen in these two images. The CuABA/C sample was prepared in cross section and investigated by means of Scanning Electron Microscopy with Energy Disperive X-Ray Detection (SEM/EDX). Two SEM images of the interfacial region between CuABA and glassy carbon are given in the Figures 6.7 and 6.8.

Both images were taken from the same sample. At first sight the different thicknesses of the reaction layer is visible, in Figure 6.7 the thickness is approx. 4 μm, in Figure 6.8 the thickness is approx. 2 μm. Despite this difference the images in both
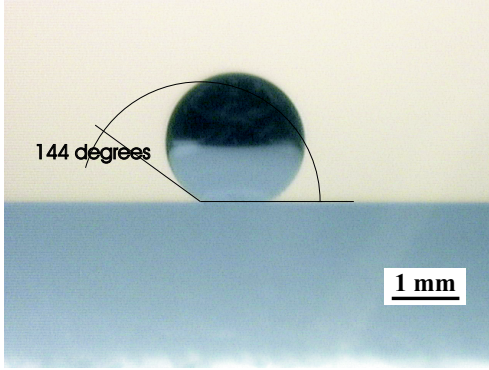
Figure 6.5: HTSDD image of liquid Cu on glassy carbon. The contact angle in this non-wetting case is approx. 144° and is reached in less than one second.
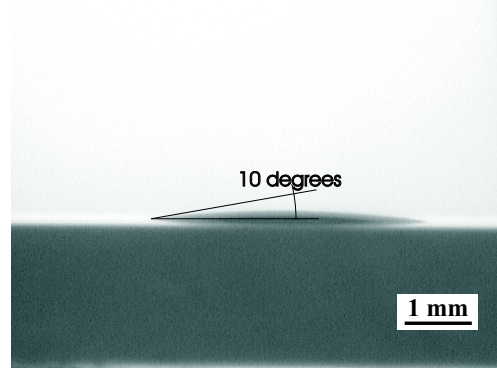
Figure 6.6: HTSDD image of liquid CuABA on glassy carbon. The equilibrium contact angle of approx. 10° is reached in about 80 seconds.
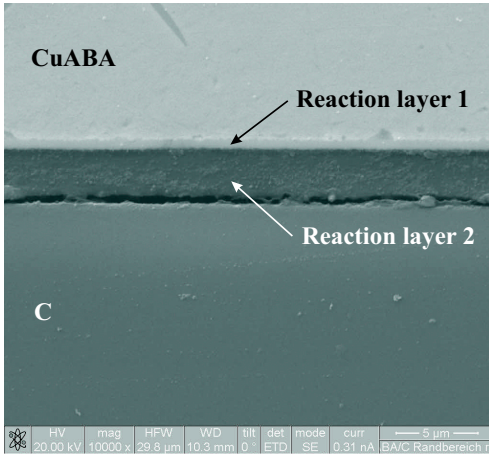
Figure 6.7: SEM image of the interface CuABA/C. The formation of two reaction layers and a detachment in the joint is visible.
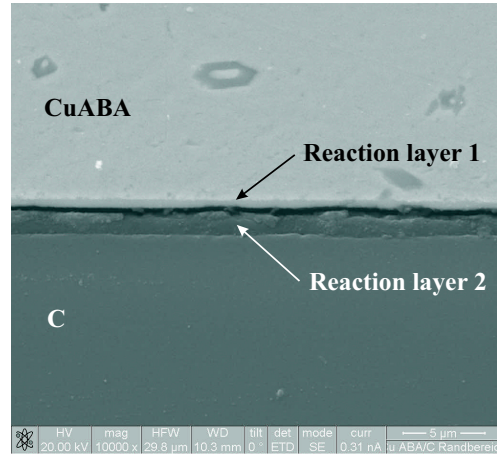
Figure 6.8: SEM image of the interface CuABA/C. In contrast to Figure 6.7 the detachment in the joint is between the two reaction layers.

cases show two different reaction layers, a thinner one near the CuABA brazing alloy and a thicker one near the carbon side. After the wetting experiments the solidified droplet adhered well to the glassy carbon substrate, but the microstructural investigations showed delaminations in the joint. They occur either between the reaction layers or between reaction layer 2 and the carbon substrate.

EDX measurements of these two reaction layers were performed. The composition

of the reaction layers is given in Table 6.2.

	Reaction layer 1		Reaction layer 2	
Element	wt%	at%	wt%	at%
C	42,1	73,0	63,4	82,1
O	4,1	5,2	10,4	9,9
Si	0,7	0,5	0,2	0,1
Ti	35,8	15,6	14,7	4,9
Cu	17,3	5,7	11,3	3,0

Table 6.2: EDX results of the two different reaction layers. A significantly higher Ti content can be seen in reaction layer 1.

The EDX results showed a significantly higher Ti content in the reaction layer 1, which is nearer to the CuABA brazing alloy. Si was detected in the precipitations visible in both images.

The alloying element Ti in the CuABA brazing alloy is responsible for the significant wetting transition from non-wetting in the pure Cu case to the excellent wetting in the CuABA case. The Ti forms a reaction layer on the carbon surface which is much better wetted by the liquid drop. The addition of elements in the drop material which form good wettable reaction layers is a well known method to improve the wetting of the liquid [14].

6.3   Coatings on Carbon

In a first preliminary experiments different coatings in several thicknesses were sputter deposited and the wetting behavior of a pure Cu droplet was investigated. The coating materials were: Mo, Ti, TiN, W, Cr, Al and AlN, with each of them in the thicknesses of 10, 20, 50 and 100 nm. In the case of TiN and AlN it has to be mentioned that the coatings were sputtered in a pure nitrogen atmosphere and no stoichiometric analysis was done to check the composition. Due to the non-golden appearance of the TiN it seems that it is not real stoichiometric TiN but some kind of mixture. The same is true for the AlN coating. This was done before the nitrogen gas flow controller was implemented into the PVD plant. An overview with optical images of all samples described above is given in Table 6.3.

These experiments were done in an evaporation plant by resistive heating, prior to the finalization of the HTSDD. So no in-situ observation of the experiment was possible, the optical images were taken afterwards. The images showed in the most cases (W, Cr, Al and AlN) non-wetting and delamination. In the W case the Cu droplet wets the coating partially but also leads to the disappearance of the W coating by solution of W into Cu. The Cr, Al and AlN coatings are not stable during the experiment.

In this study just the Mo and the Ti films, preferentially the thicker coatings, show wetting behavior with the Cu droplet leading to contact angles less than 90°, and very low values for the Mo coatings. Therefore these two elements can be seen as wetting promoting thin films. The results for the TiN films are not too reliable due to the above mentioned sputter method but according to literature and the project partner, TiN films are of great interest and have the property to enhance wetting.

Table 6.3: Overview of wetting experiments with different interlayers.
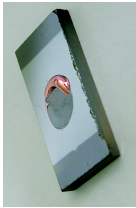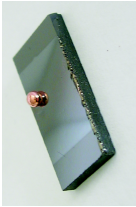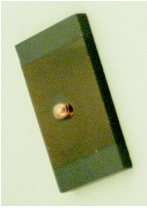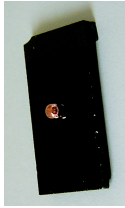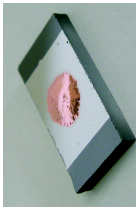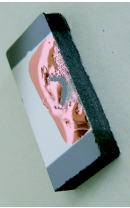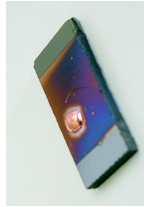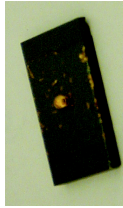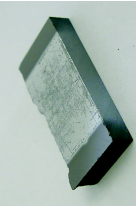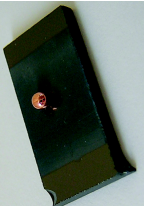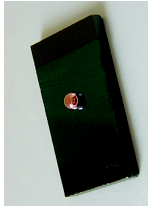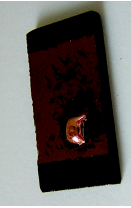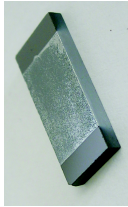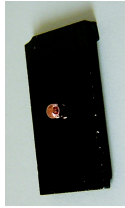
nm	Mo	Ti	TiN	W	Cr	Al	AlN
10							
20							
50							
100							

Chapter 7

Substoichiometric TiN as wetting promoter

The mechanism of reactive sputtering of TiN coatings has been presented in Section 5.2. There it was shown that stoichiometric TiN films can be achieved by using two mass flow controllers, one for the argon and one for the nitrogen flow. Substoichiometric TiN_x films were then generated by reducing the nitrogen flow into the vacuum chamber. With this procedure the production of stoichiometric TiN and substoichiometric TiN_x coatings for further investigation was carried out.

7.1 Introduction to TiN

The application of TiN as wetting promoting thin films in plasma facing components has been suggested by the project parter ARI Ansaldo Ricerche S.p.A., Italy. They performed earlier experiments with Chemical Vapor Deposition (CVD) TiN which seems to improve the wetting of the brazing alloy on CFC, but no detailed study was done in this case.

In literature [14, 39] some information about Cu and Cu-alloys on TiN_x films can be found. The contact angle of pure copper on TiN is in the non wetting regime ($\theta =$ 96° - 110°). Two ways are reported in literature to decrease the contact angle and improve the wetting: the stoichiometry of the coating is one important factor and the addition of carbide forming elements into the pure Cu is the other one. By using substoichiometric TiN_x films the contact angle can be decreased to values between

46° - 60°. The addition of 5 at% Ti to Cu leads to a contact angle on TiN of only 12°. So commercial Cu brazing alloys often have additions of elements like Ti and Si (the elemental composition of the CuABA brazing alloy is given in Appendix F).

7.2 TiN experiments

The brazing alloy used in the plasma facing components is the commercial CuABA-alloy[1]. Therefore all following experiments were done with this brazing alloy.

For the investigation of the influence of the substoichiometry of the TiN_x coating a wettability study of CuABA on different TiN coatings with several substoichiometries was performed. For this wetting study the samples given in Table 7.1 were produced:

Sample	Ar [sccm]	N_2 [sccm]	thickness	stoichiometry x
Ti	8,1	0	100 nm	0
TiN12	8,1	1,2	100 nm	1
TiN10	8,1	1,0	100 nm	0,6
TiN08	8,1	0,8	100 nm	0,3
TiN06	8,1	0,6	100 nm	0,15

Table 7.1: Sample parameters of the wettability study of CuABA on different TiN_x stoichiometries.

The stoichiometry of the samples was checked by RBS and the values for x are given in the last column of Table 7.1. Additional one pure carbon sample was tested as reference material without an interlayer. A piece of CuABA was used as brazing alloy. Images of the samples after the wetting study are given in Figures 7.1 - 7.6. There the solidified CuABA drops on the samples are shown.

From these images one common feature is visible: the wetting in the final stage is very good for all samples, with contact angles of about 10°. But the time for reaching the final contact angle differs significantly which will be discussed later. The solidified drop has a highly spherical shape which indicates uniform wetting.

---

[1]Composition and material parameter see Appendix F
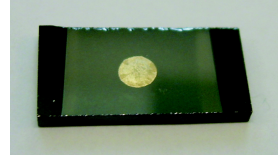
Figure 7.1: CuABA on glassy carbon.

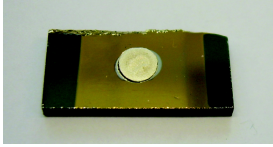Figure 7.2: CuABA on 100 nm Ti coating.

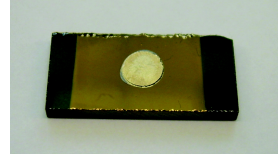
Figure 7.3: CuABA on TiN12.

Figure 7.4: CuABA on TiN10.
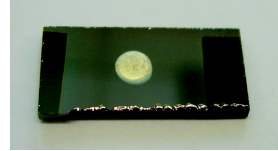

Figure 7.5: CuABA on TiN08.

Figure 7.6: CuABA on TiN06.

In some of the samples the solidified drop detached from the substrate, leading to a crater in the carbon (see Figure 7.5). This happens in the last stage of cooling in the HTSDD and may be attributed to stresses in the sample. Repeating the experiments leads to uncorrelated results, the detachment or the non-detachment on the same sample happens arbitrarily. The very fast cooling process (from 1100°C to room temperature in approx. 10 minutes), which seems to be responsible for the detachment, should be optimized to reduce the stresses.

For the time evolution of the contact angle of the substoichiometric TiN_x films the images during the wetting experiment were analyzed and the value of the contact angle was plotted vs. the time. This was done for all samples and the results are shown in Figure 7.7, where the difference in the time evolution is clearly visible. The slowest wetting of CuABA occurs on the pure carbon sample without any interlayer. Here the time for reaching the final contact angle is about 80 seconds. The deposition of any kind of interlayer leads to a strong decrease in the wetting time. A pure 100 nm Ti interlayer reduces the wetting time to about half the value
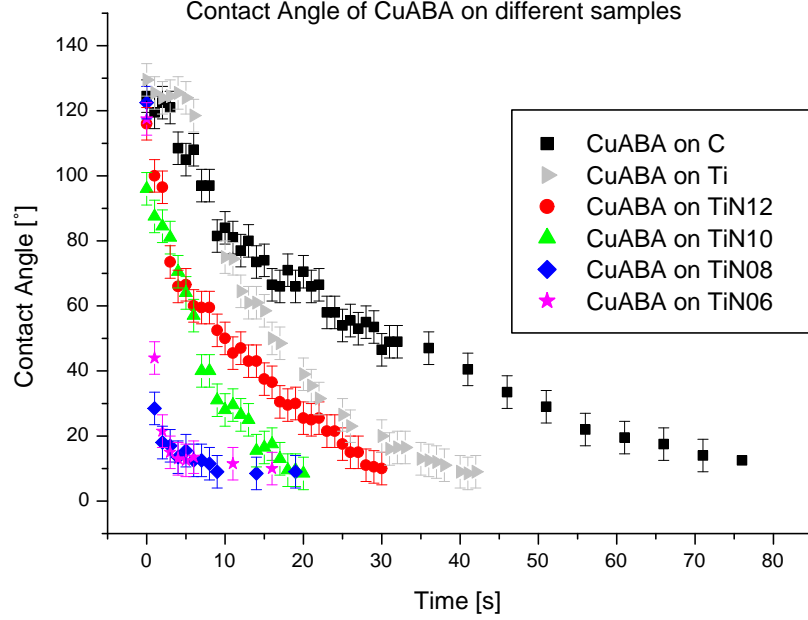
Figure 7.7: Contact angle study of CuABA on different samples. The reduction of wetting time can be seen for all interlayers, also the clear dependence on the stoichiometry of the TiN_x film is visible.

of pure carbon. The usage of TiN or substoichiometric TiN_x coatings leads to a further decrease in wetting time. The stoichiometry of the TiN_x coatings also has a strong influence on the wetting behavior. A reduction of the nitrogen content in the coating leads to faster wetting of the CuABA brazing alloy, resulting in reaching the final contact angle after 10 seconds for the $TiN_{0,15-0,30}$ film. These results are in agreement with the literature [14, 39], where a correlation between film stoichiometry and contact angle is reported.

To quantify the dependence of the wetting time on x, the time $\tau_{20°}$, to reach a contact angle of 20°, is plotted in Figure 7.8 vs. the stoichiometry of the film.

The x-axis is the stoichiometry of the film and on the y-axis $\tau_{20°}$, which is the time for the contact angle to reach 20°, is drawn. For the TiN_x samples a linear dependence of $\tau_{20°}$ on the x values is visible.
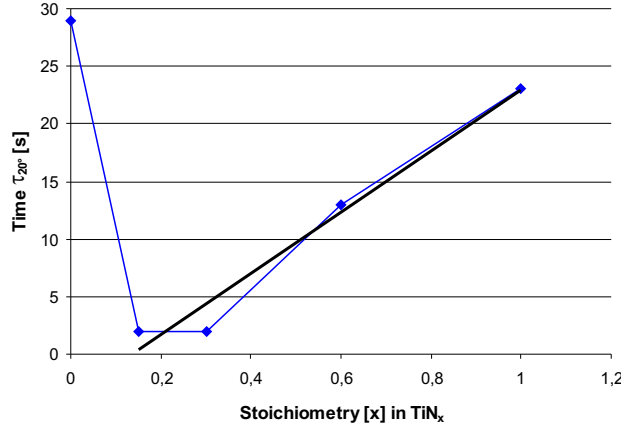
Figure 7.8: Time $\tau_{20°}$ for reaching a contact angle of 20° vs. the TiN stoichiometry. A linear dependence between time and stoichiometry is visible.

For brazing trials of CuABA on carbon the following two interlayers were used: the stoichiometric TiN coating and the substoichiometric TiN_x with the fastest wetting characteristics. The aim is to find a difference of the two coatings and improve the wetting behavior of the CuABA brazing alloy.

7.3 Reactive Wetting

The previous section (CuABA on TiN) is an example for reactive wetting. This means the alloying of the drop with elements that form a reaction layer at the solid/liquid interface. This reaction layer should enhance the wetting behavior. A more detailed view of this topic is given next.

7.3.1 Introduction to Reactive Wetting

The literature [14] divides reactive wetting into the case of simple dissolution of the solid in the liquid and the case of the formation of a 3D compound (reaction layer) at the interface.

Reactive wetting is divided as follows:

   I. Dissolution wetting

      1. σ_{LV} and σ_{SL} values insensitive to dissolution

      2. σ_{LV} and σ_{SL} values sensitive to dissolution

  II. Formation of 3D compound

      1. Reaction product wettability

         i. Reaction product more wettable than the substrate

        ii. Reaction product less wettable than the substrate

      2. Spreading kinetics

         i. Reaction limited spreading

        ii. Diffusion limited spreading

In the first case (I.1.) the dissolution of the solid into the liquid is assumed not to change significantly the surface and interface energies, σ_{LV} and σ_{SL}. Here only the geometry at the triple line is changed. In the second case (I.2.) the interfacial energies are modified due to dissolution of small quantities of tensio-active species of the solid, but the solid/liquid interface is assumed to remain nearly flat. These two cases are shown in Figure 7.9.
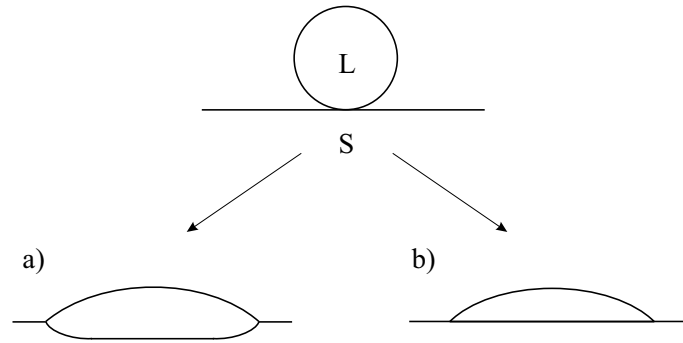

Figure 7.9: The two cases of dissolutive wetting: a) Dissolution of the solid modifies the geometry of the triple line. b) Modification of the interfacial energies of the system, while the S/L interface remains macroscopically planar.

Interfacial reaction causes the formation of a dense 3D layer of solid reaction product. The thickness of this reaction layer will be assumed to be negligible compared to the

drop size, so that this layer does not disturb the measurement of the macroscopic contact angle. From literature results it has been concluded that wetting in reactive systems is governed by the final interfacial chemistry at the triple line rather than by the intensity of the reaction.

As given in the above classification two possible cases of wetting the newly formed reaction layer are possible: the reaction product is more (II.1.i.) or less (II.1.ii.) wettable than the substrate. In the present work on wetting promoting thin films, the case of less wettability of the reaction layer is not interesting and therefore omitted. The formation of a reaction layer which promotes the wetting of the alloy is more relevant.

Two possible configurations can be produced at the triple line when the final contact angle is reached: a stable and a metastable configuration (see Figure 7.10).
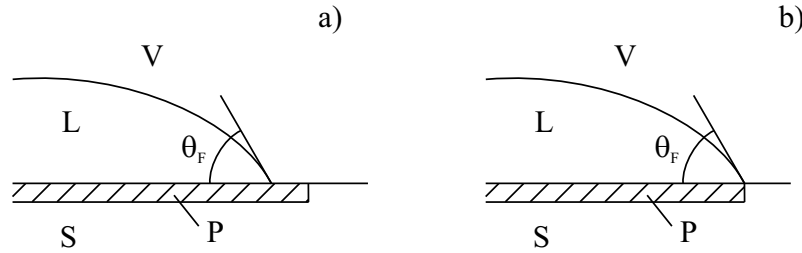

Figure 7.10: Possible configurations of the reacting system at the triple line when the steady-state contact angle is reached. a) stable configuration, b) metastable configuration. The reaction product is marked with P.

The stable configuration has a layer of reaction product P extending on the free surface of the substrate (Figure 7.10.a), while in the metastable configuration the reaction layer does not extend over the edge of the drop (Figure 7.10.b). The metastable configuration is possible if the extension of the reaction layer outside the drop edge is blocked by thermodynamic barriers. A critical layer thickness d_C can be calculated from the Gibbs energy of the reaction per unit volume of P (Figure 7.10) and the change of the interfacial energies [14]. This leads to a critical thickness of about 1 nm. Only for thicknesses less than d_C the metastable configuration is possible. Real reaction layers found in literature are orders of magnitude thicker (μm - range). Except for very unrealistic values of $\Delta\sigma$ and ΔG, thermodynamic barriers

to the lateral growth of P on the substrate exist, therefore the final configuration expected for reactive wetting is the stable one.

For the spreading kinetics of reactive wetting two limiting cases can be defined, by comparing the rate of the chemical reaction at the triple line to the rate of diffusion of reactive solute from the drop bulk to the triple line. In the reactive wetting case it is considered that the liquid metal consists of a solvent A containing a reactive solute B. The reaction product P is better wetted by the A-B alloy than the initial substrate.

This leads to the distinction of reaction and diffusion limited spreading [61, 62].

Diffusion limited spreading

When the local reaction rates are comparatively high, the rate of lateral growth of the reaction product at the triple line is limited by the diffusive supply of reactant from the drop bulk to the triple line. The contact angle decreases during wetting and so the reduction of the reactant in the diffusion field will lead to a continuous decrease in the reaction rate. This results in the decreasing movement of the triple line, see Figure 7.11. Therefore time-dependent spreading rates are expected in this case.
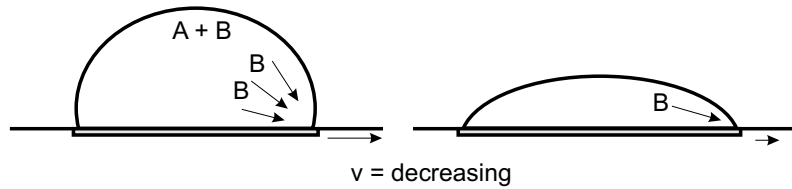

Figure 7.11: Diffusion controlled reactive wetting: The limiting factor is the transport of the reactant from the liquid to the reaction at the triple line. The triple line velocity decreases during the wetting experiment.

In a liquid the solute is transported by convection and diffusion; the governing equation is Fick's second law written in the frame of reference of the moving triple line with the velocity u,

$$D \, \Delta C + u \, \nabla C = \frac{\partial C}{\partial t} \tag{7.1}$$

with C as concentration of reactive species and D as diffusion coefficient in the liquid. By assuming just diffusion near the triple line, the second term on the left hand side which represents convection can be neglected. A solution for Equation 7.1 is presented in [63] and [62], with the result:

$$\frac{dR}{dt} = \frac{2DF_{(t)}}{en_v}\left(C_0 - C_e\right)\theta \tag{7.2}$$

where R is the drop base radius, n_v is the number of moles of reactive solute per unit volume of the reaction product, e is the reaction product thickness at the triple line, C_0 is the bulk drop concentration, C_e is the concentration of reactive solute in equilibrium with the reaction product (such that $C = C_e$ at the triple line) and $F_{(t)}$ is a function of time, which varies only weakly and can be assumed as a constant with a numerical value 0,04.

For a spherical cap shaped droplet with the volume V the contact angle can be approximated by $\theta = 4V/(\pi R^3)$. Inserting this relation into Equation 7.2 yields:

$$R^4 = const. \, V^1 \, t \tag{7.3}$$

Here the exponents of R and V are 4 and 1, respectively. A plot of the radius R over the time t for an arbitrary volume V is given in Figure 7.13. The decrease in the triple line velocity of the diffusion limited wetting regime can be seen, so plotting R vs. t gives evidence of the reactive wetting regime.

Reaction limited spreading

In this limiting case the chemical kinetics at the triple line are rate limiting because diffusion within the droplet is comparatively rapid. In this case the rate of reaction and hence the triple line velocity are constant with time, see Figure 7.12 (if the reaction does not change the global drop composition significantly, so that the chemical environment of the triple line is constant with time).
This means:

$$R^1 = const \, V^0 \, t \tag{7.4}$$

where the exponents of R and V are 1 and zero, respectively. By plotting the droplet radius vs. the time, one gets the straight line in Figure 7.13. The difference in the
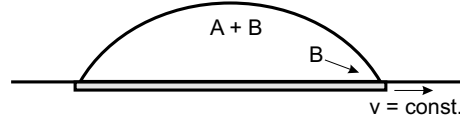
Figure 7.12: Reaction controlled reactive wetting: It is limited by the time for the reaction at the triple line. The triple line velocity is constant during the wetting experiment.

time evolution of the two curves is evident, so the distinction of these two extreme cases - pure reaction limited or pure diffusion limited spreading - should be easy to make.
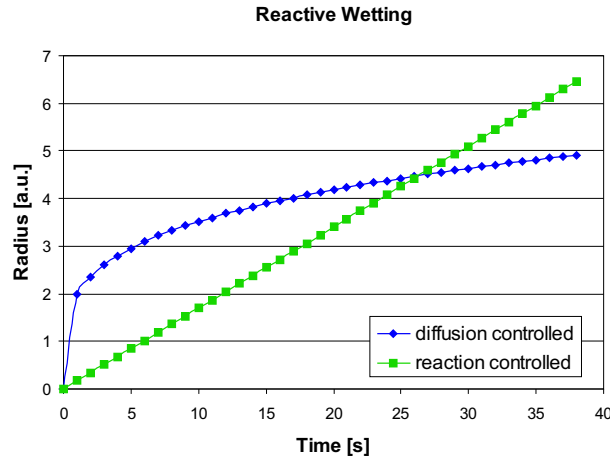

Figure 7.13: Comparison between the two different reactive wetting regimes: diffusion controlled and reaction controlled reactive wetting.

7.3.2 Analysis on different samples

The identification of the type of reactive wetting was done in three different sample systems: CuABA on pure carbon (glassy carbon), on a Ti thin film and on a stoichiometric TiN thin film, both deposited on carbon. The wetting of the substrates with the brazing alloy was recorded until a final contact angle was observed (in all three cases about 10°). The samples just differ in the time for reaching the final contact angle. With the additional interlayers the time was less than half the time for the carbon substrate (see the x-axis in Figure 7.14 - Figure 7.16).
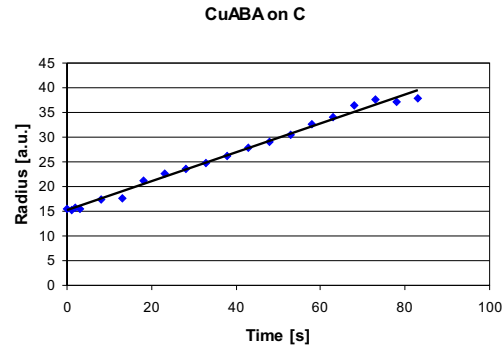
CuABA on C

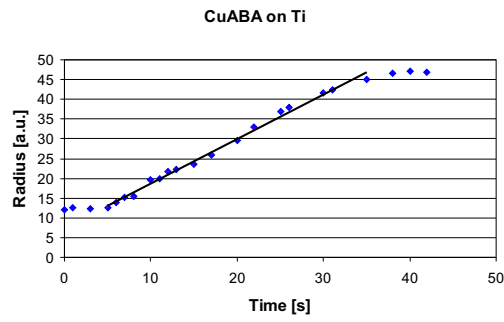*Figure 7.14: Droplet radius vs. time of CuABA on Carbon.*

CuABA on Ti

Figure 7.15: Droplet radius vs. time of CuABA on Ti.
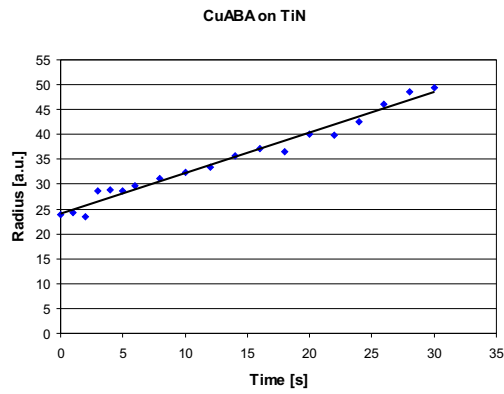
CuABA on TiN

Figure 7.16: Droplet radius vs. time of CuABA on TiN.

In Figure 7.14 the wetting behavior of CuABA on pure carbon, in Figure 7.15 CuABA on a Ti interlayer and in Figure 7.16 CuABA on a TiN interlayer is shown. In these figures the radius of the droplet is plotted vs. the time, and in all three different cases the experimental values (solid dots) can be fitted with a straight line. Based on the considerations in the previous section this leads to the identification of the wetting regime to be reaction limited. The data after reaching the final contact angle (similar to the largest radius) are not drawn in all figures, so in these cases the last data value means the largest radius.

In the above examples of reactive wetting the CuABA brazing alloy reacts with the substrate material (pure or with additional interlayer), forming a reaction layer which promotes the wetting of the liquid drop. The chemical elements found in these reaction layers are mainly Ti, Si, Cu, C and even N (see Table 6.2, Table 7.2 and Figure 7.37). So these elements are involved into the formation of the reaction layers and therefore responsible for the good wetting of the liquid droplet.

The possible phases build from these elements are manifold: SiC, TiC, Ti_2C, Si_3N_4, CuN, $TiCN$ and $SiCN$, several phases of $TiCu$, $TiSi$, and $CuSi$. Some of these phases are known as wetting promoters for Cu e.g. TiC and Si_3N_4, others e.g. SiC is not wetted by pure Cu [14], but for the most of them no data is available. Despite no exact determination of the phases in the reaction layers has been performed, the improvement of the wetting behavior by them is significant.

7.3.3 Cross sectional investigation

During the wetting experiments the wetting alloy spreads over the surface of the substrate and reaches the final contact angle. These experiments are performed at the melting temperatures of the brazing alloy, which is 1024°C in the case of CuABA, so at high temperatures compared to standard soldering. The cooling down after the experiment is just done by turning off the current of the resistance heater and leaving the sample in the water cooled clamps. This results in a cooling rate of approx. 2 K/s (in approx. 10 min room temperature is reached).

The solidified droplets showed two different adhesion behaviors: either the solidified droplet adheres well to the substrate (either on the whole substrate or a small piece which broke out of the substrate) or the solidified droplet detached from the

substrate. This happened with the CuABA brazing alloy on the same substrates or interlayers. These two different cases where investigated by cross sectional preparation of the samples. In Figure 7.17 the cross section of CuABA on a 100 nm TiN film is shown where the droplet adheres to the glassy carbon substrate. In contrast, in Figure 7.18 the droplet detaches from the substrate and just the drop was prepared in cross section.
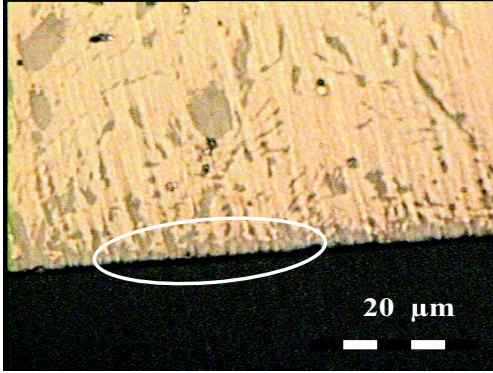

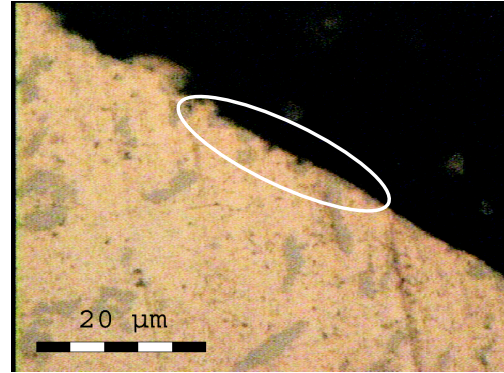Figure 7.17: Cross section of CuABA on TiN with an continuous reaction layer.

Figure 7.18: Cross section of CuABA on TiN with a non continuous reaction layer.

In Figure 7.17 a reaction layer at the interface CuABA/C is clearly visible. On the entire interface this reaction layer is continuous. A different behavior is found in the case of the detached droplet. Here on the interface and also in the bulk drop a darker phase is found, but not as continuous layer (see Figure 7.18). So in a quick assumption the adhesion of the CuABA on the carbon substrate can be attributed to a continuous reaction layer formed at the interface of brazing alloy and substrate, which is in general the goal of reactive brazing alloys. The difference in adhesion of equal samples is not yet clear, but some small heating differences in time or temperature drift during the experiment can be the reason for this.

The mismatch in the Coefficients of Thermal Expansions (CTE) is the reason for stresses in the materials and therefore responsible for the delaminations. The CTE of CuABA is 19,5 $\times 10^{-6}$ K^{-1} (from room temperature to 500°C) and 2,6 $\times 10^{-6}$ K^{-1} for the glassy carbon (Sigradur G) substrate (from room temperature to 200°C). The large mismatch leads to stresses which have to be complied by an interlayer to avoid cracks and delamination in the joint. This is a possible explanation of the above situation: in the sample with the non continuous reaction layer the CuABA is next

to the carbon and so the mismatch is too high for bonding, in the other sample the continuous reaction layer between CuABA and the carbon plays the role as an intermediate layer for stress reduction.

On these cross sections EDX measurements were done to investigate the two different phases visible in the images. The spectrum of the brighter, Cu shining phase is shown in Figure 7.19 and the spectrum of the reaction layer is given in Figure 7.20.
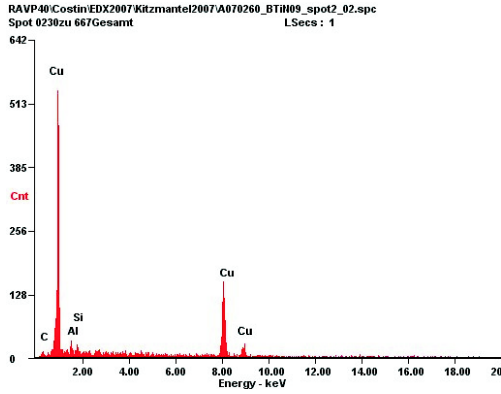

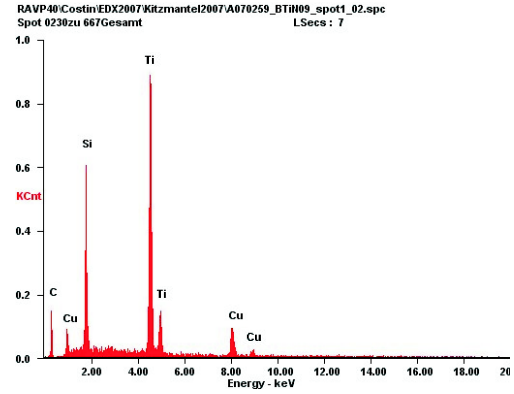Figure 7.19: EDX spectrum of the brighter phase in the CuABA alloy.

Figure 7.20: EDX spectrum of the darker phase/reaction layer in the CuABA alloy.

The concentration of the elements (in at%) of the two phases is given in Table 7.2, showing the high Cu concentration in the brighter phase compared to the high Ti and high Si amount in the reaction layer phase.

	reaction layer	brighter phase
Cu	8,2	52,0
Ti	25,4	-
Si	16,5	3,8
Al	-	4,9

Table 7.2: EDX results on the cross sectional samples: Elements in at% in the reaction layer near the interface and in the brighter phase of the sample.

Due to just one EDX measurement e.g. no standard deviation can be given. Despite the uncertainty of the measurement (few at%) the significant difference between the two phases is visible. In the reaction layer a high concentration of Ti and

Si was detected, showing that this elemental distribution is far from the original CuABA alloy composition. Otherwise the bright phase in the images is mainly composed of Cu with some percent of Si and Al, which is close to the original CuABA composition. A high amount of carbon was detected in both phases, which can be mainly attributed to some contaminations of the surface during handling/transport. Of course the carbon in the reaction layer has also a part in the formation of TiC.

7.4   TiN on Graphite

Brazing trials were done with several different coatings on graphite. In Table 7.3 the four samples used for the brazing experiments are listed with the appropriate parameters (argon and nitrogen flow, thickness, stoichiometry). As substrate material graphite IG-43 (from Toyo Tanso)[1] was used, delivered by ARI Ansaldo Ricerche S.p.A.

Sample	Ar [sccm]	N_2 [sccm]	thickness	x
CTiN01	8,1	1,0	100 nm	1
CTiN03	8,1	0,6	100 nm	0,30
CTiN04	8,1	1,0	1 μm	1
CTiN05	8,1	0,6	1 μm	0,30

Table 7.3: Sample parameter of TiN_x on graphite with x as stoichiometry.

Two different stoichiometries with two different thicknesses of the TiN_x films were used for the brazing experiments. These two coatings were: TiN and $TiN_{0,30}$, which showed the fastest wetting behavior.

An image of the 100 nm thick TiN coating sputter deposited onto the graphite is shown in Figure 7.21.

A sketch of the brazing layout is given in Figure 7.22, where "interlayer" means the different TiN_x coatings from Table 7.3. The brazing was performed under vacuum at a temperature of 1035°C for 18 min to a 2 mm thick Cu sheet.

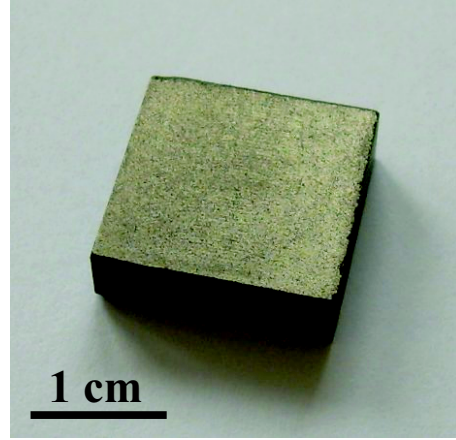[1]Material parameter see Appendix F

Figure 7.21: 100 nm TiN sputter deposited onto graphite IG43.
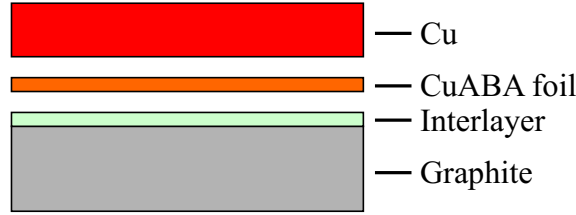

Figure 7.22: Scheme of the brazing layout. Interlayer means the different substoichiometric TiN_x coatings.

The thickness of the CuABA brazing foil was 50 μm. After the brazing of the samples all of them were analyzed by a non-destructive ultrasonic technique. This method allows the detection of cracks and holes in the interface of the joint. In Figure 7.23 the result of this measurement is presented. The different colours correspond to different levels of attenuation of the ultrasonic wave (in decibel - dB): a detached interface would reflect almost all the signal, i.e. zero attenuation. Delaminations in the sample would appear as large reflection like for the reference sample. The reference sample is tested parallel to have a reference for the condition of full reflection. It consists of a copper sheet which is immersed in water and as a consequence the ultrasonic waves which enter the reference sample are reflected almost completely. In well brazed samples the ultrasonic waves which enter the copper sheet are able to pass to the graphite or CFC and they are not reflected.

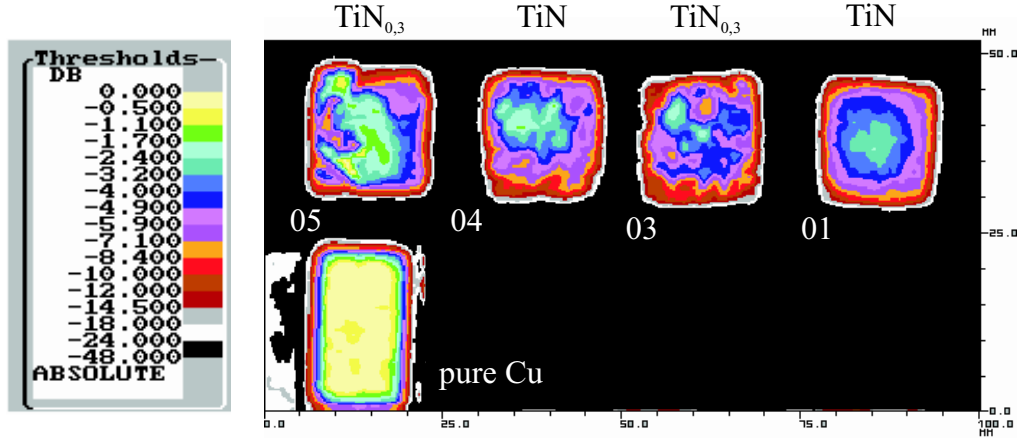In Figure 7.23 one can see the ultrasonic images of the four brazed samples (the

Figure 7.23: Non-destructive ultrasonic testing of the samples after brazing. The number in the image corresponds to the number in the sample name (see Table 7.3).

numbers in the image correspond to the numbers in the sample name) and of a pure Cu reference sample. All of the images show a good joint of the samples and no significant defects were detected. According to this technique the brazing of the samples was successful.

After the non-destructive ultrasonic testing, destructive metallographic examinations of the samples followed. Therefore the samples were cut and the cross-section of the joint was analyzed by optical microscopy and analytical scanning electron microscopy (SEM/EDX). The result of this investigation is presented in the next three figures; in Figure 7.24 an optical image of the brazed joint is shown, in Figure 7.25 a SEM image at higher magnification and in Figure 7.26 a SEM image with the N concentration profile is shown.

The cross sectional analysis was done with all four samples from Table 7.3. In conclusion it can be said, that no differences between the two stoichiometries and the two thicknesses was found with this analysis. So the images are representative for all samples. The optical microscopy image (Figure 7.24) shows a sound joint between the brazing alloy and the graphite. The penetration of the reaction layer into the graphite porosities is very good and in the brazing alloy intermetallic precipitates are present which is usual for the brazing alloy. The SEM image in Figure 7.25 shows the same reaction layer in a higher magnification; also here the sound joint is clearly visible. The reaction layer itself contains a Ti richer zone near the graphite
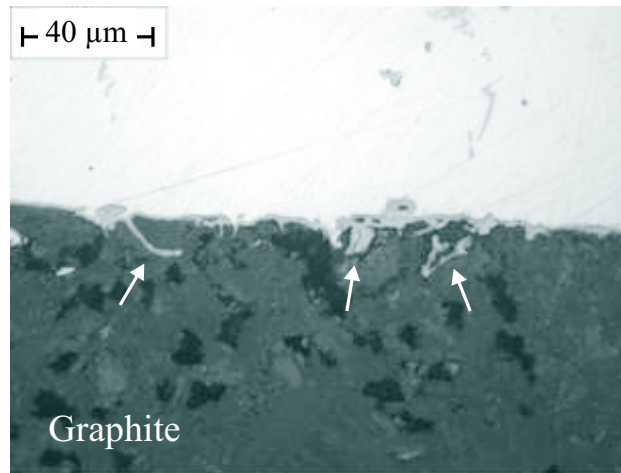
Figure 7.24: Optical microscopy image of the brazed joint. One can see the good penetration of the reaction layer into the graphite porosities, indicated by the arrows.
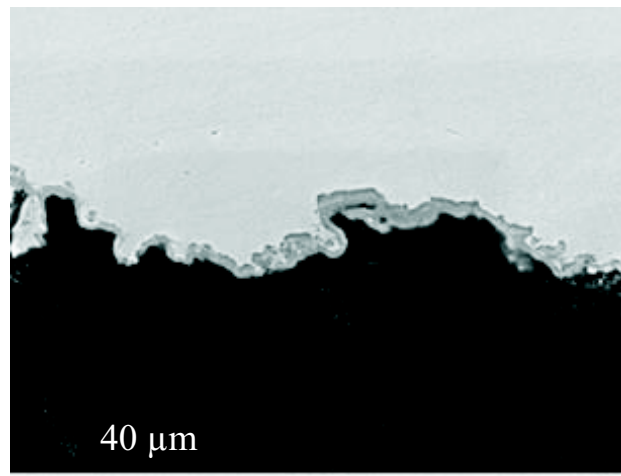

Figure 7.25: SEM image of the brazed joint, a sound connection to the carbon.

and a Si richer zone near the Cu side. EDX maps of the elements C, Si and Ti are shown in Figures 7.27 - 7.30.

The detection of the TiN layer was not possible, the qualitative N concentration profile (see SEM image in Figure 7.26) shows no higher concentration of nitrogen near the graphite side.

Despite the non detectable influence of the different TiN coatings on the brazing behavior and the microstrutural investigations, it can be concluded that the coatings
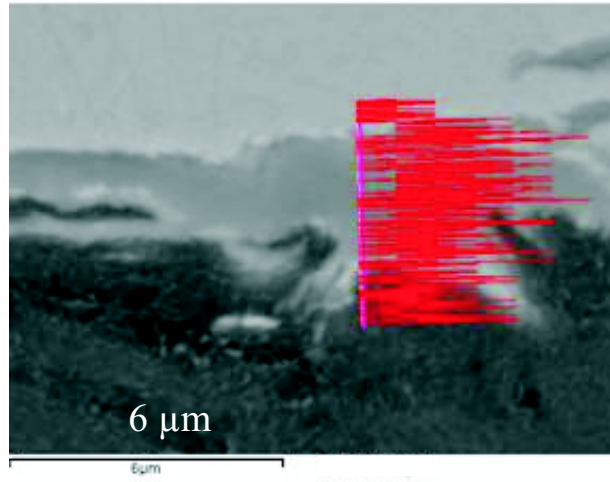
Figure 7.26: SEM image of the brazed joint with a qualitative N concentration profile, no higher concentration on the graphite side can be detected.
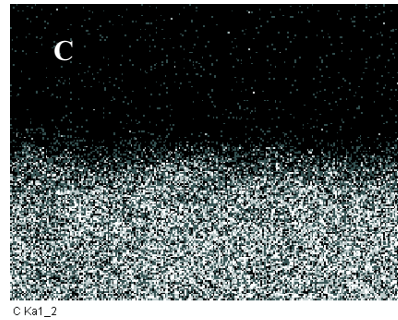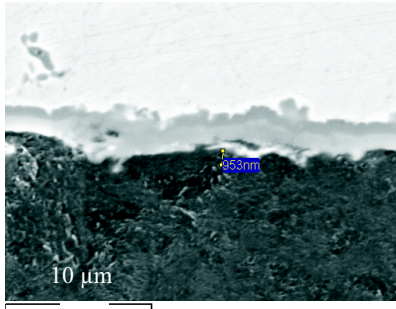

Figure 7.27: SEM image of the brazed joint.

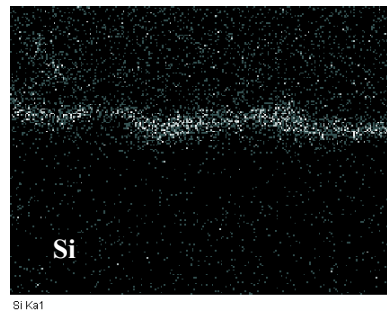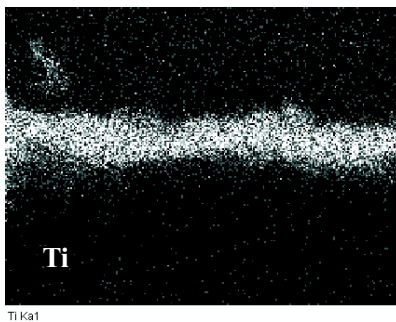*Figure 7.28: C EDX map of the sample.*

Figure 7.29: Ti EDX map of the sample.

Figure 7.30: Si EDX map of the sample.

on graphite did not corrupt the final joint. Therefore these coatings were considered as successful interlayers for the joint.

7.5 TiN on CFC

In the next step the wetting promoting TiN coatings were sputter deposited onto CFC NB31[1], which is the state of the art protective material for the application in the PFC. Therefore again four different TiN interlayers were produced (two thicknesses with two stoichiometries, respectively), the parameters of the samples are given in Table 7.4.

Sample	Ar [sccm]	N$_2$ [sccm]	thickness
CTiN07	8,1	0,6	100 nm
CTiN08	8,1	1,0	100 nm
CTiN09	8,1	0,6	1 μm
CTiN10	8,1	1,0	1 μm

Table 7.4: Sample parameter of TiN on CFC.

An image of such a TiN coating is given in Figure 7.31, where the typical layered structure of the CFC is still visible through the coating.
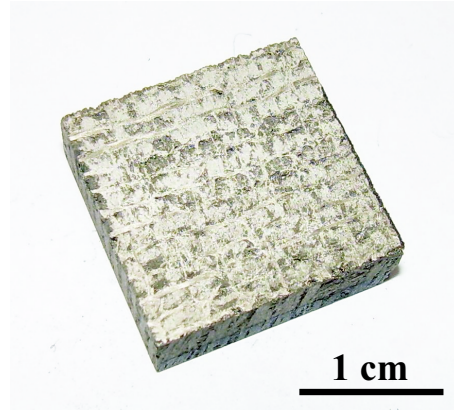

Figure 7.31: 1 μm thick TiN coating on CFC NB31. The layered structure of the CFC is still visible through the coating.

In contrast to TiN on graphite (see Section 7.4), the compounds brazed in this investigation had a different configuration. They were produced in a configuration

---

[1]Material parameters see Appendix F

similar to the final one expected for active cooled PFCs. These consist of an additional 2 mm thick Mo sheet (low CTE interlayer) between the CuCrZr heat sink and the CFC, to reduce the stresses generated by the different expansion coefficients. The schematic configuration is given in Figure 7.32.
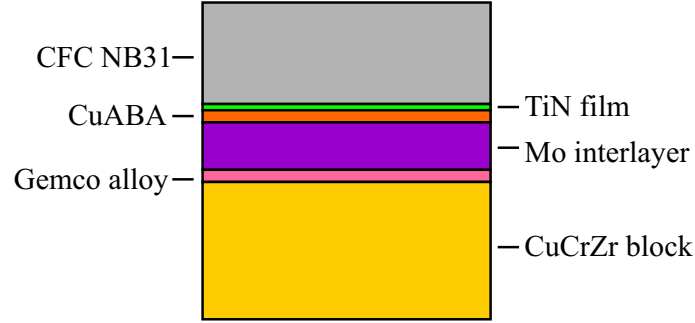

Figure 7.32: Schematic configuration of the brazing layout. The introduction of a Mo interlayer shall lower the stress due to CTE mismatch and it is the expected compound configuration for active cooled PFC.

The brazing was performed in one single vacuum heat treatment at 1035°C for 18 minutes. Then the samples were cut and microstructural investigations were performed.

The achieved results can be considered as promising for all of the produced compounds, but a clear advantage of the 100 nm thin $TiN_{0,3}$ film turned out. It showed a better joint, with less cracks in the CFC and no detachments between CFC and brazing alloy. These cracks just appeared on the edges of the compound, but this will be significantly reduced in the active cooled mock-ups, because of the more accurate alignment of the parts. In the case of the thicker TiN films some delaminations between the brazed joint and the CFC were visible.

Nevertheless it is difficult to state that the cracks within the CFC have been produced by the differences between the TiN films. These cracks seem to be more mechanically caused than due to the chemical interaction of the CuABA with the TiN-coated CFC. On the other hand, the detachments of the CFC from the brazing alloy could be influenced by the thickness of the TiN film. So, the following images and investigations are given for the 100 nm thick $TiN_{0,3}$ coating.

Optical images of the brazed compound are given in Figure 7.33 and in Figure 7.34,

showing the sound joint of the different layers. In these figures no cracks and delaminations are visible.
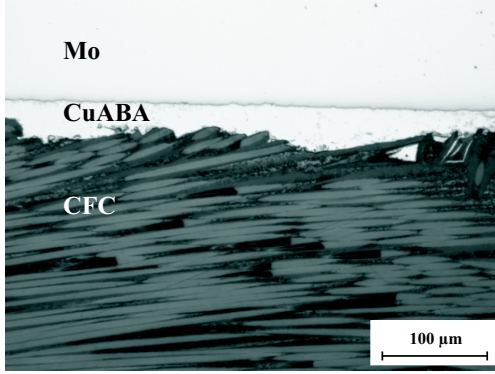

Figure 7.33: Optical microscopy image of the brazed compound. The interface is sound, without delaminations and cracks.
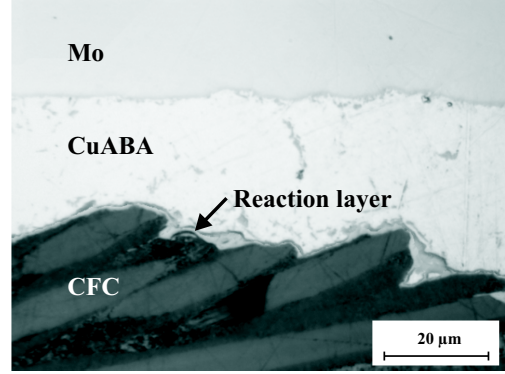

Figure 7.34: Optical microscopy image of the brazed compound. Additional to Figure 7.33 the reaction layer at the CFC side is visible.

This sample was also analyzed by means of EDX mapping. A SEM image of the compound is shown in Figure 7.35 and the elemental maps are given in Figure 7.36, showing the elements C, Cu, Si and Ti.
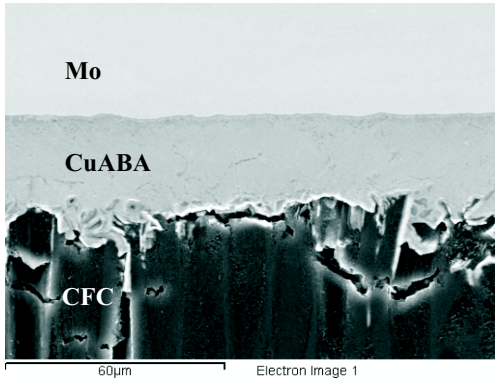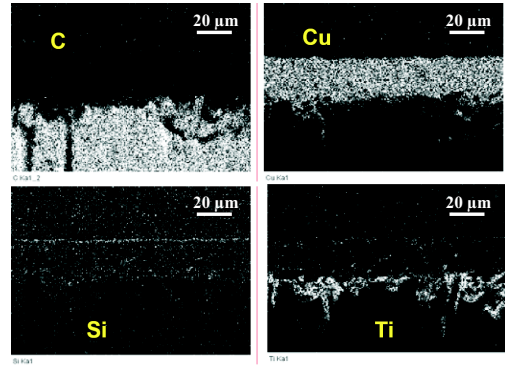

Figure 7.35: SEM image of the brazed compound.

Figure 7.36: Elemental mapping (C, Cu, Si and Ti) of the brazed CFC compound. The joint is Ti richer near the CFC side, whereas a thin Si layer is present near Mo.

The high Cu content in the CuABA foil and the C of the CFC substrate are clearly visible. The amount of Ti is higher at the CFC side, whereas a thin Si rich layer

seems to be present at the Mo side.

The reaction layer at the interface CFC/CuABA was investigated by EDX maps at higher magnification than in Figure 7.36. The thickness of the reaction layer is 1-2 μm and consists of several elements which are shown in the EDX maps of Figure 7.37.
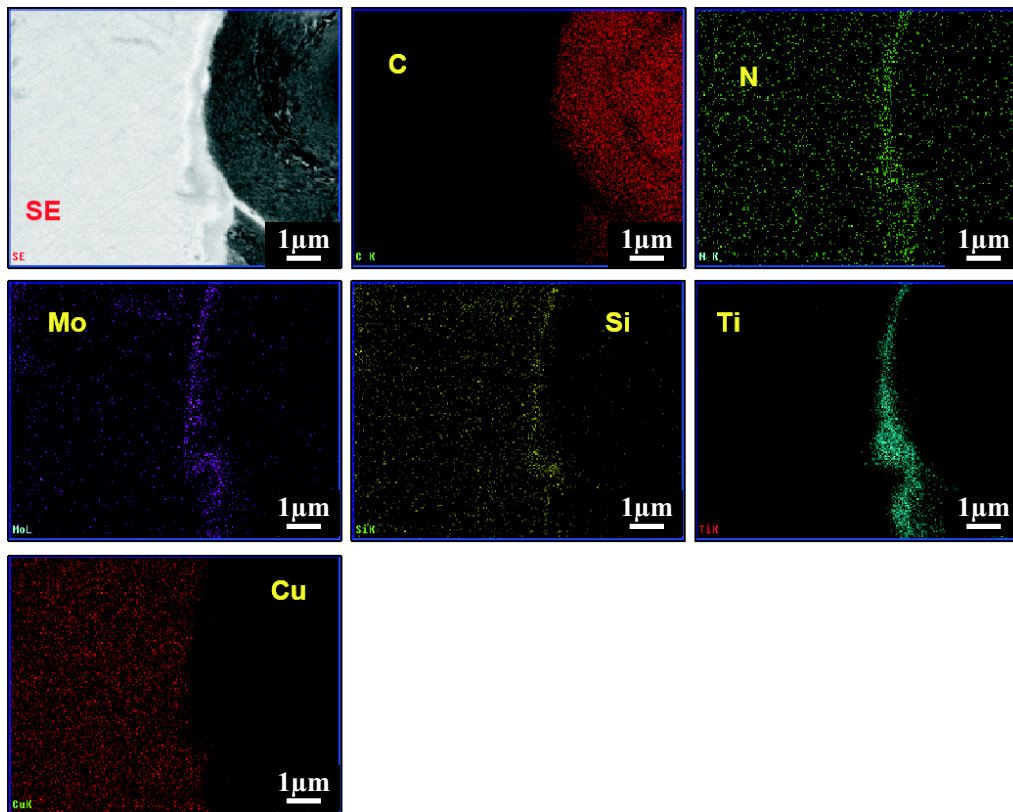
Figure 7.37: EDX mapping of the reaction layer at higher magnification. The maps show the presence of nitrogen and molybdenum in the reaction layer.

Besides the two elements, Si and Ti, which were found also in the EDX investigations of Figure 7.36, additionally the elements Mo and N were detected. The Mo emerges from the 2 mm thick intermediate brazing layer and diffuses through the brazing alloy into the reaction layer at the CFC/CuABA interface. The presence of nitrogen results from the sputter deposited TiN layer onto the CFC. Although the signal is not very strong, it can be clearly detected in the reaction layer.

7.5.1   Thermal shock tests

A very simple but significant test for preliminary screening of flat tile PFCs is the following kind of thermal shock test. Of course this kind of test is not a high heat flux test, it does not produce the temperature gradient on the PFC, which is expected in real operation and it can not be used alone in order to assess the performance of a mock-up. But for the specific geometry, flat tile and C-based protective material, this test has demonstrated its ability to detect unsuccessful joining concepts, avoiding longer and more expensive high heat flux tests.

Experiments have shown that:

- C-based flat tiles brazed to CuCrZr with a pure compliant layer, without any surface tailoring, always failed (complete detachment) before 5 thermal shocks.

- CFC flat tiles brazed to CuCrZr with a pure compliant layer, with surface texture or composite brazing, showed no failure up to at least 20 thermal shocks.

- Uncoated CFC tiles brazed to CuCrZr with a 2 mm thick Mo interlayer showed no failure after 25 thermal cycles.

The thermal shock test can be described as follows:

- A 1,6 mm diameter hole is drilled into the CuCrZr block and a thermocouple is fitted in it.

- Slow heating up to 450 °C within 3 minutes is performed using a hot air blower.

- Very fast cooling down is done by immersion the sample in ambient temperature water.

- Visual inspection is performed after each 5 shocks in order to check for cracks or detachments.

The results of this thermal shock tests are given in Table 7.5.

Here 3 of the 4 compounds survived 30 thermal shock test without failure, just one sample failed at cycle 18. The CFC tile completely detached from the Mo interlayer, but a thin CFC layer has been left on the brazed joint, confirming that the joint

Sample	Cycles to failure
CTiN07	30 (without failure)
CTiN08	30 (without failure)
CTiN09	18
CTiN10	30 (without failure)

Table 7.5: Results of the thermal shock tests on the brazed compounds.

itself was sound. This detachment is not due to defects in the brazed joint, but it is due to CTE mismatch between the materials. The detached sample was larger than the 3 others and therefore the stresses were higher.

The results of the CFC brazing experiments confirm that sputtered TiN coatings are worth to be tested in actively cooled mock-ups. Future high heat flux tests will confirm if the simultaneous use of a low CTE interlayer ($\alpha_{\mathrm{Mo}} = 4,8 \times 10^{-6}\mathrm{K}^{-1}$) and of wetting promoting TiN films deposited onto the CFC is a route for high performance plasma facing components.

Chapter 8

Molybdenum as wetting promoter

8.1 Introduction

The application of molybdenum as interlayer in C/Cu material systems has been reported in literature [64, 65, 66]. It is known as wetting promoter in C/Cu heat sinks, due to the good wettability of Cu on the molybdenum interlayer.

In this work the wetting behavior of heat treated pure molybdenum and molybdenum coatings with Cu and CuABA was investigated. The influence of this thermal treatment on a Mo interlayer was measured by means of Auger Electron Spectroscopy (AES) and Secondary Ion Mass Spectroscopy (SIMS) in order to investigate the diffusion/carbidization process in the Mo layer. A model of the reaction kinetics at the C/Mo interface was designed for comparison with the experiments.

8.2 Wetting experiments

8.2.1 Pure molybdenum

In the first step wetting experiments with copper on pure molybdenum substrates were performed. As Mo substrates, 3 mm thick pieces (10 mm × 15 mm) from a sputter target were used. The contact angle measurements were performed either on a substrate just polished prior the experiment and on a heat treated substrate (at 800°C for 1 min). The results of the wetting experiments are given in Figure 8.1 and Figure 8.2, showing the equilibrium contact angle which is reached after approx.
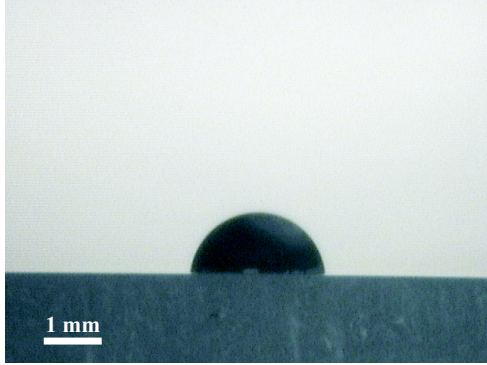
60 seconds.

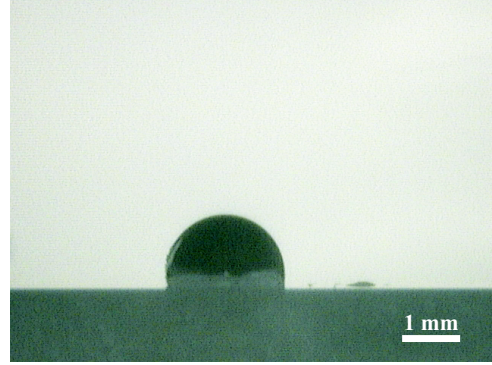*Figure 8.1: Image of the liquid Cu droplet on pure Mo, the contact angle is approx. 84°.*

Figure 8.2: Image of the liquid Cu droplet on pure Mo, previously tempered for 1 min at 800° C. The contact angle is approx. 97°.

The contact angle of Cu on the Mo substrate is approx. 84° and the contact angle on the tempered Mo substrate is approx. 97°. Images of the solidified droplets after the wetting experiments are shown in Figure 8.3 and Figure 8.4, where on the latter one a small movement of the droplet on the Mo substrate is recognizable.
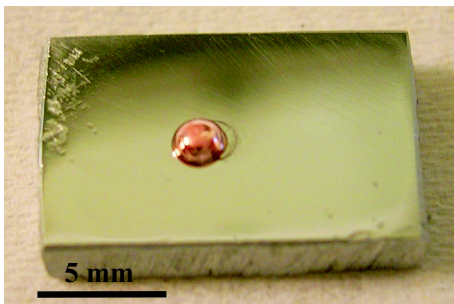

Figure 8.3: Image of the solidified Cu droplet on the Mo substrate.
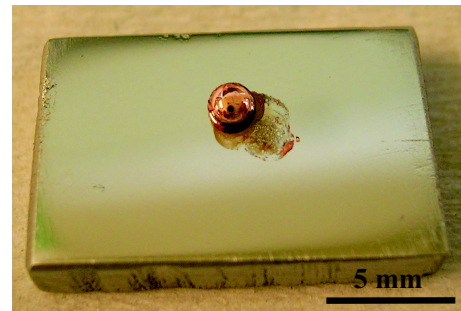
Figure 8.4: Image of the solidified Cu droplet on the Mo substrate, previously tempered for 1 min at 800° C.

Assuming that the liquid-vapor and the solid-liquid interfacial energies are constant in the two different experiments, a change in the contact angle of the liquid drop is affected by the change of the surface energy of the solid substrate. In this simple approach a smaller contact angle means a higher surface energy of the solid, because

of the minimization of the surface energy. Vice versa, a solid substrate with a very low surface energy will exhibit a bigger contact angle with the liquid.

The difference in the contact angle of the two samples is approx. 13°, showing that the difference in the surface energy of the Mo substrate is rather low. This was proved by the measurement of the surface energy of the Mo substrates by the method after *Owens et al*, details see Section 6.1. These investigations gave the value of 56 mJ/m² for the Mo substrate and the value of 46 mJ/m² for the heat treated Mo substrate. A comparison with the contact angles for the two different Mo substrates give the verification of the minimization concept, shown above ($\theta = 84°$ for the Mo substrate and $\theta = 97°$ for the heat treated Mo substrate).

This is in contradiction to the surface energy measurements on 100 nm thick molybdenum coatings on glassy carbon (Mo coating as deposited and Mo coating tempered at 800°C for 1 min). These results are shown in Figure 8.5.
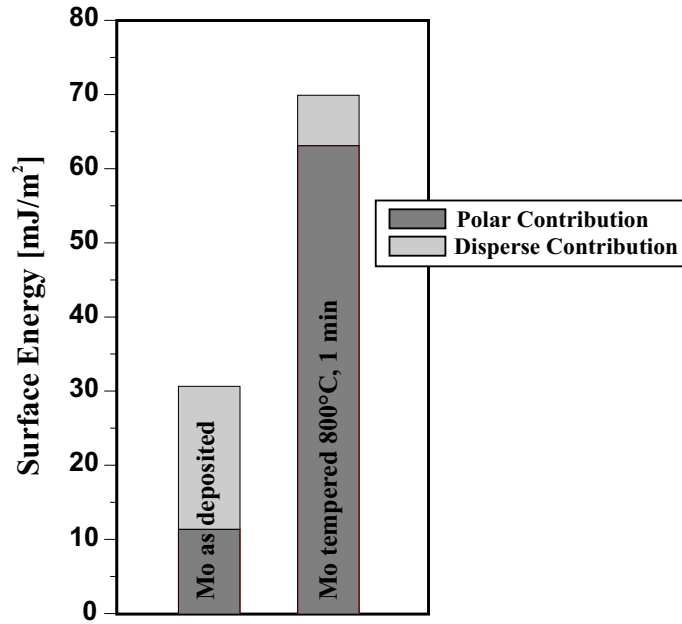
Figure 8.5: Surface energy of Mo coatings on glassy carbon: 100 nm Mo and 100 nm Mo tempered at 800 °C for 1 min

Here a significant increase of the surface energy due to heat treatment is clearly visible. This may be attributed to the formation of molybdenum carbide in the coating, which is discussed in the Sections 8.3 and 8.4. Therefore Figure 8.5 in fact shows the surface energy of a 100 nm Mo coating and the surface energy of a 100

nm Mo₂C coating.

So the heat treatment of a 100 nm thick molybdenum coating leads to an increase of the surface energy of the coating. This is, in turn, responsible for a lower contact angle of a liquid (minimization concept of the surface energy) and therefore for the better wetting of a liquid on this coating. This wetting improvement by thermal treatment is of great interest and is investigated in the next subsections in more detail.

8.2.2 Molybdenum and molybdenum carbide coatings

The wetting experiments were performed on 100 nm thick Mo layers sputter deposited onto Sigradur substrates. Pure Cu and CuABA were used as liquid metals. The contact angle of Cu on Mo and on Mo₂C is reported to be 30° and 18°, respectively [14]. In the previous section the contact angle of Cu on Mo was found to be approx. 84° and the formation of Mo₂C leads to a higher surface energy (means lower contact angle). This experimental value of the contact angle is higher than in literature but the trend, the reduction by the molybdenum carbide, is nevertheless clearly visible.

The parameters for the heat treatment for the carbidization process were 5 min at 1000°C in the HTSDD under high vacuum. In the case of pure Cu both mounting conditions were tried: either the transport of the sample via atmosphere between PVD production and wetting experiment as well as the transport under vacuum in the transfer chamber.

Images of the Cu wetting experiments are given in the following Figures (Figure 8.6 to Figure 8.9). Here the results for Cu on Mo and Mo₂C in vacuum and atmosphere are presented.
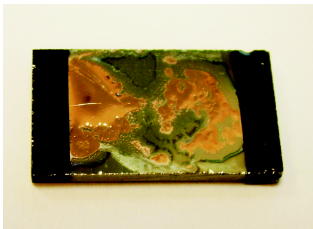

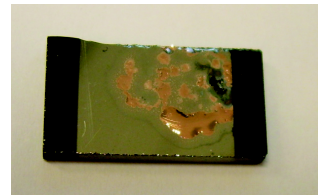*Figure 8.6: Image of Cu on 100 nm Mo (under atmosphere).*

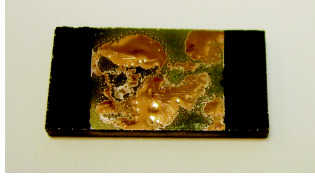*Figure 8.7: Image of Cu on 100 nm Mo₂C (under atmosphere).*

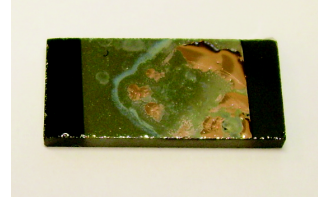Figure 8.8: Image of Cu on 100 nm Mo (under vacuum transport).

Figure 8.9: Image of Cu on 100 nm Mo_2C (under vacuum transport).

All four samples look quite similar, Cu spreads all over the Mo coatings, each of them is wetted well. From these images no differences between Mo and Mo_2C, and transport under vacuum or atmosphere can be deduced. The wetting happens so fast that the molten droplet separates into several regions, all of them with contact angles θ of approx. 15°. Generally it can be said, that all of the above coatings showed a good wetting with pure Cu, but the spreading of the droplet is not uniform. This problem may be solved by the usage of smaller Cu pieces for the experiments. (In all of these experiments Cu cylinders with a diameter of 1,5 mm and a height of 1 mm were used. With the density of Cu (= 8,92 mg/mm^3) this leads to a mass of approx. 16 mg.)

Because of the undetectable influence of the vacuum transport with the transfer chamber on the wetting behavior, in the next experiments with CuABA, this additional transport was not performed.

The following two Figures, Figure 8.10 and Figure 8.11, show the wetting results of CuABA on 100 nm Mo and Mo_2C coatings, respectively.
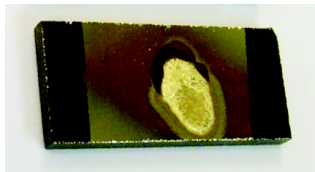
Figure 8.10: Image of CuABA on 100 nm Mo.
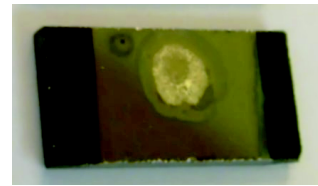

Figure 8.11: Image of CuABA on 100 nm Mo_2C.

The wetting of the CuABA brazing alloy on the two coatings is very similar, both solidified droplets show approx. a circular spreading. The final contact angle θ is in both cases about 10° and the wetting behavior is very fast, meaning that the final contact angle is reached in about one second. This is even faster than for $TiN_{0,3}$.

In some wetting experiments the same phenomenon as observed in the case of TiN coatings happens, i.e. the detachment of the droplet from the Sigradur®G substrate after the experiment during cooling, producing a crater in the glassy carbon. Therefore the weak part of this structure is also the glassy carbon itself.

From two wetting experiments cross sections were prepared and optical microscopy images of them are shown in Figure 8.12 and Figure 8.13, CuABA on Mo and CuABA on Mo_2C, respectively.
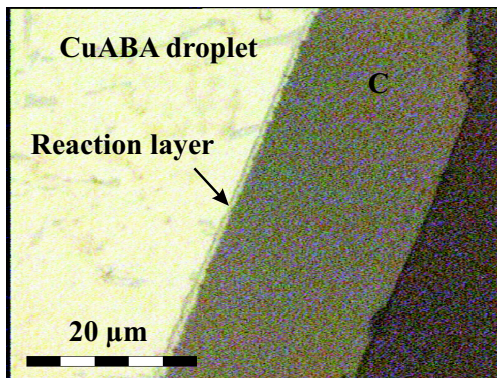

Figure 8.12: Cross section of CuABA on Mo with the reaction layer.
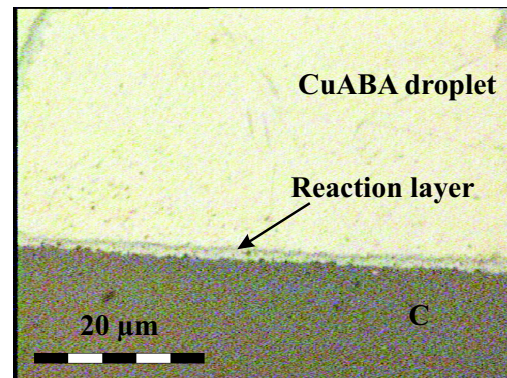
Figure 8.13: Cross section of CuABA on Mo_2C with the reaction layer.

Both figures look very similar, showing the carbon substrate, a reaction layer (of several μm thickness) at the interface and the brazing alloy droplet. The reaction layer is continuous over the whole sample, no cracks and delaminations are visible, the whole structure is sound.

EDX measurements of the reaction layers from Figure 8.12 and Figure 8.13 were performed to investigate the chemical composition of the layers. The result of this investigation is presented in Table 8.1.

In both reaction layers a high amount of Ti and a low amount of Cu was found, also Si was detected in the reaction layers. In the solidified droplets precipitations with a high amount of Ti and Si were detected. The Ti from the CuABA alloy segregates to the reaction layer and the precipitations, whereas the most of the Si segregates to the precipitations.

The thickness of these reaction layers was found to be 2-3 μm, which is in agreement with the images from the optical microscope.

	Reaction layer			
	Mo		Mo_2C	
Element	wt%	at%	wt%	at%
Ti	30,9	13,6	59	35,7
Cu	14	5,5	11,5	5,9
Si	2,1	1,6	9,1	9,4
Al	0,7	0,6	-	-

	Precipitations			
	Mo		Mo_2C	
Element	wt%	at%	wt%	at%
Si	23,5	25,5	32,2	38,1
Ti	59,6	37,9	60,6	42,1
Cu	3,0	1,5	-	-

Table 8.1: EDX investigation of the reaction layer from the samples with the Mo and the Mo_2C interlayers. Additionally the chemical composition of the precipitations in the droplet was measured.

8.3 Analytical investigations

To further investigate carbide formation, thermal treatment experiments were performed with 100 nm thick Mo layers sputter deposited onto glassy carbon substrates. The thermal treatment was performed in the HTSDD with different maximum temperatures. The parameters of the heating procedure are given in Table 8.2.

Sample	treatment time [min]	temperature [°C]
SD13	1	400
SD14	1	600
SD15	1	500

Table 8.2: Temperature parameters for the heat treatment of Mo samples.

These temperatures were chosen after some trials at higher temperatures, for finding the temperature range where the diffusion of C into the Mo layer is clearly observable. With AES depth profiles the composition of the samples was checked. AES is a surface analytical technique with an information depth of a approx. 1 nm. With an additional ion gun (Ar^+ ions) the surface of the sample can be removed and depth information can therefore be obtained.

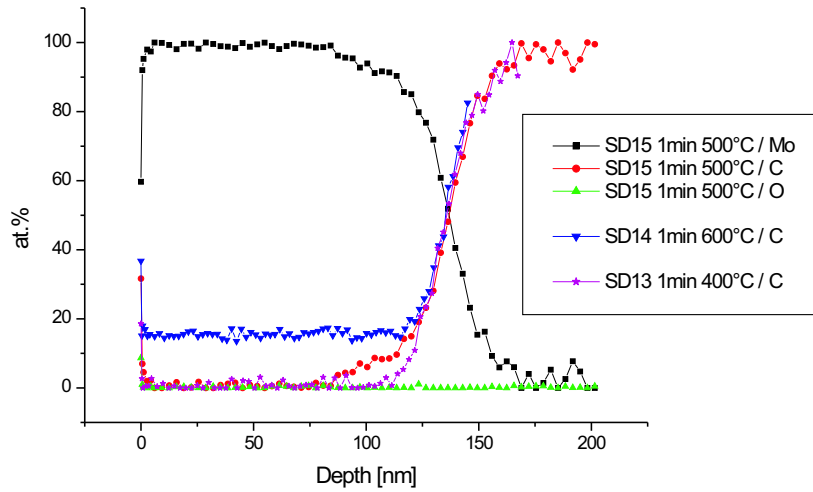The depth profiles of the three different samples from Table 8.2 are presented in Figure 8.14.

Figure 8.14: Auger depth profile of three heat treated Mo coatings (1 minute at 400 °C, 500 °C and 600 °C). The difference in the carbon signal of the samples is visible.

In Figure 8.14 the concentration of C, Mo and O is given for the sample heated at 500°C. For the two other samples only the C signal is plotted for comparison. The sample tempered at 400°C shows no C signal in the Mo layer, contrary to the sample tempered at 600°C, where in the whole Mo layer a constant C signal can be detected. The sample tempered at 500°C represents the intermediate case; here the C signal starts to develop from the C/Mo interface towards the Mo layer. This means that at this time/temperature parameter the diffusion of the C atoms into Mo starts.

For comparison the same samples were investigated by SIMS. The results of these
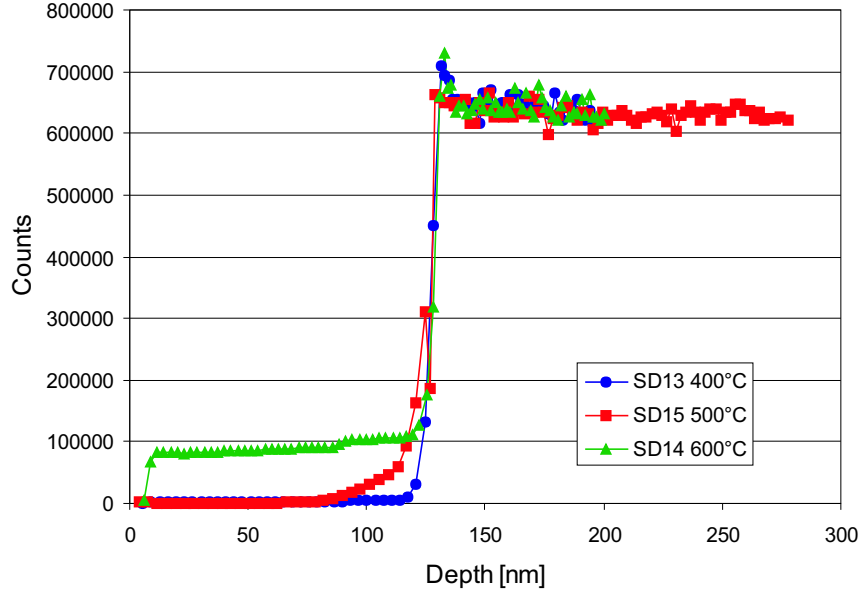
SIMS measurements are given in Figure 8.15.

Figure 8.15: SIMS depth profile of the carbon signal of the three heat treated Mo coatings. The onset of the carbon signal in the 500 °C sample is clearly visible.

These graphs are similar to those of the AES measurement (see Figure 8.14), which is an additional proof of the carbon content in the Mo layer.

The carbon incorporation is either from interdiffusion or from the formation of molybdenum carbide. In literature different temperatures have been found for the formation of Mo_2C. A temperature between 700°C - 900°C is given in [67], depending on the oxygen content. A higher content of oxygen resulted in a higher temperature due to the partial occupation of the interstitial sites by oxygen. In [68] the formation of carbide is not observed after tempering the samples (200 nm Mo on polycrystalline diamond films) 1h at 500°C. At 600°C a 20 nm thick carbide layer was found and complete carbidization of the Mo layer occured at 800°C. In contrast to these high temperatures needed for carbide formation, [69] reports carbide formation at a temperature of 400°C of samples composed of a thin carbon film deposited onto molybdenum. None of these authors mentioned the formation of MoC in their experiments, because its stability at these temperatures is very low.

8.4 Cellular Automaton model

The formation of the carbide layer has been modeled by a Cellular Automaton (CA).
A Cellular Automaton describes a system in time and space by the interaction of
neighboring cells defined by transition functions. The growth of this intermediate
phase occurs by a chemical reaction at the interface and the carbon diffusion through
this phase. Chemical reaction equations and Fick's diffusion equation have been
applied to calculate the concentration of the different species [70].
A simple CA is shown in Figure 8.16, just to give an impression of the geometrical
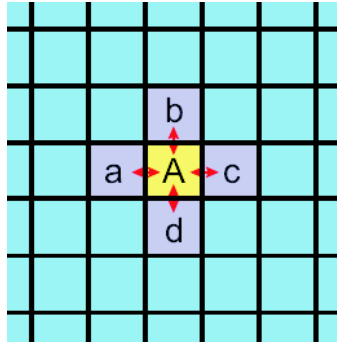situation.

*Figure 8.16: Image of a simple Cellular Automaton. The central cell A interacts with the
neighboring cells via transition rules (arrows).*

Here the central cell "A" interacts with the neighboring cells "a", "b", "c" and "d"
via specified transition rules. The typical cell length is in the order of 1 - 10 nm.
One set of transition rules results from the diffusion equation. Fick's diffusion equa-
tion in one dimension and without any external forces can be written as follows:

$$\frac{\partial c_i}{\partial t} = D \cdot \frac{\partial^2 c_i}{\partial x^2} \tag{8.1}$$

with c_i as concentration of species i $[particles/m^3]$ and D as diffusion coefficient
$[m^2/s]$. D is a constant if the concentration is low.
The diffusion coefficient depends strongly on the temperature and has an Arrhenius-
type behavior:

$$D = D_0 \exp\left(-\frac{E_A}{RT}\right) \tag{8.2}$$

with D_0 as pre-exponential factor $[m^2/s]$, E_A as activation energy $[kJ/mol]$, R as gas constant $[J/mol\,K]$ and T as temperature $[K]$.

Further it is assumed that the carbide layer growth is a diffusion controlled process, suggested by experiments in [68], therefore a high value of the chemical reaction constant which specifies a second transition rule is used for the simulation. The calculation of the carbide formation with the CA is dependent on the diffusion coefficient of C through the Mo_2C layer. By calculating the carbide formation with values for the diffusion coefficient found in literature no carbide layer was obtained at temperatures up to 600°C - the diffusion constant is too low.

Therefore also the additional influence of grain boundary diffusion has to be incorporated into the model.

The size of the Mo grains in the sputter deposited layer has been measured by Atomic Force Microscopy (AFM) - see Figure 8.17 - and Transmission Electron Microscopy (TEM) - see Figure 8.18 -, latter giving also information about the orientation of the grain boundaries, which are perpendicular to the C/Mo interface in the present case. The grain size was approx. 100 nm.
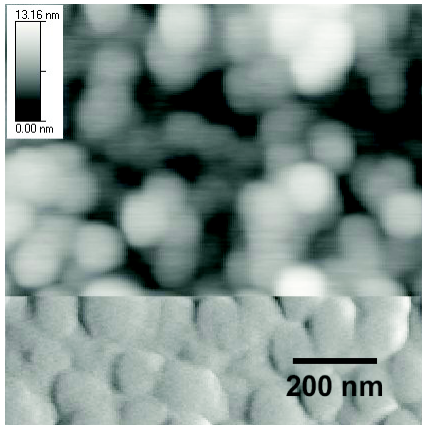

Figure 8.17: AFM micrograph of the surface of a 100 nm thick Mo layer. In the lower part of the image the grain structure is enhanced by artificial shadowing.

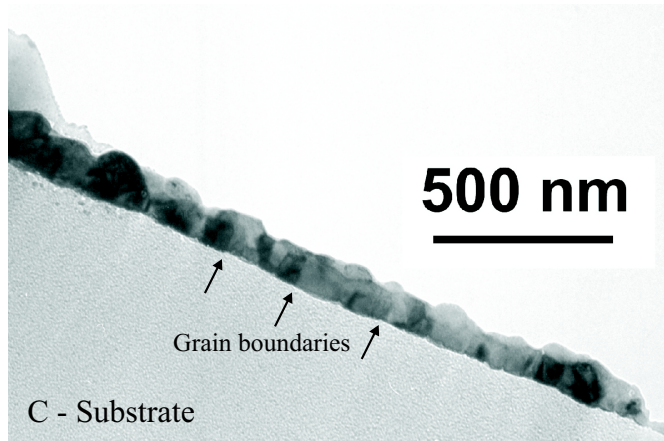*Figure 8.18: Cross sectional TEM micrograph of a 100 nm thick Mo-layer. The grain boundaries (indicated by arrows) are clearly visible. The lateral grain diameter is approx. 100 nm and the grain boundaries are perpendicular to the substrate.*

The diffusion through the grain boundaries is faster than within the grains, increasing the growth rate of the molybdenum carbide in the sample. In order to match the

experimental results, the value for the activation energy in the grain boundary has to be decreased, by keeping the literature value of the bulk diffusion coefficient of C in Mo_2C. In general the diffusion constant within the grain boundaries is 4-8 orders of magnitudes larger than the diffusivity within the grains. Therefore the activation energy of diffusion is reduced by a factor 0,4 - 0,6 while the pre-exponential factor is unchanged.

For the calculation of the carbide formation, the data given in Table 8.3 for the reaction rate constant and the diffusion coefficient were used [70].

chemical reaction equation	$2\ Mo + C \rightarrow Mo_2C$
reaction rate constant k	$10^{10}\ [s^{-1}]$
diffusion of C in Mo_2C	$1{,}1 \cdot 10^{-22}\ m^2/s\ (400°C)$
	$7{,}6 \cdot 10^{-21}\ m^2/s\ (500°C)$
$1{,}876 \cdot 10^{-8} \exp\left[-\frac{183{,}3\ kJ/mol}{RT}\right]$	$2{,}0 \cdot 10^{-19}\ m^2/s\ (600°C)$
diffusion of C in the grain boundary	$7{,}7 \cdot 10^{-18}\ m^2/s\ (400°C)$
	$1{,}3 \cdot 10^{-16}\ m^2/s\ (500°C)$
$1{,}876 \cdot 10^{-8} \exp\left[-\frac{121{,}0\ kJ/mol}{RT}\right]$	$1{,}1 \cdot 10^{-15}\ m^2/s\ (600°C)$

Table 8.3: Parameters for the calculation of the growth of molybdenum carbide [70].

The activation energy E_A of 183,3 kJ/mol is equal to a value of 1,9 eV.

With these assumptions the growth of the molybdenum carbide layer was calculated with the CA and the results are shown in Figure 8.19.

In this figure the concentration of the molybdenum carbide is computed by the CA after a heat treatment for 1 min at temperatures of 400°C, 500°C and 600°C. An onset of the carbide formation can be seen at 500°C, which is in good agreement with the experimental results obtained by AES (see Figure 8.14) and SIMS (see Figure 8.15).

With this comparison between experiment and CA simulation the influence of grain boundary diffusion in the growth of molybdenum carbide is highlighted.

The present chapter dealt with Mo coatings as wetting promoters for CuABA on the
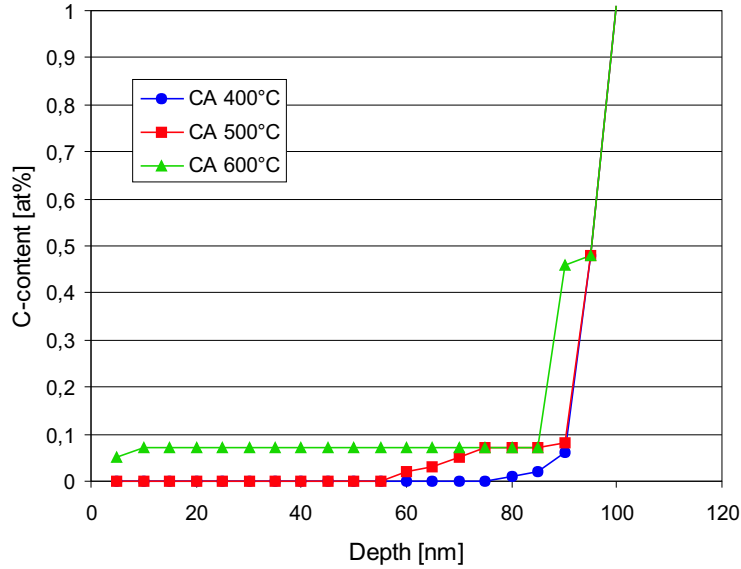
Figure 8.19: Results of the simulation with the cellular automaton, the onset of the carbide formation at the Mo/C interface is visible. The carbon concentration is normalized to the value within the C substrate. The substrate should be assumed at a depth of 100 nm.

carbon substrate. The wetting regime of the brazing alloy droplet is reactive wetting, resulting in the formation of a reaction layer at the interface substrate/droplet. The thermal treatment of the Mo coating during the brazing process leads to the formation of a Mo_2C coating, actually, which was proven by the analytical investigations methods AES and SIMS. The reactive wetting regime could not be identified, due to the very fast wetting of the droplet on the coatings. The increase of the surface energy of the molybdenum coating with the heat treatment was also shown in this chapter, in contrast to pure Mo substrates where the surface energy (and contact angle) is nearly unchanged by heating.

Chapter 9

Conclusion and Outlook

The aim of this thesis was to plan and construct a high temperature sessile drop device for wettability studies in different liquid/solid systems. For the study of the wettability of a molten metal on a solid surface the contact angle between these two phases is relevant. In the present work the sessile drop technique was chosen; this means the optical imaging of the liquid drop which rests on a solid surface and the calculation/measurement of the contact angle between the droplet and the surface. This method can easily be performed for liquids at atmospheric conditions but it is challenging for liquid metals (vacuum conditions and high melting points).

The work was performed in the framework of the EU EXTREMAT IP project (NMP-CT-2004-500253), which deals with the development of new materials for extreme environments. The position of this thesis within the framework of the project is within the task of identifying and characterizing wetting promoters in fusion applications. New interlayers for the existing plasma facing components should be developed. The main interest in this field was the investigation of TiN_x films as wetting promoters in the joining process of Carbon parts to a CuCrZr alloy.

The device constructed within this work is operated in a vacuum chamber under high vacuum, with a base pressure of about 5×10^{-5} Pa and maximum temperatures of about 1100°C. The heating of the samples is realized by a resistance heated substrate holder, which can also be mounted via an ISO KF 40 flange to a PVD chamber where a deposition of thin films can be performed prior to the wetting

experiments. This equipment, which allows the vacuum transport from the PVD chamber to the wetting experiment, is unique to the author´s knowledge. The device was successfully finalized and both, basic experiments to check the feasibility of the equipment as well as systematic wetting experiments concerning the above tasks within EXTREMAT were performed.

Concerning the determination of basic properties of metal melts, the applications of the high temperature sessile drop device are manifold: measurement of the liquid drop geometry and determination of the contact angle, measurement of the liquid surface energy of molten metals and identification of the reactive wetting regime by the time evolution of the contact angle.

For the measurement of the liquid surface energy two models for the sessile drop method are proposed in literature [24, 26]. Both of them involve the measurement of specific geometrical dimensions of bigger metal drops, flattened by gravity. The present investigations have shown the model of Koshevnik [26, 27] to be more precise. The calculated liquid surface energies are well matching the values given in literature [14]. Therefore a fast and reliable way to measure the liquid surface energy of metals could be established.

To investigate the properties of wetting promoting thin films, a PVD chamber was adjusted for sputtering substoichiometric TiN_x. With these films of variable composition, wettability tests were performed. For the first stage of investigation plane carbon substrates were used as substrate material and the state of the art brazing alloy for PFC - CuABA - was used as metal to melt. This study showed a significant influence of the nitrogen content on the wetting time of the substrate (best results were obtained with a nitrogen content of x = 0,30). From the above measurements it was also possible to identify the type of the reactive wetting regime by plotting the droplet radius vs. the time during the wetting experiment. Reaction controlled reactive wetting was observed in all cases of CuABA on C and different TiN_x based coatings.

Finally, the interlayers with the optimised nitrogen content were sputter deposited onto graphite substrates and CFC substrates, supplied by a project partner (ARI

Ansaldo Ricerche S.p.A.). The CFC is the plasma facing material used in the divertor region of the fusion reactor, ITER. Brazing to a pure copper sheet was performed under realistic conditions. The microstructural investigation on graphite showed no significant improvements by introduction of the interlayers. On the other hand, microstructural investigations and thermal shock tests of the compounds with CFC showed excellent over-all properties for all samples, however, the 100 nm substoichiometric $TiN_{0,3}$ coating showed a significantly improved joint.

Based on these results the decision has been made to use substoichiometric TiN coatings in a mock-up which will be exposed to a high heat flux test, simulating the plasma conditions in the fusion reactor. After this test the decision on using substoichiometric TiN films as improved wetting promoters in PFC will be made.

The above work concerning wetting promoting TiN films also resulted in a concept for the industrialization and up-scaling of the deposition process within the framework of ExtreMat (MIC - Material Industrialization Concept). The foreseen demand of wetting promoting coatings for the ITER design is about 100 m^2 in the year 2015. The individual parts have to be removed from time to time, so a continuous demand of coatings is guaranteed. Beside the concepts for TiN also two other wetting promoting thin films are investigated: TiC by the Max-Planck-Institute for Plasma Physics - IPP in Garching (Germany) and Si_3N_4 by Archer Technicoat Ltd. - ATL in London (England). All of them are very interesting and promising for the future concepts of the divertor design in fusion power plants.

A second main part of this thesis is constituted by the investigation of the wetting of Cu and CuABA on molybdenum coatings. It was found that wetting is significantly influenced by the carbide formation induced by heat treatment of thin molybdenum films deposited on carbon substrates. The carbide formation in the coating in dependence on temperature and treatment time was experimentally analyzed by means of AES and SIMS, and compared to the results of a Cellular Automaton model. With this model the influence of grain boundary diffusion on the growth of the molybdenum carbide layer was verified. The wetting of the Mo coatings by the brazing alloy happened within one second and resulted in a contact angle of approx.

10° - meaning excellent wettability.

Finally the high temperature sessile drop device is also suitable for other applications related to the wetting properties of different materials. These range from the simple usage of the high temperature sessile drop device as oven for thermal treatments via the investigation of selective wetting on patterned wetting promoting thin films to monitoring the infiltration behavior of liquid metals in fiber-preforms.

There is, however still room for improvement of the device: a main point is the temperature and temperature uniformity of the heating system with the resistance heater. As heat is introduced from beneath the sample, the temperature uniformity is still questionable.

As a final resume it can be said that it was possible to achieve excellent measurement results with the present high temperature sessile drop device both, in basic research as well as in experimental studies intimately related to applications in the field of future fusion materials. As the production of energy with fusion technology is one way to ensure the future demand of energy for mankind this thesis constitutes a very small, but nevertheless an important part of this way.

Bibliography

[1] Lide D. R. *CRC Handbook of Chemistry and Physics, 74th Edition, 1993-1994*. CRC Press, Inc., 2000 Corporate Blvd., N.W., Boca Raton, Florida 33431, 1993. ISBN 0-8493-0595-0.

[2] WebElements^{TM}, the periodic table on the WWW, Copyright 1993-2007 Mark Winter, The University of Sheffield and WebElements Ltd, UK. www.webelements.com, visited on 27. 11. 2007.

[3] Koráb J., Korb G., Štefánik P., and Degischer H. P. *Composites: Part A*, 30:1023–1026, 1999.

[4] Mayerhofer K. E., Neubauer E., Eisenmenger-Sittner C., and Hutter H. *Applied Surface Science*, 179:275–280, 2001.

[5] Dellanay F., Froyen L., and Deruyttere A. *Journal of Materials Science*, 22:1–16, 1987.

[6] Dhingra A. K. *Trans. R. Soc.*, A294:151, 1980.

[7] Clyne T. W., Bader M. G., Cappleman G. R., and Hubert P. A. *J. Mater. Sci.*, 20:85–96, 1985.

[8] Contreras A., Lopez V. H., and Bedolla E. *Scripta Materialia*, 51:249–253, 2004.

[9] Chen J., Hao C., and Zhang J. *Materials Letters*, 60:2489–2492, 2006.

[10] Yue T. M. and Chadwick G. A. *Journal of Materials Processing Technology*, 58:302–307, 1996.

[11] *ITER EDA Agreement and Protocol 1, ITER EDA Documentation Series No. 1.* IAEA, 1992. Vienna.

[12] Information about ITER and PFC were taken from internal project reports. Information about the ExtreMat project can be found on the project homepage. www.extremat.org, visited on 27. 11. 2007.

[13] Young T. *Phil. Trans. Royal Soc.*, 95:65, 1805.

[14] Eustathopoulos N., Nicholas M. G., and Drevet B. *Wettability at High Temperature.* Pergamon materials serie, Elsevier Science Ltd., 1999. ISBN 0-08-042146-6.

[15] Dupré A. *Théorie Mécanique de la Chaleur, Chapter IX, Actions moléculaires (suite).* Gauthier-Villars, Paris.

[16] Soper A., Gilles B., and Eustathopoulos N. *Materials Science Forum, Transtec Publications*, 207-209:433, Switzerland.

[17] Wenzel R. N. *Industrial and enginieering Chemistry*, 28 (8):988–994, 1936.

[18] Cassie A. B. D. and Baxter S. *Trans. Faraday Soc.*, 40:546, 1944.

[19] Kurogi K., Yanc H., and Tsujii K. *Colloids and Surfaces A: Physicochem. Eng. Aspects*, 2008.

[20] Nakajima A. *Journal of the Ceramic Society of Japan*, 112 (10):533–540, 2004.

[21] Garandet J. P., Drevet B., and Eustathopoulos N. *Scripta Materialia*, 38(9):1391–1397, 1998.

[22] Laplace (Marquis) P. S. *Traité de Mécanique Céleste, fourth volume, first edition (théorie de láction capillaire) of the supplement to Book 10 (sur divers points relatifs au systéme de monde).* Chez Courier. Paris.

[23] Bashforth F. and Adams J. C. An attempt to test theory of capillary action. *Cambridge University Press*, 1883.

[24] Dorsey N. E. *J. Washington Aca. Sci.*, 18:505, 1928.

[25] Bonfield W. *J. Mater. Sci.*, 7:148, 1972.

[26] Koshevnik A. Y., Kusakow M. M., and Lubman N. M. *J. Phys. Chem. (Russian)*, 27:1887, 1953.

[27] Ahmed U. M. and Murr L. E. *Journal of Materials Science*, 11:224–230, 1976.

[28] Zhong D., Mateeva E., Dahan I., Moore J. J., Mustoe G. G. W., Ohno T., Disam J., and Thiel S. *Surface and Coatings Technology*, 133-134:8–14, 2000.

[29] Zhu J., Kamiya A., Yamada T., Shi W., Naganuma K., and Mukai K. *Materials Science and Technology*, A327:117–127, 2002.

[30] Ho H.-N. and Wu S.-T. *Materials Science and Engineering*, A248:120–124, 1998.

[31] Shen P., Tujii H., Matsumoto T., and Nogi. K. *Scripta Materialia*, 48:779–784, 2003.

[32] Yin L., Meschter S. J., and Singler T. J. *Acta Materialia*, 52:2873–2888, 2004.

[33] Levi G., Bamberger M., and Kaplan W. D. *Acta Materialia*, 47(14):3927–3934, 1999.

[34] Stockner M. Master Thesis, Vienna University of Technology, 2004.

[35] Data sheet on www.corning.com, Corning Incorporated Lightning & Materials, Houghton Park CB-08, Corning, New York, 14831. www.corning.com, visited on 17. 08. 2007.

[36] Frey H. and Kienel G. *Dünnschichttechnologie*. VDI-Verlag GmbH, Düsseldorf, 1987. ISBN 3-18-400670-0.

[37] *Vakuum in Forschung und Praxis 18 (2006) Nr. 2, 42-43*. WILEY-VCH Verlag GmbH & Co KG, Weinheim, 2006.

[38] Bergauer A. and Eisenmenger-Sittner C. *Technologie Dünner Schichten, Physik Dünner Schichten*. Vienna University of Technology, 2006. Lecture script.

[39] Xiao P. and Derby B. *Acta mater.*, 44(1):307–314, 1996.

[40] Rocha L. A., Ariza E., Ferreira J., Vaz F., Ribeiro E., Rebouta L., Alves E., Ramos A. R., Goudeau Ph., and Riviere J. P. *Surface and Coatings Technology*, 180-181:158–163, 2004.

[41] Groudeva-Zotova S., Kaltofen U. R., and Sebald T. *Surface and Coatings Technology*, 127:144–154, 2000.

[42] Meng W. J. and Eesley G. L. *Thin Solid Films*, 71:108–116, 1995.

[43] Meng L.-J. and dos Santos M. P. *Surface and Coatings Technology*, 90:64–70, 1997.

[44] Schell N., Bøttiger J., Matz W., and Chevallier J. *Nuclear Instruments adn Methods in Physics Research*, B199:133–138, 2003.

[45] Contreras O., Duarte-Moller A., Hirat G. A., and Avalos-Borja M. *Journal of Electron Spectroscopy and Related Phenomena*, 105:129–133, 1999.

[46] Combadiere L. and Machet J. *Surface and Coatings Technology*, 88:17–27, 1996.

[47] Combadiere L. and Machet J. *Surface and Coatings Technology*, 88:28–37, 1996.

[48] Mayrhofer P. H., Kunc F., Musil J., and Mitterer C. *Thin Solid Films*, 415:151–159, 2002.

[49] Fang Q. and Zhang J.-Y. *International Journal of Inorganic Materials*, 3:1193–1196, 2001.

[50] Berg S., Blom H.-O., Larsson T., and Nender C. *J. Vac. Sci. Technology A*, 5(2):202–207, 1987.

[51] Berg S., Larson T., and Blom H.-O. *J. Vac. Sci. Technology A*, 4(3):594–597, 1986.

[52] Zaidi H., Robert F., and Paulmier D. *Thin Solid Films*, 264:46–51, 1995.

[53] Ostrovskaya L., Perevertailo V., Ralchenko V., Dementjev A., and Loginova O. *Diamond and Related Materials*, 11:845–850, 2002.

[54] Schrank C. Master Thesis, Vienna University of Technology, 2004.

[55] Owens D. K. and Wendt R. C. *Journal of applied polymer science*, 13:1741, 1969.

[56] Riess K. PhD thesis, Martin Luther University, Halle Wittenstein, 2001.

[57] HTW Hochtemperatur-Werkstoff GmbH, Gemeindewald 41, 86672 Thierhaupten, Germany. www.htw-germany.com, visited on 29. 08. 2007.

[58] Rousseaux F. and Tchoubar D. *Carbon*, 15:55–61, 1977.

[59] Rousseaux F. and Tchoubar D. *Carbon*, 15:63–68, 1977.

[60] Schwarz B. Master Thesis, Vienna University of Technology, 2003.

[61] Yost F. G. *Scripta mater.*, 42:801–806, 2000.

[62] Voitovitch R., Mortensen A., Hodaj F., and Eustathopoulos N. *Acta mater.*, 47(4):1117–1128, 1999.

[63] Mortenson A., Drevet B., and Eustathopoulos N. *Scripta Materialia*, 36(3):645–651, 1997.

[64] Neubauer Erich. *Interface Optimisation in Copper Carbon Metal Matrix Composites*. PhD thesis, Technische Universität Wien, 2003.

[65] Eisenmenger-Sittner C., Schrank C., Neubauer E., Eiper E., and Keckes J. *Applied Surface Science*, 252:5343–5346, 2006.

[66] Eisenmenger-Sittner C., Neubauer E., Schrank C., Brenner J., and Tomastik C. *Surface and Coatings Technology*, 180-181:413–420, 2004.

[67] Leroy W. P., Detavernier C., Van-Meirhaeghe R. L., Kellock A. J., and Lavoie C. *Journal of Applied Physics.*, 99(6):63704–1–5, 2006.

[68] Mikhailow S. N., Ariosa D., Weber J., Baer Y., Hanni W., Tang X. M., and Alers P. *Diamond and Related Materials*, 4(9):1137–41, 1995.

[69] Reinke P. and Oelhafen P. *Surface Science*, 468:203–215, 2000.

[70] Kiniger M. Master Thesis, Vienna University of Technology, 2007.

[71] Rauch N. *High temperature spreading kinetics of metals.* PhD thesis, Max Planck Institut für Metallforschung, Stuttgart, 2005.

[72] Honig R. E. and Kramer D. A. *RCA Rev.*, 30:285–305, 1969.

[73] Wesgo Ceramics GmbH, Willi-Grasser-Strasse 11, D-91056 Erlangen, Germany. www.wesgometals.com, visited on 20. 11. 2007.

[74] Federici G., Loarte A., and Strohmayer G. *Plasma Phys. Control. Fusion*, 45:1523–1547, 2003.

[75] Data sheet on www.gtd-graphit.de, GTD Graphit Technologie GmbH, Raiffeisenstrasse 8-10, D-35428 Langgöns, A Toyo Tanso Group Company. www.gtd-graphit.de, visited on 19.10. 2007.

List of Figures

List of Tables

Appendix A

Technical Drawings

The technical drawings for the HTSDD were done with the CAD-software AutoCAD®
2005. An overview of the inner parts of the HTSDD is given in Fig. A.1. Here the
ground flange of the device is shown with the water and current entry supply from
the lower side and the substrate holder with the catching system inside the chamber.
In the Figs. A.2, A.3 and A.4 the heatable substrate holder, the overview of the
manipulator and the water cooling are shown, respectively. All other necessary
technical drawings for the HTSDD (other flanges, single part drawings, adjustable
optic, . . .) are available as AutoCAD®-files but not printed in this thesis.

Figure A.1: Technical drawing of the whole assembly.
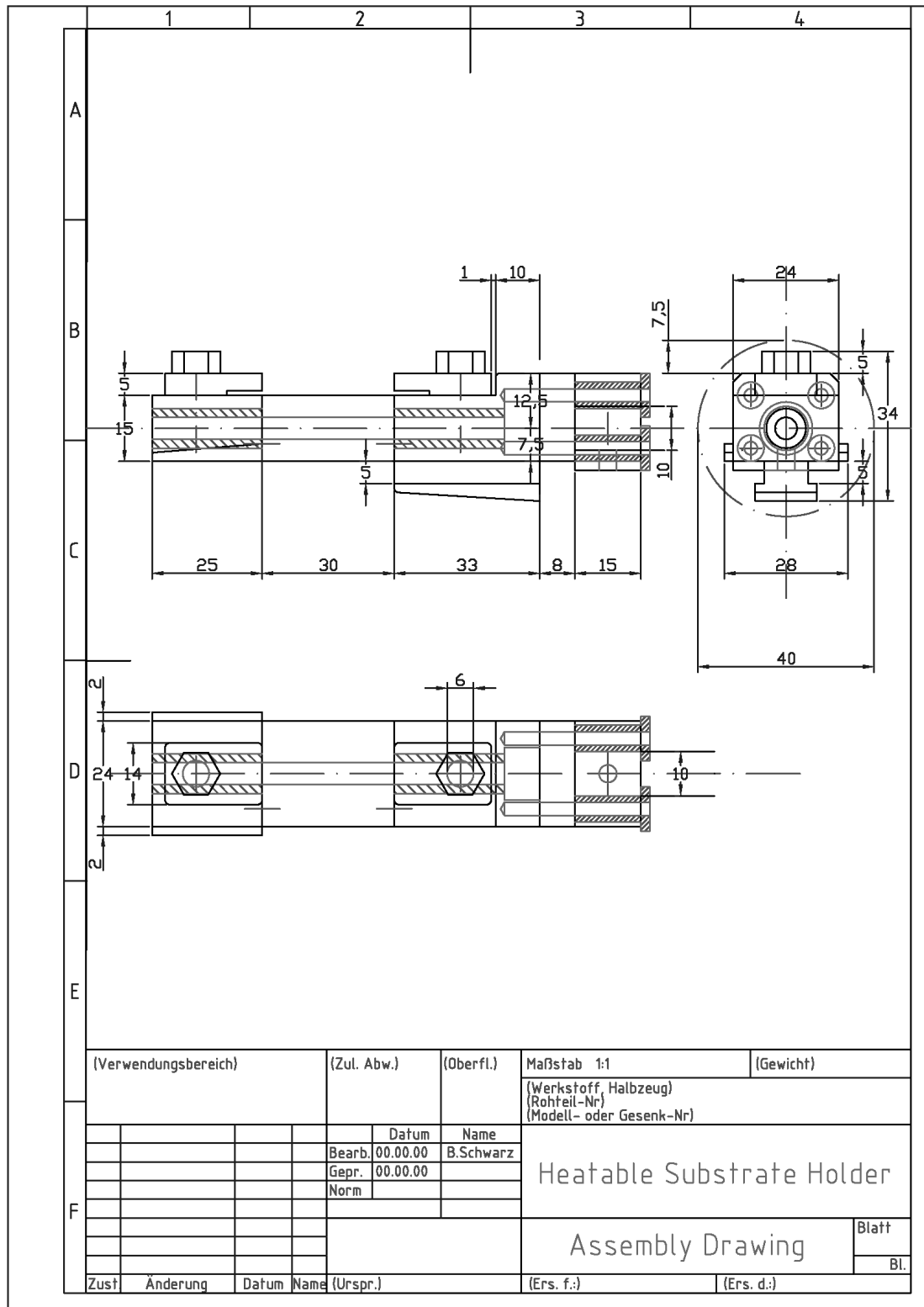
Figure A.2: Technical drawing of the substrate holder.
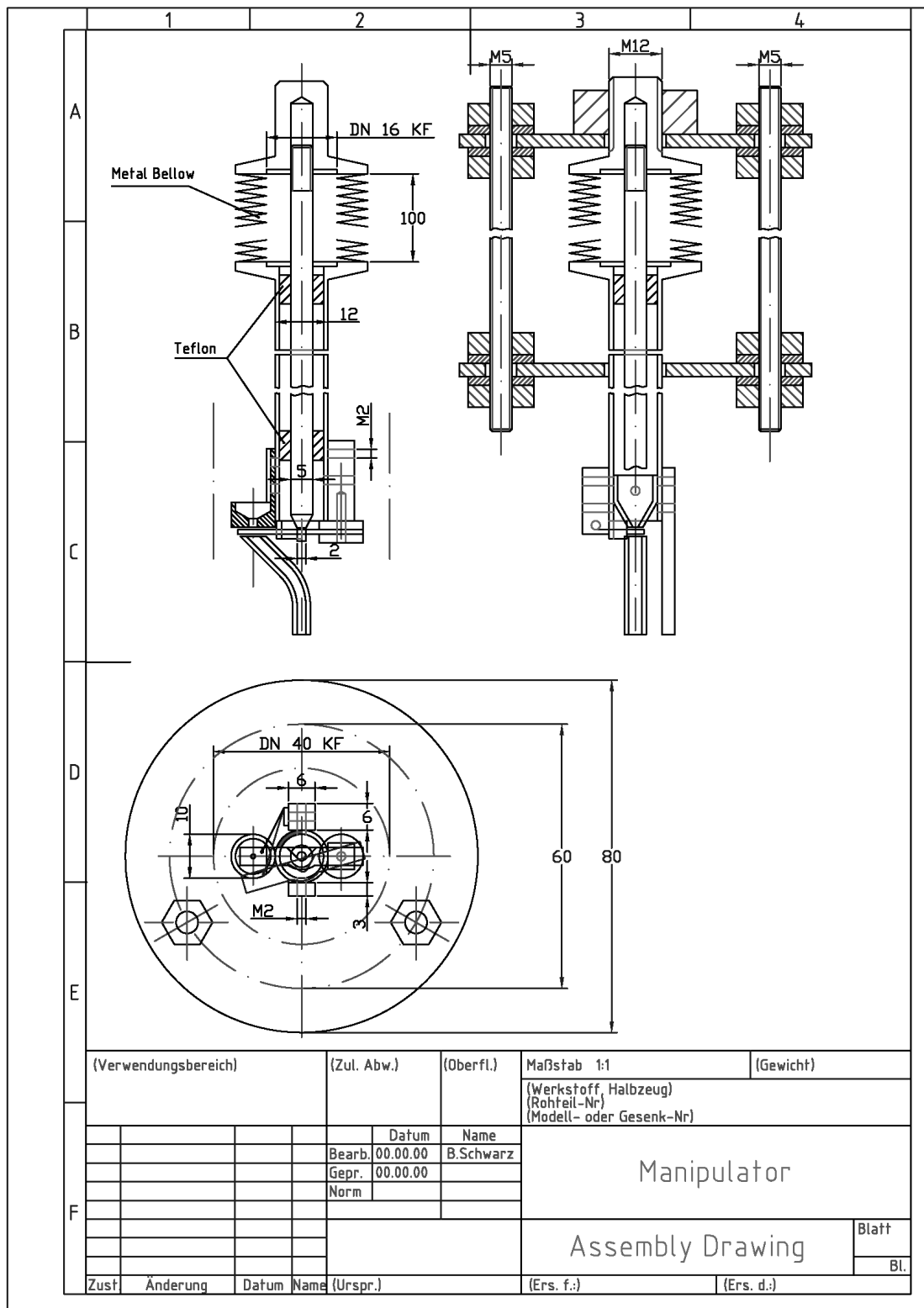
Figure A.3: Technical drawing of the manipulator.
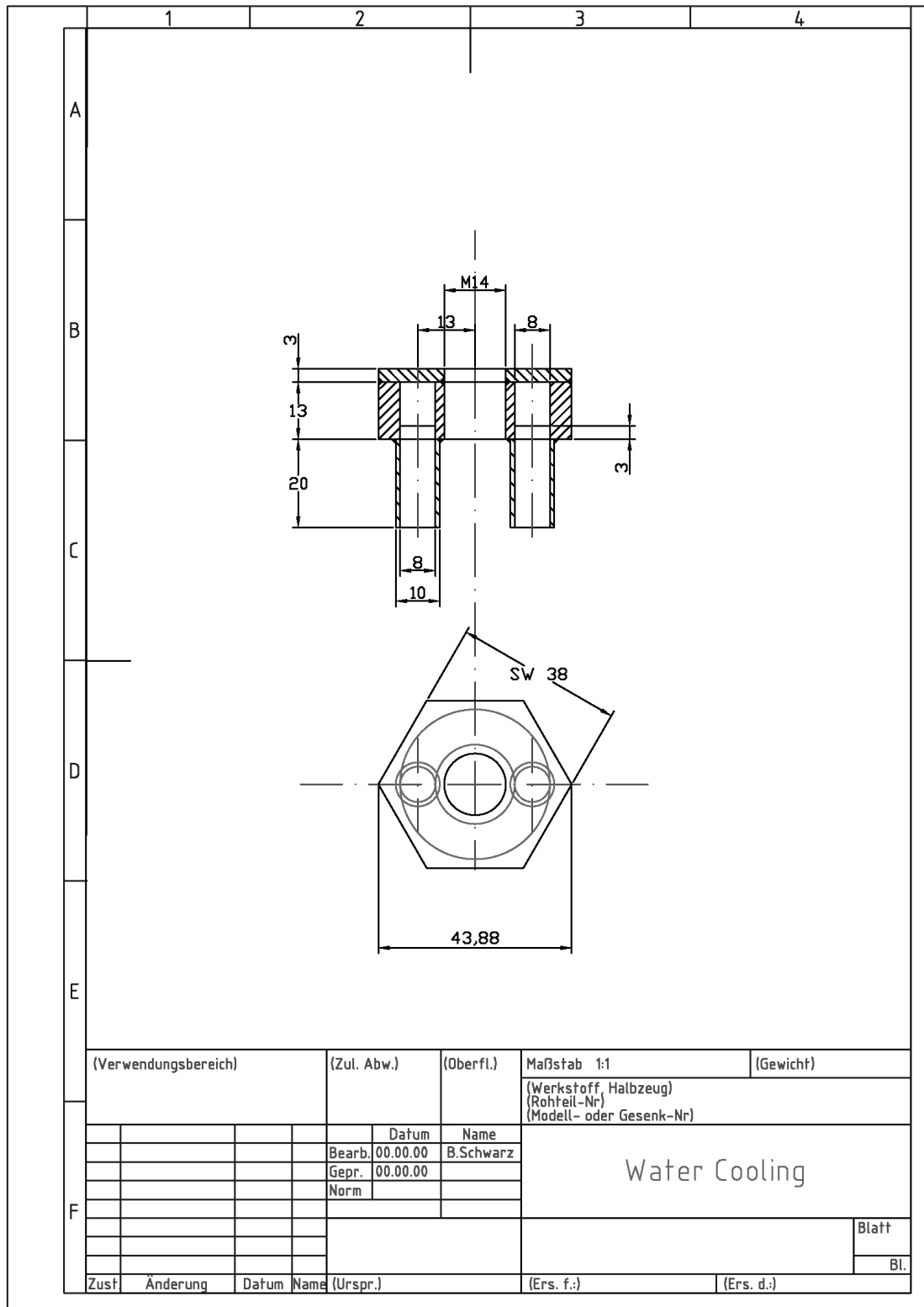
Figure A.4: Technical drawing of the water cooling.

Appendix B

Calibration Table

The calibration of the thermocouple was done by measuring the thermovoltages at different definite temperatures (either hot stage or melting points of metals) in the HTSDD. The equation for the linear fit through the measured thermovoltages is given by:

$$U_{Therm}[mV] = 0,0319\ T[°C] - 0,9683 \qquad \text{(B.1)}$$

The table generated from this equation is given in B.1. There the temperatures are given in the first row and first column of the table, and by the intersection at the desired temperature (in $°C$) the corresponding thermovoltage (in mV) can be read off.

0	0	10	20	30	40	50	60	70	80	90
0	-0,97	-0,65	-0,33	-0,01	0,31	0,63	0,94	1,26	1,58	1,90
100	2,22	2,54	2,86	3,18	3,49	3,81	4,13	4,45	4,77	5,09
200	5,41	5,73	6,05	6,36	6,68	7,00	7,32	7,64	7,96	8,28
300	8,60	8,91	9,23	9,55	9,87	10,19	10,51	10,83	11,15	11,46
400	11,78	12,10	12,42	12,74	13,06	13,38	13,70	14,02	14,33	14,65
500	14,97	15,29	15,61	15,93	16,25	16,57	16,88	17,20	17,52	17,84
600	18,16	18,48	18,80	19,12	19,43	19,75	20,07	20,39	20,71	21,03
700	21,35	21,67	21,99	22,30	22,62	22,94	23,26	23,58	23,90	24,22
800	24,54	24,85	25,17	25,49	25,81	26,13	26,45	26,77	27,09	27,40
900	27,72	28,04	28,36	28,68	29,00	29,32	29,64	29,96	30,27	30,59
1000	30,91	31,23	31,55	31,87	32,19	32,51	32,82	33,14	33,46	33,78
1100	34,10	34,42	34,74	35,06	35,37	35,69	36,01	36,33	36,65	36,97
1200	37,29	37,61	37,93	38,24	38,56	38,88	39,20	39,52	39,84	40,16
1300	40,48	40,79	41,11	41,43	41,75	42,07	42,39	42,71	43,03	43,34

Table B.1: Calibration Table for the Ni-CrNi thermocouple.

Appendix C

Navitar Zoom 6000

Factory specifications:

Magnification: 0,7 × - 4,5 ×

Zoom + adapter: 6,5 × + 1,0 ×

Operating distance: 92 mm

Object to image distance: 345 mm

Resolution: small magnification: 7 μm, big magnification: 2 μm

Depth of focus: small magnification: 1,83 mm, big magnification: 0,20 mm

Specifications used in the HTSDD:

Auxiliary lens + zoom + adapter: 0,5 × + 6,5 × + 1,0 ×

Operating distance: 175 mm (parfocal distance)

Object to image distance: 432 mm

Resolution: small magnification: 14 μm, big magnification: 5 μm

Depth of focus: small magnification: 7,31 mm, big magnification: 0,80 mm

Protection foil

In front of the optic an additional protection foil was mounted to reduce the brightness (glowing metal droplet and background illumination) for the webcam. A commercially available solar eclipse foil was used for this purpose.

Appendix D

Derivation of Young's Equation

This derivation is made under the assumptions of a circular drop an a flat solid surface and the droplet has the shape of a spherical cap. The derivation is done for the two-dimensional case and the mass of the drop is small, therefore gravitation can be neglected [71].

The total energy E_{tot} of the system is given by,

$$E_{tot} = \sigma_{LV} L_{LV} + \sigma_{SV} L_{SV} + \sigma_{SL} L_{SL} \tag{D.1}$$

where σ_{LV}, σ_{SV} and σ_{SL} are the interfacial energies and L_{LV}, L_{SV} and L_{SL} are the lengths of the interfacials lines.
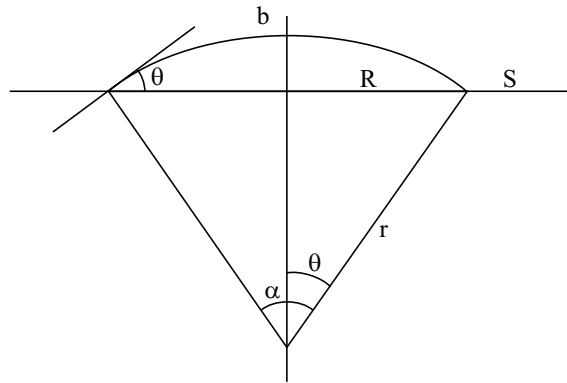
Figure D.1: Spherical cap with the relevant parameters.

In Figure D.1 the spherical cap with all relevant parameters for the derivation of the Young's equation are given.

$$b = r\alpha \tag{D.2}$$

$$r = \frac{R}{\sin\left(\frac{\alpha}{2}\right)} \tag{D.3}$$

The total energy can therefore be written as:

$$E_{tot} = \sigma_{LV}\frac{2R\theta}{\sin\theta} + \sigma_{SV}\left(S - 2R\right) + \sigma_{SL}2R \tag{D.4}$$

with S as the length of the substrate.

Here $R = R\left(\theta\right)$ which can be calculated from the profile area A of the spherical cap. The area of the cap is given by

$$A = \frac{\alpha}{2}r^2 - \frac{1}{2}r^2\sin\alpha \tag{D.5}$$

with $\alpha = 2\theta$ Equation D.5 leads to

$$A = \theta\frac{R^2}{\sin^2\theta} - \frac{1}{2}\frac{R^2}{\sin^2\theta}\sin\left(2\theta\right) \tag{D.6}$$

$$A = \frac{R^2}{\sin^2\theta}\left(\theta - \frac{1}{2}\sin\left(2\theta\right)\right) \tag{D.7}$$

Inserting $\sin\left(2\theta\right) = 2\sin\theta\cos\theta$ into Equation D.7 and solving for R leads to

$$R = \frac{\sin\theta}{\sqrt{A\left(\theta - \sin\theta\cos\theta\right)}} \tag{D.8}$$

Since the liquid is incompressible and the mass should stay constant, also the profile area A stays constant.

The equilibrium condition of the total energy E_{tot} is

$$\frac{\partial E_{tot}\left(R\left(\theta\right),\theta\right)}{\partial\theta} = 0 \tag{D.9}$$

$$\frac{\partial}{\partial\theta}\left[\sigma_{LV}\frac{2R\theta}{\sin\theta} + \sigma_{SV}\left(S - 2R\right) + \sigma_{SL}2R\right] = 0 \tag{D.10}$$

$$\sigma_{LV}\frac{\partial}{\partial\theta}\left[\frac{\theta}{\sqrt{\theta - \sin\theta\cos\theta}}\right] + \left(\sigma_{SL} - \sigma_{SV}\right)\frac{\partial}{\partial\theta}\left[\frac{\sin\theta}{\sqrt{\theta - \sin\theta\cos\theta}}\right] = 0 \tag{D.11}$$

$$\sigma_{LV} \left(\frac{1}{\sqrt{}} + \theta \frac{\partial}{\partial \theta} \left[\frac{1}{\sqrt{}} \right] \right) + (\sigma_{SL} - \sigma_{SV}) \left(\frac{1}{\sqrt{}} \cos \theta + \sin \theta \frac{\partial}{\partial \theta} \left[\frac{1}{\sqrt{}} \right] \right) = 0 \quad \text{(D.12)}$$

with the abbreviation $\sqrt{} = \sqrt{\theta - \sin \theta \cos \theta}$.

$$\frac{\partial}{\partial \theta} \left[\frac{1}{\sqrt{}} \right] = -\frac{1}{\sqrt{}^2} \left(\frac{1}{2} \frac{1 - \cos^2 \theta + \sin^2 \theta}{\sqrt{}} \right) \quad \text{(D.13)}$$

$$\sigma_{LV} \left(\frac{1}{\sqrt{}} - \frac{\theta}{\theta - \sin \theta \cos \theta} \frac{1}{2} \frac{1 - \cos^2 \theta + \sin^2 \theta}{\sqrt{}} \right)$$
$$+ (\sigma_{SL} - \sigma_{SV}) \left(\frac{\cos \theta}{\sqrt{}} - \frac{\sin \theta}{\theta - \sin \theta \cos \theta} \frac{1}{2} \frac{1 - \cos^2 \theta - \sin^2 \theta}{\sqrt{}} \right) = 0 \text{ (D.14)}$$

$$\sigma_{LV} \left(\frac{1}{\sqrt{\theta - \sin \theta \cos \theta}} - \frac{\theta \sin^2 \theta}{(\theta - \sin \theta \cos \theta)^{3/2}} \right)$$
$$+ (\sigma_{SL} - \sigma_{SV}) \left(\frac{\cos \theta}{\sqrt{\theta - \sin \theta \cos \theta}} - \frac{\sin^3 \theta}{(\theta - \sin \theta \cos \theta)^{3/2}} \right) = 0 \quad \text{(D.15)}$$

bringing the fraction to the same denominator and canceling the denominator $(\theta - \sin \theta \cos \theta)^{3/2} \neq 0$ for $\theta \neq 0$, gives

$$\sigma_{LV} \left(\theta - \sin \theta \cos \theta - \theta \sin^2 \theta \right)$$
$$+ (\sigma_{SL} - \sigma_{SV}) \left(\theta \cos \theta - \sin \theta \cos^2 \theta - \sin^3 \theta \right) = 0 \quad \text{(D.16)}$$

Some further transformations lead to

$$\frac{\sigma_{SV} - \sigma_{SL}}{\sigma_{LV}} = \frac{\theta \left(1 - \sin^2 \theta \right) - \sin \theta \cos \theta}{\theta \cos \theta - \sin \theta \left(\cos^2 \theta + \sin^2 \theta \right)} \quad \text{(D.17)}$$

with following trigonometric substitution

$$1 - \sin^2 \theta = \cos^2 \theta \quad \text{(D.18)}$$

the calculation leads to

$$\frac{\sigma_{SV} - \sigma_{SL}}{\sigma_{LV}} = \frac{\theta \cos^2 \theta - \sin \theta \cos \theta}{\theta \cos \theta - \sin \theta} = \frac{\cos \theta \left(\theta \cos \theta - \sin \theta\right)}{\theta \cos \theta - \sin \theta} \tag{D.19}$$

and by canceling this expression, we get

$$\frac{\sigma_{SV} - \sigma_{SL}}{\sigma_{LV}} = \cos \theta \tag{D.20}$$

which is the Young's equation.

Appendix E

Evaporation and Vapor pressure table
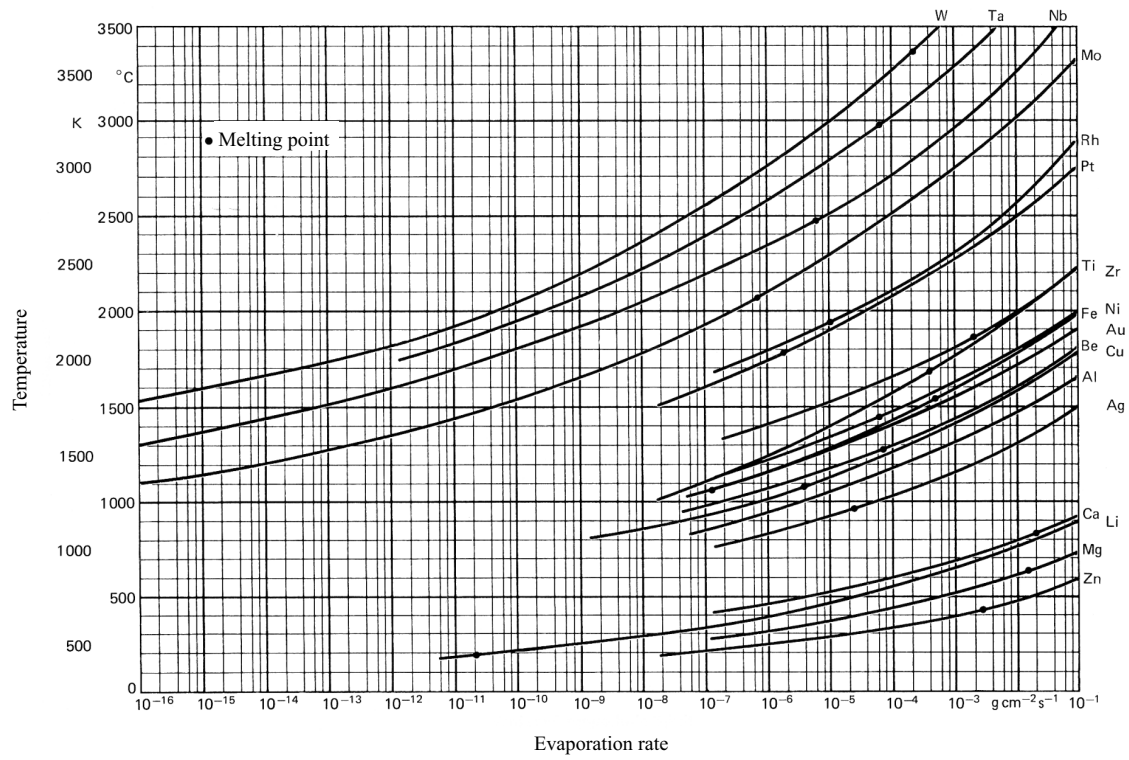
Figure E.1: Evaporation rate in high vacuum depending on the temperature [36].
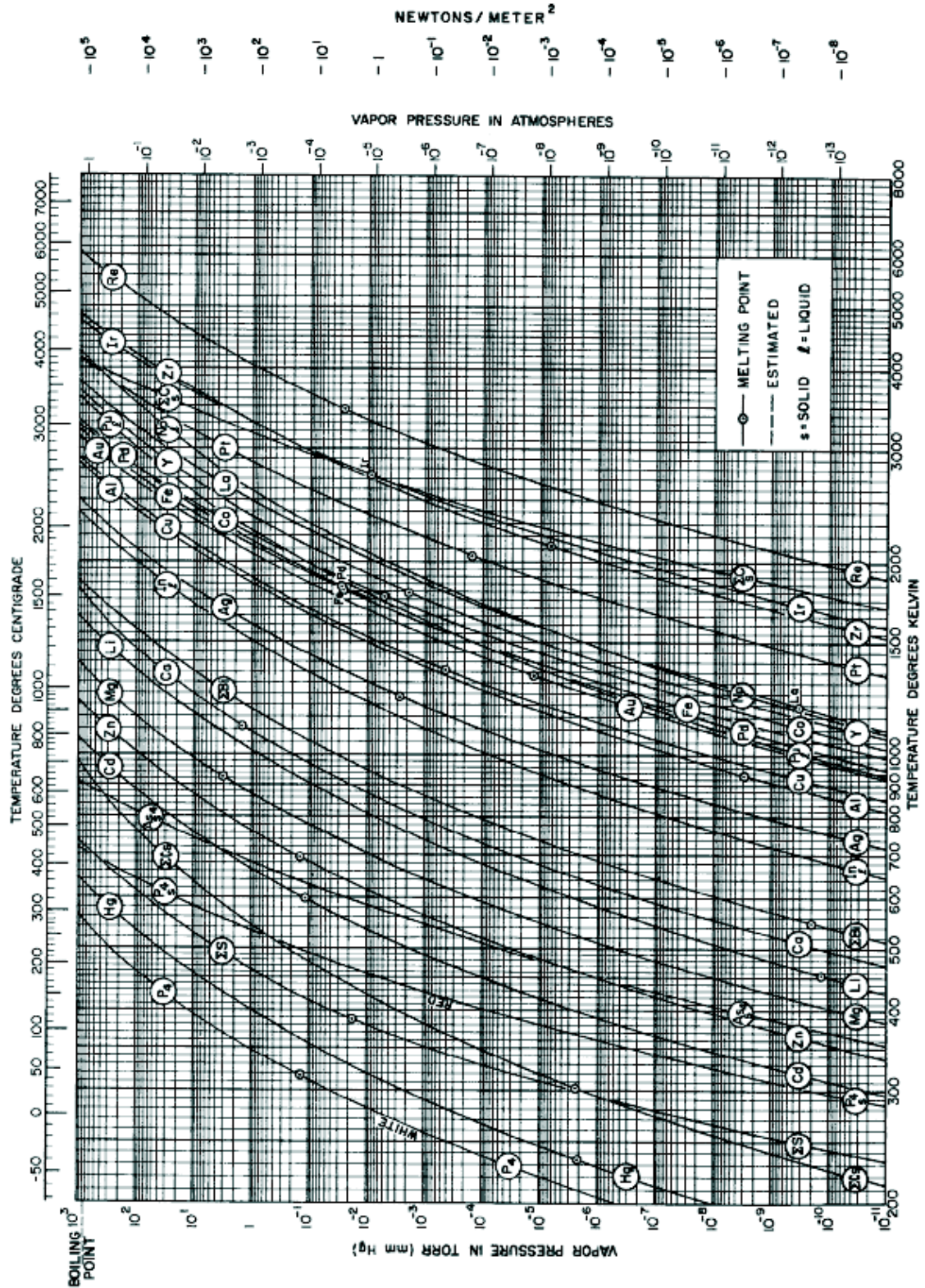
Figure E.2: Vapor pressure of several elements [72].

Appendix F

Material parameters

Property	Unit	Sigradur®G	CuABA
CTE [1]	K^{-1}	2,6 $\times 10^{-6}$	19,5 $\times 10^{-6}$
Density	$g\ cm^{-3}$	1,42	8,1
Young's modulus	GPa	35	96
Thermal conductivity [2]	$W\ m^{-1}\ K^{-1}$	6,3	38
Specific electrical resistance [2]	$\Omega\,\mu m$	45	198
Maximum service temperature	°C	3000	-
Open porosity	%	0	-
Liquidus temperature	°C	-	1024
Brazing Range	°C	-	1025 - 1050

[1] Coefficient of Thermal Expansion 20 - 200 °C

[2] 30 °C

Table F.1: Material parameters for Sigradur® G and CuABA [57, 73].

Chemical composition of the CuABA brazing alloy (in wt%, [73]):
92,77% Cu, 3% Si, 2%Al, 2,25% Ti

Material parameters of CFC NB31:

Property	Unit	T [°C]	x - direction	y - direction	z - direction
Density	g cm^{-3}	RT	1,9		
Porosity	%	RT	< 8%		
CTE	10^{-6} K^{-1}	1000	0,5		
		1500	0,7		
Therm. Cond.	W m^{-1} K^{-1}	RT	323	117	115
		500	180		
		800	154	58	55
		1000	145	56	52
		1500	136	55	51
Specific Heat	J kg^{-1} K^{-1}	500	1570	1570	1570
		3367	2166	2166	2166
Tensile strength	MPa	RT	130	30	19
		1000	165	42	27
		1500	185	50	30
Young's modulus	GPa	RT	107	15	12
		1000	107	20	12
		1500	107	22	12

Table F.2: Material parameters of CFC NB31 from Snecma Propulsion Solide (France) [74].

Material parameters of graphite IG-43 from Toyo Tanso:

Property	Value	Unit
Bulk density	1,82	g/cm^3
Electrical resistivity	9,2	$\mu\Omega m$
Flexural strength	54	MPa
Compressive strength	90	MPa
Tensile strength	37	MPa
Elastic modulus	10,8	GPa
CTE $_{(350-450°C)}$	4,8	10^{-6} K^{-1}
Therm. conductivity	14	W/m K
Average grain size	10	μm
Porosity	14	%

Table F.3: Material parameters of graphite IG-43 from Toyo Tanso [75].

Appendix G

Coefficient of determination

The coefficient of determination is the square of the Pearson's correlation coefficient R, which is defined as follows,

$$R = \frac{\sum_{i=1}^{n} (x_i - \bar{x})(y_i - \bar{y})}{\sqrt{\sum_{i=1}^{n} (x_i - \bar{x})^2} \cdot \sqrt{\sum_{i=1}^{n} (y_i - \bar{y})^2}} \qquad (G.1)$$

with the mean value $\bar{x}$:

$$\bar{x} = \frac{1}{n} \sum_{i=1}^{n} x_i \qquad (G.2)$$

The value of R^2 is in the range between 0 and 1, where 0 means none and 1 means a complete correlation.

List of Publications

Article:

I. E. Klein, <u>B. Schwarz</u>, C. Eisenmenger-Sittner, C. Tomastik, P.B. Barna, A. Kovács. Vacuum 80 (2005) 74-80.

II. C. Schrank, <u>B. Schwarz</u>, C. Eisenmenger-Sittner, K. Mayerhofer, E. Neubauer. Vacuum 80 (2005) 122-127.

III. <u>B. Schwarz</u>, C. Schrank, C. Eisenmenger-Sittner, M. Stöger-Pollach, M. Rosner, E. Neubauer. Surface and Coatings Technology 200 (2006) 4891-4896.

IV. <u>B. Schwarz</u>, C. Eisenmenger-Sittner, E. Klein, C. Tomastik, K. Mayerhofer, P.B. Barna, A. Kovács. Surface and Coatings Technology 200 (2006) 6484-6489.

V. C. Eisenmenger-Sittner, <u>B. Schwarz</u>, C. Tomastik, P.B. Barna, A. Kovacs. Applied Surface Science 252 (2006) 5466-5469.

VI. <u>B. Schwarz</u>, C. Eisenmenger-Sittner, H. Steiner. Vacuum 82 (2008) 186-188.

VII. <u>B. Schwarz</u>, P. Worbs, C. Eisenmenger-Sittner, in print, Journal of Physics: Conference Series, Stockholm.

VIII. C. Eisenmenger-Sittner, H. Steiner, <u>B. Schwarz</u>, in print, Journal of Physics: Conference Series, Stockholm.

IX. M. Kiniger, C. Eisenmenger-Sittner, J. Hell, <u>B. Schwarz</u>, H. Hutter, S. Puchner, submitted to Surface and Interface Analysis, Brussels, Belgium.

X. W. Vollnhofer, C. Eisenmenger-Sittner, J. Hell, M. Kiniger, <u>B. Schwarz</u>, H. Steiner, C. Tomastik, submitted to Surface and Interface Analysis, Brussels, Belgium.

Poster:

I. <u>B. Schwarz</u>, C. Schrank, C. Eisenmenger-Sittner, H. Bangert. "Thermisch induzierte Entnetzung von Kupferschichten auf Kohlenstoff", 12. Tagung Festkörperanalytik - TU Wien, Austria, 22. - 24. September 2003.

II. <u>B. Schwarz</u>, C. Schrank, C. Eisenmenger-Sittner, M. Stöger-Pollach, M. Rosner, E. Neubauer. "Adhesion promotion of copper-coatings to carbon surfaces by plasma pre-treatment and molybdenum interlayers", 16th International Vacuum Congress, June 28 - July 2, 2004, Venice, Italy.

III. C. Schrank, <u>B. Schwarz</u>, C. Eisenmenger-Sittner, E. Neubauer. "Recrystallisation induced de-wetting of copper coatings from carbon surfaces studies by AFM und TEM", 16th International Vacuum Congress, June 28 - July 2, 2004, Venice, Italy.

IV. E. Klein, <u>B. Schwarz</u>, C. Eisenmenger-Sittner, C. Tomastik, A. Kovacs. "Passivation of aluminum (Al) surfaces against oxidation by a monoatomic tin (Sn) wetting layer", 16th International Vacuum Congress, June 28 - July 2, 2004, Venice, Italy.

V. <u>B. Schwarz</u>, C. Schrank, C. Eisenmenger-Sittner. M. Stöger-Pollach, M. Rosner, E. Neubauer. "Molybdenum interlayers as adhesion promoters for thin copper films on plasma treated glassy carbon", 10th Joint Vacuum Congress, September 28 - October 2, 2004, Portoroz, Slovenia.

VI. E. Klein, <u>B. Schwarz</u>, C. Eisenmenger-Sittner, C. Tomastik. "The initial stages of wetting and spreading of Sn on Al surfaces", 10th Joint Vacuum Congress, September 28 - October 2, 2004, Portoroz, Slovenia.

VII. C. Schrank, <u>B. Schwarz</u>, C. Eisenmenger-Sittner, E. Neubauer, K. Mayerhofer. "Influence of thermal treatment on the adhesion of copper coatings on carbon substrates", 10th Joint Vacuum Congress, September 28 - October 2, 2004, Portoroz, Slovenia.

VIII. <u>B. Schwarz</u>, C. Eisenmenger-Sittner, E. Klein, C. Tomastik, K. Mayerhofer, P. B. Barna, A. Kovac. "Passivation of Al surfaces against oxidation by monoatomic Sn wetting layers", E-MRS Spring Meeting, May 31 - June 3, 2005, Strasbourg, France.

IX. C. Eisenmenger-Sittner, <u>B. Schwarz</u>, C. Tomastik, P. B. Barna, A. Kovacs. "Experimental Studies of Solid State Surface Wetting of Sn on Al", 13th International Congress on Thin Films, June 19 - 23, 2005, Stockholm, Schweden.

X. K. E. Mayerhofer, <u>B. Schwarz</u>, C. Eisenmenger-Sittner, H. Hutter. "Influence of Sn wetting layers on the oxidation behavior of Al sputter deposits", 13. Tagung Festkörperanalytik, July 26 - 29, 2005, Chemnitz, Germany.

XI. C. Eisenmenger-Sittner, <u>B. Schwarz</u>, J. Hell, E. Neubauer. "Application of Vacuum Based Processes for the Production of Metall Matrix Composites", IUVSTA ECM-100, September 18 - 20, 2006, Seoul, Korea.

XII. <u>B. Schwarz</u>, C. Eisenmenger-Sittner, H. Steiner. "Construction of a High Temperature Sessile Drop Device", 11th Joint Vacuum Conference, September 24 - 28, 2006, Prague, Czech Republic.

XIII. <u>B. Schwarz</u>, P. Worbs, C. Eisenmenger-Sittner. "Applications of a High Temperature Sessile Drop Device", 17th International Vacuum Conference, July 2 - 6, 2007, Stockholm, Schweden.

XIV. H. Steiner, C. Eisenmenger-Sittner, <u>B. Schwarz</u>. "Temperature induced recrystallization of copper coatings deposited on adhesion promoting molybdenum interlayers", 17th International Vacuum Congress, July 2 - 6, 2007, Stockholm, Sweden.

XV. M. Kiniger, C. Eisenmenger-Sittner, J. Hell, <u>B. Schwarz</u>, H. Hutter, S. Puchner. "Carbide Formation in Mo Layers Deposited on Carbon Substrates: Comparison of Experimental Data with a Cellular Automaton (CA) Model" 12th European Conference on Applications of Surface and Interface Analysis, September 9 - 14, 2007, Brussels, Belgium.

XVI. W. Vollnhofer, C. Eisenmenger-Sittner, J. Hell, M. Kiniger, <u>B. Schwarz</u>, H. Steiner, C. Tomastik. "The Influence of Temperature Treatment and Carbon Addition on the Surface Morphology and the Surface Energy of Molybdenum Layers on Carbon Substrates", 12th European Conference on Applications of Surface and Interface Analysis, September 9 - 14, 2007, Brussels, Belgium.

XVII. P. Worbs, <u>B. Schwarz</u>, H. Maier, H. Bolt. "TiC Coatings as Wetting Promoter for optimizing C/Cu brazed Joints in High Heat Flux Components", European Congress and Exhibition on Advanced Materials and Processes, Euromat2007, September 10 - 13, 2007, Nürnberg, Germany.

Acknowledgement

I would like to thank my supervisor Prof. Christoph Eisenmenger-Sittner for the opportunity to do my thesis on this very interesting physical topic. His support and help during the work was outstanding. I would also like to thank him for the possibility to visit many conferences during my thesis.

I want to thank the whole "Thin Film" group for their help and their support during my work, especially my thank is devoted to Johannes Hell, Harald Steiner, Marianne Kiniger and Wolfgang Vollnhofer. Also thanks to our trainee, Thomas Kölbl, for his manufacturing assistance. To all other colleagues during my work at the University, thank you.

The workshop of our institute I would like to thank for the help with the planning, constructing and manufacturing of my device: Andreas Lahner, Josef Sicherl, Jürgen Gindl and Roland Oppelmayer.

A great thank to Prof. Degischer who managed the EU project and to his secretary Tanja Grünwald for the easy handling of my invoices and travel costs.

I would also like to thank Dr. Hans Maier and Peter Worbs, project partner from IPP Garching, Munich, for their RBS measurements of my samples and their fruitful discussions followed during the thesis. A great thank to Dr. Carlo Gualco, project partner from ARI Ansaldo Ricerche S.p.A., Geneva, for the support of substrates and the brazing experiments.

At last I would like to thank my family: my parents for supporting me in every decision I made in my life, my brother Robert for his great computer skills and finally my wife, Sabine, for standing by my side.

Curriculum Vitae

09. 07. 1976	Born in Krems/Donau
1982 - 1986	Elementary School/Wieselburg
1986 - 1990	Grammar School/Wieselburg
1990 - 1995	HLBLA Francisco-Josephinum, Polytechnic for agricultural engineering
Juni 1995	Final examination passed with distinction
Oct. 1995 - Juni 1996	Military Service in Horn as wireless operator
Oct. 1996	Begin of the study "Technical Physics" at the Vienna University of Technology
Nov. 2002 - Oct. 2003	Master Thesis at the TU Vienna, Institute for Solid State Physics E138. "Untersuchung der Haftfestigkeit von Kupfer auf oberflächenbehandeltem glasartigen Kohlenstoff mittels Transmissionselektronenmikroskopie."
8. Oct. 2003	Final examination passed with distinction
Since 1. 1. 2004	PhD student at the Vienna University of Technology, Institute of Solid State Physics E138, Thin Film Group
	FWF Project P14534: "Wechselwirkung zwischen Cu und vorbehandelten C-Oberflächen" FWF Project P15739: "Phasenbildung und Entmischung in polykristallinen Schichten" EU Project NMP3-CT-2004-500253: "ExtreMat - New Materials for Extreme Environments"